TISSUE AND WHOLE ORGAN DECELLULARIZATION: AN EVALUATION OF CYTOCOMPATIBILITY AND MECHANICS

by

Christopher Arthur Carruthers

B.S. in Biomedical Engineering, University of Rochester, 2007

Submitted to the Graduate Faculty of

The Swanson School of Engineering in partial fulfillment

of the requirements for the degree of

Doctor of Philosophy

University of Pittsburgh

2013

UNIVERSITY OF PITTSBURGH

SWANSON SCHOOL OF ENGINEERING

This dissertation was presented

by

Christopher Arthur Carruthers

It was defended on

August 7, 2013

and approved by

Thomas W. Gilbert, PhD, VP of Research and Development, ACell, Inc.

Charles F. McTiernan, PhD, Associate Professor, Department of Medicine, University of Pittsburgh

Michael S. Sacks, PhD, Professor, Department of Biomedical Engineering, University of Texas at Austin

Sanjeev G. Shroff, PhD, Professor, Department of Bioengineering, University of Pittsburgh

Dissertation Director: Stephen F. Badylak, DVM, PhD, MD, Professor, Department of Surgery, University of Pittsburgh

TISSUE AND WHOLE ORGAN DECELLULARIZATION:
AN EVALUATION OF CYTOCOMPATIBILITY AND MECHANICS

Christopher Arthur Carruthers, PhD

University of Pittsburgh, 2013

Extracellular matrix (ECM) scaffolds offer an alternative treatment to repair damaged cardiac tissue by promoting the formation of functional host tissue. While promising, the methods used to manufacture ECM scaffold materials vary widely with different source tissues, detergents, methods of application, and duration. This variability results in differences in the final ECM composition and structure that can lead to inconsistent clinical outcomes. Minimal information exists regarding the physical and biological effects of different detergent treatments used for decellularization upon the resultant ECM scaffold.

Cardiac tissue includes both the ECM structure and composition, each of which has reciprocal effects upon cell phenotype and gene expression. This cell-ECM interaction was evaluated by cell deformation and biosynthetic activity and was found to be dependent on localized mechanical coupling to the fiber network. Differences were noted by anatomic location and tissue layer. A therapeutic strategy to replace damaged cardiac tissue with site-specific cardiac derived ECM scaffolds may thus be advantageous. However, different detergent treatments used to decellularize may negatively impact this microstructural complexity and the associated downstream beneficial effects upon tissue remodeling.

Two clinically relevant source tissues, urinary bladder and heart, were treated with four detergents commonly used for tissue decellularization: a non-ionic detergent (Triton™ X-100), a zwitterionic detergent (CHAPS), and two ionic detergents (sodium deoxycholate and SDS). For bladder tissue, detergents were applied through immersion and mechanical agitation, and for

myocardium, detergents were applied through whole organ retrograde perfusion. The composition, structure, mechanics, and in-vitro cytocompatibility of the resultant ECM materials were characterized.

Results show that Triton™ X-100 adequately decellularized bladder tissue but not myocardium during whole organ perfusion. Sodium deoxycholate and SDS were found to be highly effective for decellularization. CHAPS and SDS resulted in a loss of ECM constituents such as GAGs and denatured the collagen fiber network. Failure strength was unaffected by detergent choice. These findings for CHAPS and SDS correlated with a poor in-vitro cytocompatibility. Triton™ X-100 and sodium deoxycholate retained composition, structure, and in-vitro cytocompatibility. This information may assist in the development of rational strategies for effective decellularization of tissues while maintaining ECM structure-function properties.

TABLE OF CONTENTS

LIST OF TABLES

LIST OF FIGURES

PREFACE

The pursuit of a doctorate involves a process of one's growth and development as a researcher. This maturation can go forward only with the help and dedication of others. I am thankful to many people whose continuous support and feedback were essential to my success. First and foremost I am indebted to Dr. Stephen Badylak for accepting me into his laboratory and facilitating the completion of my doctoral studies. I will forever value his support and the opportunity to participate in such an interdisciplinary clinically driven environment. I also appreciate Dr. Michael Sacks for fostering my ability as an engineer. When I first entered graduate school I was a novice, but now, I have become a critical researcher.

My Doctoral Committee's ideas and criticisms helped me to improve as a scientist. Thank you to Dr. Sanjeev Shroff, Dr. Thomas Gilbert, Dr. Charles McTiernan, and once again, to Dr. Stephen Badylak and Dr. Michael Sacks for their dedication to my development and for the valuable insights that they provided to this body of work.

The Department of Bioengineering has given unrelenting support. I especially thank Dr. Harvey Borovetz and Dr. Sanjeev Shroff for their dedication to the institution and their continuing support of my endeavors. I also always appreciate Dr. Steven Abramowitch for keeping his door open to provide sage insights or just to invite me to grab a bite to eat. The administrative staffs were invaluable friends and colleagues who keep the gears turning: Jocelyn Runyon, Eve Simpson, Allyson LaCovey, Nicholas Mance, Glenn Peterson, Karen Connor, Joan Williamson and Lynette Spataro.

I would not have had a chance ever to develop the skills necessary to pursue my doctorate without first having the opportunity to participate in undergraduate research. Dr. Savio L-Y. Woo fostered my passion for the field of biomechanics and regenerative medicine in his renowned Musculoskeletal Research Center. I am honored to state that Dr. Woo continues to be a friend and mentor. LaShon Jackson and Joan Williamson of the Pittsburgh Tissue Engineering Initiative provided funding for this research opportunity and later welcomed me back to share my experiences as a researcher with high school and college students. Dr. Noah Cowan of Johns Hopkins University, Dr. Diane Dalecki and Dr. Denise Hocking of the University of Rochester, and Dr. Michael King of Cornell University each provided me with meaningful instrumental research opportunities in their laboratories.

I am also thankful to my fellow colleagues for assisting me in developing the skill sets necessary for the performance of experiments that were key to this endeavor. I look forward to their continued friendship and to additional intellectual discussions. Dr. Christopher Dearth provided both excellent mentorship and insight on this work. Christopher Hobson, Dr. Antonio D'Amore, Dr. John Stella, Dr. Andrew Feola, Dr. Chad Eckert, Dr. Rouzbeh Amini, Noah Papas, Christopher Medberry, Brian Sicari, Matt Wolf, and Denver Faulk were incredibly dedicated to my development as a researcher. Ricardo Londono, Tim Keane, Lisa Carey, Dr. Peter Slivka, Dr. Fanwei Meng, Dr. Rebecca Heise, Dr. Erinn Joyce, Dr. Bahar Fata, Diana Gaitan, Dr. Silvia Enders-Wognum, and Serena Augustine were always willing to lend a helping hand. Bryan Good and Caroline Kramer were excellent undergraduate researchers who contributed to the completion of this work.

I am especially thankful for the patience and mentoring of the staff scientists and laboratory managers: Janet Reing, Scott Johnson, Dr. Li Zhang, Dr. Rui Liang, Deanna Rhoads,

Jennifer DeBarr, Dr. Hongbin Jiang, John Freund, and Dr. Neil Turner. The assistance of Dr. Simon Watkins, Greg Gibson, Jonathan Franks, and Jason Devlin from the Center for Biologic Imaging at the University of Pittsburgh was critical to successful acquisition and analysis of data from both two photon microscopy and scanning electron microscopy. The support of my colleagues at the UPMC artificial heart program strengthened my clinical perspective of cardiovascular disease and treatment: Stephen Winowich, Dr. Richard Schaub, Douglas Lohmann, Donald Severyn, Erin Driggers, Robert Stone, and Michael McCall.

The National Institute of Health (T32 Trainee in Biomechanics in Regenerative Medicine Program), the National Science Foundation (Graduate Research Fellowship Program), the McGowan Institute of Regenerative Medicine, and the Wesley C. Pickard Fellowship provided the funding necessary for the completion of this work. For this assistance I shall always be thankful.

Without family and friends such work would be without purpose. To my mother and father: Thank you for believing in me and instilling in me a sense of purpose. You supported my development without boundaries, and were always there for me. I would also like to thank Raphael Schwartz, Mathew Scullin, Kevin Scullin, and Steven Cullen for always providing a good laugh and perspective.

Finally, to my wife, Elizabeth: I am forever grateful for your love, support no matter the hour, dedication, and sacrifice. You encouraged me always to remain positive, to laugh, and to enjoy life. Your support has been essential to my success. I dedicate this body of work to you.

1.0 INTRODUCTION

1.1 HEART FAILURE AND TREATMENT STANDARD

The function of the heart is to pump blood through a network of arteries and veins called the cardiovascular system for nutrient transport, oxygen transport, and metabolic waste removal. Cardiovascular disease is a broad term to describe the malfunction of both the heart and cardiovascular system. This term encompasses the narrowing of blood vessels, coronary artery disease, heart rhythm problems, heart infections, and congenital heart defects. Cardiovascular disease accounts for more than one in three deaths in the United States and had an estimated cost of $300 billion in 2009 alone (1). The first line of treatment requires lifestyle changes such as diet and exercise coupled with medication to lower blood pressure, prevent coagulation, and lower cholesterol. The next line of treatment after severe angina is either coronary angioplasty or bypass, a surgical procedure to open a narrow blocked coronary or reroute blood supply around the damaged site using a healthy artery from the lower leg. If heart failure is reached whereby the heart is unable to pump enough blood to meet the body's demands, then treatment options are limited.

Over 3 million Americans over the age of twenty have heart failure with an estimated cost of $32 billion for 2013 (1), and of these patients 200,000 have severe class IV heart failure (2). Treatment options are limited to either pharmacologic therapy such as the use of diuretics to

treat volume overload for symptom relief, mechanical circulatory support, or heart transplant (3). While heart transplant represents the gold standard of treatment, in 2011 less than 2,500 heart transplants were performed in the United States due to donor shortage. To be eligible for a heart transplant, the patient needs to be younger than 65 years of age without significant comorbidity (1, 2). For those patients unable to receive a heart transplant, a ventricular assist device (VAD), a form of mechanical circulatory support, is the only other option. Compared to pharmacologic therapy alone, a VAD is superior offering a reduction in mortality rate of 27% at one year (4).

While VADs are a promising technology, they are not without limitations. VADs require anticoagulation therapy to prevent thromboembolism due to the artificial surface of the VAD. With an increased risk of thromboembolism there is an associated increased risk of stroke and transient ischemic attacks. The necessity for anticoagulation therapy along with a lack of pulsatile flow also presents a risk of bleeding especially in the gastrointestinal space if not well managed (5, 6). VAD-related infections are a prevalent complication and contribute to significant financial burden due to increased need for hospitalization and surgical intervention. VAD related infections are common along the driveline whereby a percutaneous lead connects the internal LVAD motor to an external power supply, although there may also be pump pocket infections, and LVAD associated endocarditis. Patients with VADs have limited mobility due to an accompanied device controller that requires battery power.

While this promising technology is improving with time there is a definitive limitation in that a mechanical circulatory support system does not grow or remodel with the patient, which is especially critical for pediatric patients who will require increasing cardiac output with age. The recent advances in cardiovascular tissue engineering offer a potential platform whereby novel medical devices may grow and remodel with the patient. Such advances are critical to improve the 5-year survival rate of heart failure patients which is only 50% (1).

1.2 CARDIOVASCULAR TISSUE ENGINEERING

Tissue engineering is defined as an "interdisciplinary field that applies the principles of engineering and life science towards the development of biological substitutes that restore, maintain, or improve function" (7). At least 70 companies have developed or are developing tissue engineered products (8). Tissue engineering can further be subdivided into three categories: Cell-based products, cell-free supports, and whole tissues that combine technologies from both cell-based products and cell-free supports (8). Cell-free supports are commonly referred to as biomaterials and may be classified as either synthetic or biologic.

1.2.1 Synthetic Scaffolds

Synthetic technologies utilize either non-absorbable polymers such as polypropylene or biodegradable polymers such as poly(ether ester urethane)urea (PEUU) elastomers (9). The objective of manufacturing biomaterials with synthetic technologies is to replicate the structure of the native tissue or organ with the assembly of biomimetic fibers. Methods of manufacturing

include such techniques as nano-patterned surfaces, microfabrication, electrospinning, and assembled hydrogels (8). These methods of manufacturing create reproducible sheet-structures with controllable mechanical properties. A challenge with these techniques is the limited ability to create three-dimensional porous scaffolds with nano-topographies. Further, while non-absorbable polypropylene synthetic meshes quickly incorporate into the adjacent tissue, they elicit a chronic pro-inflammatory response characterized by the formation of dense fibrotic tissue within and around the mesh (10). Meshes with absorbable filaments are reported to have an augmented inflammatory reaction initially (11) with a subsequent decrease in the inflammatory reaction (12, 13). This formation of fibrotic tissue leads to a mechanical mismatch between the mesh and surrounding host tissue that is associated with pain and discomfort for the recipient (14, 15).

1.2.2 Biologic Scaffolds

Tissue engineering devices that are derived from biologic platforms instead of synthetic platforms provide both structural support and functional cues. Biologic scaffolds composed of mammalian extracellular matrix (ECM) have been successfully used in both pre-clinical and clinical applications for surgical reconstruction of musculotendinous, dermal, cardiovascular, gastrointestinal, and lower urinary tract tissue (16-28). The ECM represents the secreted products of resident cells and includes structural proteins such as collagen and elastin, adhesion proteins such as fibronectin and laminin, proteoglycans, growth factors, and cytokines (29, 30).

Allotransplantation of an organ from one human to another requires immunosuppression therapy. Xenotransplantation is not possible in part due to porcine cell expression of the α-gal epitope and other cell associated epitopes (31). Conversely, ECM is actually highly conserved

amongst many species (32-34) mitigating adverse components of the host immune response (35). These biologic cues in ECM have been shown to influence cell migration, proliferation, and differentiation (36-42). ECM scaffolds promote a constructive remodeling response by modulation of the immune response (43, 44), mechanotransduction at the site of injury (45, 46), rapid degradation and release of bioactive peptides (47-49), and site directed recruitment of progenitor cells (43, 44, 50, 51). A constructive remodeling response modulates the three phases of wound healing (inflammation, proliferation, and maturation) to form site appropriate new tissue as opposed to scarring. While scarring is characterized by the deposition of a dense collagenous ECM that lacks blood supply and nerves independent of anatomic location, a constructive remodeling response results in healthy viable tissue that more closely matches the surrounding area (Table 1).

Table 1: Comparison of a constructive remodeling response to scarring.

	Vascularized	Innervated	Tissue Composition	Structure	Mechanics
Constructive Remodeling	Yes	Yes	Site specific (connective, muscle, epithelial)	Organized fiber network	Similar to surrounding tissue
Scarring	No	No	Dense collagenous matrix	Randomly oriented collagen	Stiffer than surrounding tissue

1.2.3 Site-Specific ECM Scaffolds and Organs

ECM scaffolds are derived from multiple anatomic sites including intestine (52, 53), urinary bladder (17), skin (54), heart valves (55, 56), brain, spinal cord (57), liver (58), and heart (59, 60). Because the ECM is the product of the resident cell populations, it is logical that the specific composition will vary depending on the source tissue, and that the ECM product will be ideally suited for application to the tissue from which it is harvested (61). For example, ECM harvested from the liver compared to collagen gel cultures promoted significant improvement in albumin

synthesis and urea production for seeded hepatocytes (62), and a coculture of sinusoidal endothelial cells and hepatocytes maintained the greatest degree of differentiation on liver ECM compared to either UBM or SIS (63).

Anatomically homologous ECM scaffolds have demonstrated functional improvement in preclinical and clinical applications for the liver (62-64), heart (65, 66), lungs (67), trachea (68), nerve (69), adipose (70), and mammary gland [51]. Recent studies have further demonstrated the successful creation of three-dimensional ECM scaffolds prepared by whole organ decellularization with organs such as the heart (65, 71, 72), liver (64), lungs (67, 73), and kidney (74). Logically, these ECM scaffolds possess the ideal three-dimensional architecture for all components of the organ including vascular, lymphatic, and nerve structures.

Thus, tissue engineered devices that are derived from biologic platforms compared to synthetic platforms offer the potential to successfully incorporate into the surrounding tissue for site specific function. While synthetic platforms offer reproducibility and control over the structure and mechanics, biologic platforms offer the ability to retain a complex heterogeneous three-dimensional structure with constituents that promote a site specific constructive remodeling response.

1.3 ECM SCAFFOLDS FOR CARDIAC REPAIR

1.3.1 Myocardial Infarction and Negative Ventricular Remodeling

While heart transplants and ventricular assist devices are promising technologies for patients with end stage heart failures, they clearly have limitations. After a myocardial infarction new

therapy is necessary to prevent progressive negative ventricular remodeling that may lead to end stage heart failure. Progressive negative ventricular remodeling commences after a myocardial infarction in a multiple step process (75-78): (1) Degradation of associated ECM and an acute inflammatory response, (2) formation of dense collagenous scar due to limited regenerative capacity of myocardium, (3) hypertrophy of myocardium to compensate decrease pumping capability of infarct area, and (4) ventricle dilation with continued infarct wall thinning to maintain cardiac output by increasing stroke volume. After a myocardial infarction, the magnitude of this ventricular dilation is a predictor of poor long term outcome (79). Pharmacologic therapies such as angiotensin converting enzyme inhibitors and β-blockers are used to reduce ventricular remodeling and have proven beneficial in treatment of heart failure (80).

1.3.2 ECM Scaffold Patches for Cardiac Repair

Cardiovascular tissue engineering approaches attempt to attenuate this post-infarction ventricular dilation by surgical restoration with a ventricular patch or restraint device. The majority of cardiac patches and restraint devices have been designed from non-biodegradable synthetic materials such as Dacron, polyester, and nitinol with low elasticity. These devices are characterized by a chronic foreign-body response and no constructive remodeling nor contractile restoration (81-84). Highly elastic and biodegradable polymers such as poly(ester urethane)urea elastomers (PEUUs) have recently demonstrated promise in animal models with the promotion of cardiomyocytes and improved LV function (85, 86). While promising, these biodegradable polymers do not contain bioactive molecules to promote constructive remodeling.

Compared to synthetic polymers, ECM scaffolds promote both structural support and functional cues for cardiac repair. An anatomically site specific cardiac ECM scaffold (71) was recently used in a rodent model of a full thickness right ventricle outflow tract repair (RVOT) compared to an inert Dacron patch up to 4 months (87). The Dacron patch was encapsulated with a fibrous capsule with minimal cellular infiltration, while the c-ECM patch remodeled into a dense connective tissue with scattered islands of striated cardiomyocytes with superior echocardiography results.

While this anatomically site specific cardiac ECM scaffold is promising, non-site specific ECM scaffolds have also demonstrated efficacy. Specifically, a 4-layer multi-laminate urinary bladder matrix (UBM) ECM was compared to expanded polytetrafluoroethlyne (ePTFE) in a full thickness LV wall patch replacement in a porcine animal model up to 3 months (88). At 3 months, histology and immunohistochemistry indicated that UBM was bioresorbed with a vascularized tissue with numerous α-SMA positive myofibroblasts present and isolated regions of striated cardiomyocytes, while ePTFE had a fibrotic-body response with necrosis and calcification. Flow cytometry indicated that UBM had a similar composition of cells to normal myocardium as opposed to ePTFE which had limited cardiomyocyte markers. In a separate study UBM was applied to an experimentally produced defect in the right ventricular free wall in a canine model and compared to a Dacron patch for up to 8 weeks (89). The UBM-treated defect area showed greater systolic contraction compared to the Dacron treated area. Histology showed fibrotic reaction surrounding Dacron with no myocardial regeneration, but UBM showed cardiomyocytes staining positive for α-SMA and connexin 43.

Recently, the effectiveness of organ specific c-ECM was directly compared to a UBM in a rodent RVOT repair (90). Both ECM scaffolds had no signs of fibrotic encapsulation and were

able to preserve cardiac performance, support cell infiltration, and support an endothelial lining along the endocardial surface. Surprisingly, the UBM patch rapidly degraded and remodeled with the formation of cardiomyocytes by 16 weeks compared to the c-ECM patch with little evidence of remodeling. While the non-site specific UBM resulted in the formation of a higher level of myocardial tissue compared to the site specific c-ECM in this study, both are being investigated for their promise in the treatment of negative ventricular remodeling after myocardial infarction. Currently only one company, CorMatrix, is utilizing ECM for cardiac related repairs of pericardium, cardiac tissue, and carotid repair using a non-site specific ECM scaffold called small intestinal submucosa (SIS).

1.3.3 Minimally Invasive Injectable ECM Gels for Cardiac Repair

Another approach to the treatment of myocardial infarction is to inject a bioactive gel into the damaged region. A gel form of a cardiac ECM scaffold was prepared (60) by enzymatic solubilization with pepsin into a liquid and then induction of self-assembly into a gel when brought to physiologic conditions of 37 °C and pH of 7.4 (91). This gel form of ECM was injected directly into the LV free wall of a rodent. Endothelial cells and smooth muscle were found to migrate into the site of injection, and at 11 days post-injection there was an increase in arteriole formation (60). Recently, infarcted pigs were treated with cardiac ECM gels through a percutaneous transendocardial injection two weeks after MI and evaluated at 3 months. Echocardiography indicated improvement in cardiac function and ventricular volumes, and there was a significant increase in cardiac muscle at the region of injection (66). This cardiac ECM gel is licensed to a company called Ventrix and is planning to begin human clinical trials in quarter four of 2013.

1.3.4 Whole Organ ECM Scaffold Engineering

While cardiac patch and minimally invasive injectable gel technologies are promising, they are not feasible solutions to severe class IV heart failure where a transplant is required. Whole organ tissue engineering, however, may one day alleviate the supply-demand mismatch of available transplants. It has been demonstrated that an entire porcine heart can be decellularized by coronary perfusion. This three-dimensional ECM scaffold was found to retain collagen, elastin, glycosaminoglycans, and mechanical integrity providing a microenvironment to support site-appropriate cell differentiation and spatial organization. A group used this technique to create a tissue engineered heart by reseeding a decellularized rat heart with neonatal cardiomyocytes, fibroblast, endothelial cells, and smooth muscle cells, culturing in an incubator for ten days, and applying an external electrical stimulus to generate an organ level contractile force. While this force was only 2% of adult rat heart or 25% of a 16-week fetal human heart it demonstrated that a decellularized heart may be a potential platform for a xenogeneic tissue engineered heart replacement (71). While whole organ decellularization to produce a tissue engineered heart will take further time to develop, ECM scaffolds and gel for cardiac repair of a myocardial infarcted region provide a promising solution in the near future.

1.4 MECHANICAL LOADING AT THE SITE OF ECM IMPLANTATION

A mismatch in mechanical compliance at the site of cardiac repair can lead to a poor outcome (88, 89). Whereas a Dacron patch is stiff, a tissue derived ECM scaffold may match the mechanical compliance of cardiac tissue. An ECM scaffold as a cardiac patch or as a whole

organ replacement may match this mechanical compliance because it is derived from native tissue, thus containing an ideal three-dimensional composition and structure. The mechanical response of an ECM scaffold is largely dictated by the collagen fiber network.

1.4.1 Composition and Structure of ECM Fiber Networks

Depending on the source tissue the collagen fiber network can be starkly different. Collagen fibers themselves are diverse in composition. Collagen accounts for a third of all body protein, and twenty-eight different types of collagen have been identified in vertebrates (92). 80-90% of collagen consists of fibrillar collagen sub-units composed of type I, II, III and V collagen. These collagen sub-units are synthesized from cells such as fibroblast and osteoblast. Each fibrous collagen sub-unit consists of three α chain left-handed coiled subunits each composed of 1050 amino acids that form a right handed super-helix (93). The collagen sub-units differ due to the amino-acid sequence, the segments that interrupt the triple helix, and the higher order three-dimensional structures that are subsequently formed. Collagen type I, for example, is 300 nm long and 1.5 nm in diameter. These fibrous collagen molecules are capable of packing together to form fibrils of a diameter 40-300 nm with a staggered arrangement. The strength of fibrils is imparted by the development of intermolecular cross-links. Fibrils may pack together to form fibers with a diameter of 1-10 μm, which may then form into primary or secondary bundles called fascicles (92).

These collagen fibers form into networks that are distinct for each anatomic location and only contain certain types of collagen. Both collagen types I and III are found in tendons, ligaments, muscle, blood vessels, and scar. Type I collagen is also found in bone. For dermis the fiber network forms a pattern of interlacing bundles, for intervertebral discs they exist in broad

adjacent sheets with different directions, in tendons they exist in bundles (92), and in heart they exist in sheets with altering directions as the thickness of the myocardium is traversed (94). Type II collagen is found in cartilage and its fibrils are smaller in diameter than type I, oriented randomly in a proteoglycan ECM imparting compressibility to absorb joint shock. Type IV and V collagen are nonfibrillar and generally found in basal laminae or basement membranes and synthesized by epithelial cells. Elastin is another non-collagenous fibrous protein consisting of polypeptide chains covalently cross-linked. The individual protein molecules in elastin are able to uncoil reversibly whenever force is applied (92).

1.4.2 ECM Structure-Mechanics Relationship

These heterogeneous fiber networks are mechanically complex (95) and are subject to large deformation that exhibit a highly non-linear stress–strain relationship characterized by a compliant response or toe region at low strains and a stiff response at large strains. ECM scaffolds also exhibit viscoelasticity, and complex axial coupling. Much of this behavior is due to changes in the fiber network's internal structure with strain, which involves both straightening of crimped collagen fibers and rotation of these fibers toward the stretch axis. The fibers within the network may have a degree of alignment depending on the source tissue that correlates at the macro scale with a degree of mechanical anisotropy.

1.4.3 ECM and Mechanotransduction

For cardiac tissue, the fiber networks orient the myocytes, mechanically couple them to each other and to neighboring capillaries and nerves, and provide elastic support during ventricular filling. Acute disruption of this fiber network decreases myocardial systolic performance without even a change to myocyte contractility because the network maintains continuity between myocytes (96). Myocytes are bound to the ECM network through cell surface ECM receptors known as integrins. Integrins are dimeric transmembrane proteins composed of an α and β subunit that bind ECM proteins in the extracellular space and cytoplasmic actin-linker proteins inside the cell, thereby mechanically coupling the ECM to the actin cytoskeleton. The binding of a cell integrin to an ECM protein results in a conformational change whereby receptors cluster together to form a focal adhesion complex. This focal adhesion complex contains a cluster of integrins, associated actin-linker proteins, and multiple signal transduction molecules.

Focal adhesions are critical to mechanotransduction, the process by which cells convert mechanical signals into biochemical responses. Global forces are transmitted through the ECM and focused on cell surface integrin receptors. This global force causes a localized force dependent change in cell shape and the confirmation of the focal adhesion. This confirmation change alters the focal adhesion's biochemical activity resulting in signal transduction and associated stress-dependent remodeling. An experiment that disrupted intracellular force transmission through interfering with expression of focal adhesion protein vinculin actually impaired myocyte shape stability and disrupted normal myofibril architecture (97). It also has been demonstrated that a cardiac specific signaling molecule melusin is activated by binding β1 integrin to mediate the cardiomyocyte response to pressure overload hypertrophy to prevent cardiac failure (98). Ion channel function also is influenced by the relationship between local

integrins and mechanical forces through the ECM. To summarize, external mechanical loads exerted on cardiomyocytes can induce alterations in gene expression, muscle mass, and phenotype. These effects are mediated by force dependent signal transduction through the ECM. Thus, mechanical forces conveyed by the ECM are critical in the control of heart form and function (99).

1.5 THE MANUFACTURING OF AN ECM SCAFFOLD

The objective of decellularization of a source tissue is to remove the cellular components to prevent host rejection while minimizing alteration to the remaining ECM composition and structure. Decellularization of tissues and organs to create ECM scaffolds is a complex multiple step process. The decellularization process will vary depending on factors such as a tissue's cellularity, density, lipid concentration and thickness (100). To acquire a better understanding of the decellularization process, a description of the potential methods in a protocol are provided below.

1.5.1 Chemical Decellularization Agents

Decellularization agents may be classified into chemical and biologic agents. Chemical agents may be further broken down into either acids and bases, hypotonic and hypertonic solutions, detergents, alcohols, or other solvents. Acids and bases catalyze hydrolytic degradation of biomolecules. Peracetic acid is a common disinfection agent that also acts as a decellularization agent by removing residual DNA. Hypotonic and hypertonic saline solutions cause cell lysis by

alternating between osmotic affects that cause cell swelling and shrinking. Hypertonic saline solutions also dissociate DNA from proteins (101). Detergents solubilize cell membranes and dissociate DNA from proteins. Detergents are effective at removing cellular material from tissues but are known to disrupt and dissociate proteins. Alcohols aid in both cell lysis and lipid removal. Other solvents such as acetone also may aid in lipid removal, but similar to alcohol, they may cause tissue fixation and damage ECM structure.

1.5.2 Biologic Decellularization Agents

Biologic agents may be separated into either enzymes or non-enzymes. Enzymes such as nucleases, trypsin, collagenase, and lipase can provide high specificity for removal of cell residues or undesirable ECM constituents, but they are typically insufficient for complete cellular removal if used alone and may be cost ineffective compared to other decellularization agents depending on the volume of solution required. Non-enzymes such as chelating agents (ethylenediaminetetraacetic acid or EDTA) aid in cell dissociation from ECM proteins by binding to metal ions but are also insufficient when used alone and are most effective when combined with enzymes such as trypsin. Antibiotics and antimycotics such as penicillin, streptomycin, amphotericin B, and sodium azide may be used to inhibit microbial contamination during decellularization but also present a regulatory hurdle for clinical approval.

1.5.3 Techniques to Apply Decellularization Agents

The techniques to apply decellularization agents will depend on the tissue's thickness and density. For example, while thin tissue such as pericardium may be successfully decellularized

by immersion in a detergent solution with mechanical agitation alone, a very thick and dense tissue such as myocardium will not sufficiently decellularize by diffusion alone if left intact. For some tissues, prior to application of decellularization agents, undesirable layers of the tissue may be mechanically removed. For example, for the preparation of UBM the mucosal and submucosal of the bladder are first mechanically separated to isolate the basement membrane complex (BMC) and lamina propria, which is subsequently mechanically shaken in peracetic acid for 2 hours to both decellularize and disinfect (102). The thickness of the BMC and lamina propria is small enough for diffusion of the detergent from the surface to traverse the layers. However, the heart is too thick to achieve decellularization by detergent immersion and mechanical shaking.

The heart must either be cut into smaller pieces and mechanically agitated for prolonged periods of days (103), or decellularized as a whole organ through retrograde perfusion with detergent (65, 71, 72). Retrograde perfusion of the heart largely preserves the three-dimensional architecture of the organ compared to cutting it into smaller pieces. Retrograde perfusion accesses the vascular network within the myocardium to minimize the diffusion distance for detergents to the cells. To achieve retrograde perfusion in the heart the ascending aorta is cannulated, and a peristaltic pump moves fluid in the direction of the aortic valves which subsequently coapt under the retrograde pressure. This fluid is then forced to flow through the coronary arteries at the sinuses of the aortic valve. Perfusion through this coronary vasculature is an efficient method to both deliver decellularization agents to cells and to remove cellular material from the tissue.

1.5.4 Differences in Decellularization Protocols

For each tissue and organ there are multiple reported protocols for decellularization that differ in the number, order, type, concentration, and application time of decellularization agents. For example, one protocol commonly used for decellularization of hearts over 136 hours (65) utilizes retrograde perfusion with (1) heparinized PBS with adenosine to remove blood product, (2) an ionic detergent called SDS to remove cellular content, (3) a non-ionic detergent called Triton™ X-100 to both remove cellular content and rinse out SDS, and (4) a rinse with an antibiotic PBS solution to remove detergent residues. In this protocol each step is followed by rinsing with deionized water to remove detergent residues.

Another protocol for heart decellularization (71) used (1) the enzyme trypsin with EDTA and sodium azide to detach cells from the ECM, (2) Triton™ X-100 with EDTA and sodium azide, (3) an ionic detergent called sodium deoxycholate to remove cellular content, and (4) peracetic acid to both disinfect and decellularize. Between each step of this protocol there were rinses with type I water and 2x PBS to lyse the cells through osmotic effects. The process of decellularization of porcine heart through this protocol is reduced to less than 15 h. Thus, even for whole organ decellularization of a heart there are different protocols with many differences in the types of detergents used, their sequence, and duration of application.

1.5.5 Decellularization Protocols, ECM Composition, and Host Response

Preservation of the complex composition and three-dimensional ultrastructure of the ECM during manufacturing of these devices is highly desirable, but it is recognized that all methods of tissue decellularization result in some degree of disruption of the architecture with potential loss

of surface structure and composition (100). For example, when the processing methods do not effectively decellularize the source tissue or when chemicals are involved that create non-degradable molecular cross-links, the in-vivo soft tissue remodeling response is characterized by chronic inflammation, fibrotic encapsulation, and scar tissue formation (44, 104, 105). When the processing methods do effectively decellularize the tissue and chemicals that create non-degradable molecular cross-links are avoided, then the in-vivo remodeling response is constructive with the formation of site-specific functional tissue.

An examination of distinct processing steps used to achieve decellularization for dermis (106), cornea (107, 108), lung (109), heart valves (110), and pericardial tissue (72, 103, 111-113) found that the type and sequence of detergents used can cause marked changes in the composition, mechanical strength, and/or cytocompatibility of the resultant ECM scaffold. For example, for the decellularization of dermis it was found that liming decreased growth factor, GAG content, mechanical strength, and the ability of ECM to support in-vitro cell growth. A combination of trypsin, SDS, and Triton™ X-100 decreased growth factor content and in-vitro cell growth compared to just trypsin and Triton™ X-100 (106). Comparison of multiple step protocols for whole heart decellularization found distinct differences in DNA content, GAG content, and ECM constituents such as collagen IV, elastin, and laminin (113).

1.5.6 Detergents in Decellularization Protocols

Detergents are commonly used to decellularize tissues. The usage of different types of detergents in multiple step protocols may contribute to the distinct differences in ECM scaffold composition. To understand why detergents may effect ECM scaffold composition an understanding of their mechanism of action is necessary. Detergents facilitate cellular lysis and

solubilize the released hydrophobic proteins (114, 115). Cellular membranes are composed of phospholipids that are amphipathic containing a hydrophobic non-polar hydrocarbon tail connected to a hydrophilic polar head group. This structure aggregates to form a lipid bilayer in which hydrophilic polar head groups are oriented towards the aqueous environment forming hydrogen bonds with water molecules, while the hydrophobic tails are oriented inwards between the hydrophilic head groups. Integral membrane proteins traverse the bilayer membrane through interactions with the hydrocarbon chains of the membrane and the hydrophobic domain of the proteins.

Detergents form micelles through the aggregation of detergent molecules into organized spherical structures. At low concentrations, detergents exist as monomers and incorporate into the lipid bilayer, but as the concentration increases a threshold is reached called the critical micelle concentration (CMC) where the lipid membrane bilayer is disrupted and lysed, producing lipid-protein-detergent micelles. In this micelle, the hydrophobic regions of membrane proteins are surrounded by the hydrophobic chains of the detergent molecules and membrane phospholipids.

Detergents are classified into three main categories based on the property of the hydrophilic head group (114, 115): non-ionic, ionic, and zwitterionic. Non-ionic detergents contain uncharged hydrophilic head groups and are suited for breaking lipid-lipid and lipid-protein interactions. Non-ionic detergents are considered a non-denaturant and are widely used in proteomics literature for isolating membrane proteins in their biologically active form retaining native subunit structure, enzymatic activity or non-enzymatic function. Ionic detergents contain a head group with a net charge that can be either negative (anionic) or positive (cationic). Ionic detergents either contain a hydrocarbon straight chain as in SDS or a more complicated rigid

steroidal structure as in sodium deoxycholate. Ionic detergents can disrupt protein-protein interactions along with lipid-lipid and lipid-protein interactions, and they may denature proteins. Zwitterionic detergents offer combined properties of ionic and non-ionic detergents. For example, CHAPS does not possess a net charge like non-ionic detergents but is able to break protein-protein interactions like an ionic detergent. In proteomics literature CHAPS is considered to denature proteins less than ionic detergents possibly due to its rigid steroid ring structure.

To summarize, there are many different detergents that may be used in decellularization protocols each with their own unique set of properties. For example, SDS is an ionic detergent that is known to denature proteins in the proteomics literature (114-116), but it is a commonly used detergent in the decellularization of hearts (60, 65, 66, 72). Thus, it is critical to understand how different detergents with distinct chemical properties effect ECM scaffolds in the process of decellularization.

1.6 MOTIVATION

ECM scaffolds offer a promising opportunity to repair an infracted myocardium that may lead to heart failure over time. Decellularization of tissues to produce ECM scaffolds is a complex process that is not standardized even for a specific anatomic source tissue. To achieve decellularization there are numerous reported protocols with differences in decellularization agents, their sequence and duration of application, and method of delivery. Depending on the processing methodology the host response to the implanted ECM scaffold may either be characterized by chronic inflammation, fibrotic encapsulation, and scar tissue formation or a constructive remodeling response with the formation of site-specific functional tissue. A review

of the properties of different types of decellularization agents suggests that their intrinsic chemical properties may cause varying degrees of damage to the composition and structure of the resultant ECM scaffold. Damage to the composition and structure of the ECM scaffold may subsequently impact the host response. Some of these multiple step protocols have been compared (72, 103, 106-113), and it was found that differences did exist in composition, mechanical strength, and/or cytocompatibility of the final ECM product even if derived from the same source tissue.

However, no reference exists on how each detergent may affect the properties of the final ECM scaffold. While some multiple step protocols have been compared, these protocols contain multiple detergents with differences in concentrations and incubation times. Thus, while these reported comparisons indicate that differences may exist between some decellularization protocols, any conclusion drawn could not be attributed to any single step in the multiple step process. Additionally, none of these reported comparisons are comprehensive. These comparisons of decellularization protocols only focus on a limited type of detergents or methods of characterization (i.e. only examined composition or mechanics). Among all these referenced studies only two studies compared different methods of whole organ decellularization of the heart and neither was comprehensive, nor attempted to isolate any variables from these multiple step protocols (65, 72).

The goal of decellularization is the removal of all cellular material to prevent an adverse immune response and to preserve the composition, structure, or mechanical integrity of the remaining three-dimensional ECM. However, to date, there is no methodical evaluation of the effect of different detergents on the ECM scaffold to assist in the formulation of an optimized decellularization protocol for a tissue of interest. Without such information numerous protocols

have been developed from conjecture with subsequent impact on the host response to the ECM scaffold implant and clinical outcome of the patient. Thus, the **overall objective** of this thesis is to characterize the effect of different detergent treatments on the composition and mechanics of ECM, and in-vitro cell-ECM interaction. This information will facilitate informed decision making regarding decellularization protocols and their effect upon the ECM scaffold material.

1.7 SPECIFIC AIMS

Specific Aim 1: To acquire a quantitative understanding of ECM micromechanics.

Rationale: Before characterizing ECM scaffolds as a function of different detergent treatments the native structure of the heart and the complex interactions between the cells and ECM need to be assessed. The native heart valve was used due to its inherently fibrous architecture which is similar to an ECM scaffold.

Hypothesis: Cell – ECM interaction as measured through deformation is distinct for both the type of valve and the layers of the valve.

Specific Aim 2: To determine whether the composition, structure, and mechanics of ECM scaffolds are altered as a function of different detergent treatments.

Rationale: Numerous decellularization protocols are reported in the literature with differences in detergents, method of detergent delivery, and durations of detergent application. It is unknown what effect each type of detergent has on the resultant ECM scaffold. In this aim the effect of commonly used detergents for decellularization is assessed

under equivalent conditions to develop a comprehensive profile of each detergent for decellularization. Two source tissues were chosen for their relevance in application to cardiac repair.

Hypothesis: Ionic detergent treatment will result in a loss of ECM constituents, and a decrease in mechanical strength that will be correlated at the micro-structural scale.

Specific Aim 3: To determine if cell-ECM interaction is dependent upon the detergent treatment.

Rational: It is unknown whether the integrity of the ECM ligand – cell integrin interaction is retained depending on the detergent used to achieve decellularization. Modifications to the composition and structure that are investigated in Specific Aim 2 may correlate with cytocompatibility in this aim.

Hypothesis: Non-ionic detergents will retain the structure and composition of ECM for a higher level of cytocompatibility.

2.0 NATIVE HEART ECM MICROMECHANICS

Critical to the success of an ECM scaffold cardiac patch is the ability to support tissue driven mechanotransduction, i.e., translation of organ level mechanical stimuli into cellular responses through the localized fiber network. Mechanical forces were found to be critical to the constructive remodeling of an SIS ECM scaffold in an Achilles tendon repair in a rabbit model. Specifically, rabbits with full range of motion had an associated greater cellular infiltrate and organized connective tissue with deposition along the lines of stress compared to those whose motion was not constrained (117). Further, in a canine partial cystectomy model repaired with either SIS or UBM ECM scaffold it was found that only the bladders that had site appropriate mechanical loading (i.e. bladder filling) had a constructive remodeling response (118). This constructive remodeling response was characterized by the formation of a differentiated urothelium and islands of smooth muscle cells. Bladders whose fillings were inhibited with long term catheterization were instead characterized by fibrosis.

An in-vitro study also supported the idea that mechanical forces are critical to the promotion of a constructive remodeling response. Fibroblast seeded onto an SIS ECM scaffold and subjected to cyclic stretching had increased expression of Col I, exhibited a contractile phenotype with increased expression of SMA, TN-C, and TGF-β1 (45), and had fiber alignment along the axis of loading (119). Prior to investigating whether certain detergent treatments may damage the ECM scaffold fiber network such that it is unable to transmit organ level mechanical stimuli into host cellular responses, it is first critical to understand the complexity of this cell-ECM fiber network coupling for the native heart tissue.

Mechanotransduction is known to be critical in the control of heart form and function through regulation of cardiomyocyte gene expression, muscle mass, and phenotype (99). The native heart myocardium contains dense striated muscle unlike ECM scaffolds which are decellularized. The native heart valves, however, are passive elements that are composed of a dense multilayered ECM framework that lack this striated muscle. Thus, the native heart valves were investigated due to their inherently fibrous architecture similar to ECM scaffolds. To better understand native tissue complexity the heart valves' micromechanics are examined in two stages. The first stage compares two different heart valves in terms of cellular gene expression profile and fiber kinematics. The second stage examines fiber kinematics in more detail with a focus on cell-fiber interactions. The information derived from this aim will demonstrate the complexity of the native heart tissue to elucidate the benefits of a tissue engineered approach to heart repair that utilizes site-specific ECM scaffolds.

2.1 GENE EXPRESSION AND COLLAGEN FIBER MICROMECHANICAL INTERACTIONS OF THE SEMILUNAR HEART VALVE INTERSTITIAL CELL[1]

2.1.1 Introduction

The aortic (AV) and pulmonary (PV) heart valves, termed "semilunar" due to their leaflet shape, have the basic function of preventing retrograde blood flow into the ventricles during diastole. Valve mechanical function spans multiple length scales from the organ-scale hemodynamic phenomena to the underlying tissue and cellular components (120). Both the AV and PV experience significant in-plane tension resulting from transvalvular pressure (TVP) during diastole (120); approximately 90 mmHg and 15 mmHg for the AV and PV, respectively. As a result of this difference, the AV and PV ECM organization and concomitant mechanical properties differ considerably (121-123). Normal tissue morphology and function rely upon the constituent cell population's ability to detect forces appropriate to their correct tissue context (124). However, it is not known whether the AV and PV valvular interstitial cell (VIC)-tissue mechanical coupling and VIC function for each valve are also distinct. A better understanding of the anatomical site-specificity of native heart tissue is critical to understanding the requirements for a tissue engineered repair or replacement.

The semilunar valves consist primarily of three histologically distinct fibrosa, spongiosa, and ventricularis layers, except in the coaptation region that is a single collagenous layer (125). The fibrosa is oriented towards the associated artery and is composed mainly of a dense, highly

[1]This work has been adapted from the following published manuscript:
Carruthers CA, Alfieri CM, Joyce EM, Watkins SC, Yutzey KE, Sacks MS. Gene expression and collagen fiber micromechanical interactions of the semilunar heart valve interstitial cell. Cellular and Molecular Bioengineering. 2012;5(3): 254–265.

aligned network of Type I collagen fibers. For the AV the fibrosa layer dominates the mechanical response compared to the ventricularis layer (126). The ventricularis faces the ventricle and is composed primarily of elastin and a more loosely structured collagen fiber network. The spongiosa, located between the fibrosa and ventricularis, is rich in glycosaminoglycans, and has been observed to have collagen fibers transverse it that interconnect the fibrosa and ventricularis layers (126). Structural adaptations to applied stress, especially in the collagen fiber network, are also distinct for each valve (122). In the unloaded configuration, the AV leaflet demonstrates substantial regional variations in collagen fiber alignment as compared to the relatively uniform PV (122). As loading commences, the AV collagen fibers straighten more than observed for the PV (122). These differences in valvular tissue structure also are apparent in the mechanical behavior under biaxial load at aortic physiological membrane tension (60 N/m) (123), where the PV is more compliant in the radial direction compared to the AV, while both valves respond similarly in the circumferential direction (123).

Clinical interest for the PV has focused on auto-transplantation into the aortic position as a replacement for the AV, especially for the pediatric population (127). This results in a six-fold increase in the PV autograft TVP, with explants from 2-10 weeks having a higher VIC biosynthetic activity compared to explants from 3-6 years (128). These results suggest that the PV autograft can adapt to the increased loading at the cellular level, possibly until a new homeostatic state is achieved although such information is lacking. Moreover, the development of engineered tissue approaches to congenital PV and AV reconstruction require a detailed knowledge of semilunar heart valve mechanics and the underlying mechanobiology.

VICs maintain the ECM structure through protein synthesis and enzymatic degradation (129), and are phenotypically plastic in that they are quiescent under homeostatic conditions and active in periods of growth and disease (130). Yet, relatively little is known about how organ level mechanical stimuli result in alterations in semilunar valve biosynthetic activity. Both in our and other laboratories cyclic mechanical stimuli during in-vitro culture has been utilized in valvular tissues to elicit alterations in biosynthetic activity (131, 132). These results suggest a link between the VIC phenotype, biosynthetic activity, and cellular loading resulting in the specific valve in-vivo hemodynamic environment. These studies were directed in part towards understanding how changes in TVP induce concomitant changes in structural and mechanical properties of the AV and PV in-vivo. Along these lines, the porcine AV VICs undergo larger deformations in the fibrosa layer compared to the spongiosa and ventricularis layers (133).

The above results clearly suggest specific VIC-ECM interactions that may be also unique for each semilunar valve, including layer-specific adaptations. To gain insight into this question, this sub-aim quantitatively links the semilunar valve VIC biosynthetic activity at the genetic level to differences in VIC location (valve type, layer), VIC deformation level, and VIC quantitative mechanical interactions with the collagen fiber network with TVP. VIC mRNA expression level of ECM constituents and phenotypic markers was measured with qRT-PCR from both semilunar valves. Changes in VIC shape were quantified using semilunar valves exposed to increasing TVP, and compared to differences in valve ECM layer structure and collagen fiber structure. Note for the PV both physiologic (~15 mmHg) and hyper-physiologic (~90 mmHg) TVP levels were utilized in order to compare both its physiological and autograft environments.

2.1.2 Methods

2.1.2.1 Histomorphometry

Porcine hearts (from animals 10 months old, and approximately 250 lbs) were obtained within 10 minutes of death from a local USDA approved abattoir (Thoma Meat Market, Saxonburg, PA). AV and PV leaflets were dissected on site, with the surrounding myocardium trimmed from the leaflets. A central 2 mm strip in the radial direction was removed and fixed in 10% neutral buffered formalin (VWR) for histology. The remaining leaflet was frozen in liquid N_2 and stored at -80^{o}C prior to homogenization for mRNA analysis.

The resulting formalin fixed leaflet tissue was processed as previously described (134, 135). Briefly, Movat's modified pentachrome staining was used to visualize fibrous collagen (yellow), proteoglycan and GAGs (blue), and elastic fibers (black), on 5 μm sections on the radial-transverse surface (Figure 1). Leaflet thickness, as well as the percent total thickness of fibrosa, spongiosa, and ventricularis layers were evaluated in 3 regions per leaflet for n=7 AV and n=7 PV leaflets using ImageJ software. Leaflet layers were identified by distinct color boundaries whereby the fibrosa layer contained yellow and blue, the spongiosa layer contained blue with no black or yellow, and the ventricularis layer contained only black. Statistical significance of differences between AV and PV dimensions was determined by independent-samples *t*-test with $p<0.05$, with values reported as mean ± standard error.

2.1.2.2 Real-Time Quantitative PCR

Porcine AV and PV leaflets were obtained as above and frozen in liquid N_2 then stored at -80^{o}C prior to homogenization and total RNA isolation using Trizol as previously described (136). Samples were then treated with DNase using a DNA-free kit (Invitrogen). RNA was quantified,

and 0.5 μg was used for cDNA synthesis with the Superscript RT-PCR kit according to manufacturer's instructions. 1μL cDNA was used for real-time PCR by Taqman gene expression assays and the StepOnePlus system (Invitrogen).

Taqman assays used were porcine *GAPDH* (Ss03373286_u1), *Col1a1* (Ss03373340_m1), *Col3a1* (Ss03375691_g1), *Hsp47* (Ss03373335_g1), *matrix gla protein (MGP)* (Ss03394091_m1) and *biglycan* (Ss03375454_u1). An additional custom assay was designed for porcine *periostin* (forward 5'-GGCAAACAGCTCAGGGTCTTC-3'; reverse 5'-TTCCTCTAACCATGCATGAATTTTC-3'; probe 6FAM-TGTATCGTACTGCTGTCTG-MGBNFQ). The identity of the amplified *periostin* DNA fragment was confirmed by sequencing. Taqman assays were used at 1X and custom assays were performed using 900 nM forward and reverse primers with 250 nM probe. Amplification conditions were step 1 95^{o}C 20s; step 2 95^{o}C 1s; step 3 60^{o}C 20s, with steps 2 and 3 repeated for 40 cycles. All amplifications were performed in triplicate for each sample and data were normalized to *GAPDH* levels. Relative expression values also were determined based on normalization to *β-actin* (Ss03376563_uH) expression, and no significant differences were observed for expression values normalized to either *GAPDH* or *β-actin*.

Data were analysed using the comparative ΔΔCt method according to manufacturer's instructions (Invitrogen). Expression values for each leaflet were reported relative to the AV from the same animal, set at 1.0. A total of 15 AV and 15 PV leaflets from 5 individual AV and PV were evaluated. Statistical significance for each marker of interest between AV and PV was determined by a paired samples t-test with $p<0.05$ (PASW Statistics, V. 18). Values are reported as mean ± standard error.

2.1.2.3 Tissue Level Biomechanics

Porcine PV leaflets used for biomechanical analysis were removed from the pulmonary root using aforementioned tissue source and preparation protocols. The right PV leaflet was chosen for this study for consistency and placed in gauze wet with PBS and snap frozen at -80 °C to avoid tissue degradation prior to testing (137). A detailed description of the biaxial testing device and methods used for planar biological tissues has been reported previously (138). A 10 mm x 10 mm section was dissected from the central belly region of the leaflet. Specimens were preconditioned ten cycles with a half cycle time of 15 s to a maximum membrane tension of 60 N/m. A peak tension of 60 N/m was used because it corresponds to an in-vivo aortic diastolic pressure of approximately 90 mmHg (138, 139). Eight right PV leaflets from eight pig hearts were tested. Samples were compared to previously tested right coronary AV leaflet samples from seven pig hearts (126). The average biaxial response of the AV was compared to the PV by performing a linear interpolation on each sample at representative tension values and averaging the interpolated stretch values across samples at each tension. Max AV circumferential stretches were compared to max PV circumferential stretches with an independent-samples t-test with $p<0.05$ (PASW Statistics V 18). Values are reported as mean ± standard error.

2.1.2.4 Valve Deformation and VIC-ECM Imaging

All AV and PV tissue sections were acquired from a previous study by Joyce et al., as described in (122). In brief, pairs of AVs and PVs were fixed at retrograde hydrostatic pressures of 0,1,2,4,10,20,60, and 90 mmHg in aqueous glutaraldehyde solution using an elevated reservoir column. The application of retrograde pressure mimicked diastole when the leaflets coapted and underwent a large planar distention. For each pressure level and valve, the belly region of one of the three leaflets (Figure 1) was paraffin embedded, and two 5 μm sections were taken and

stained with Movats Pentachrome to distinguish VIC nuclei and the three leaflet layers: Fibrosa, spongiosa, and ventricularis (122, 133). Additional 5 μm sections were stained with Picrosirius red and imaged under polarized light microscopy, as previously described, to visualize the natural birefringence of collagen fibers by the periodic bands that correspond to collagen fiber crimp (122). Additional sections were taken at 30 μm for 3D analysis at pressures of 0 and 90 mmHg for the AV to represent both the free float and physiological TVP, respectively, and 0, 20, and 90 mmHg for the PV to represent free float, physiological TVP, and hyper-physiological TVP (in the case of the Ross procedure), respectively.

Each section was deparaffinized, permeabilized with Triton™ X-100 for 20 minutes at 1:1000 concentration, stained with Sytox green nucleic acid stain (Invitrogen) for 1:2000 for 15 minutes, and gelvatol mounted with a coverslip for two-photon microscopy (TPM) (140). TPM was executed with an Olympus FV1000 TPM system equipped with a Chameleon ultra diode-pumped laser operated with Olympus fluoview software. TPM was used to simultaneously image collagen and VIC nuclei via second-harmonic generation (SHG – filter set at 400±100 nm) and two-photon excited fluorescence (TPEF – filter set at 525±50 nm), respectively. Each sample was imaged with a 25x XL Plan N objective (N.A. of 1.05) forming a 500 by 500 μm field of view with a 0.5 μm/pixel resolution to a subsurface z-axis depth of 25-30 μm with a 1 μm step size resulting in 25-30 images composing a stack. An excitation wavelength of 830 nm was used for all samples with a laser transmissivity of 7%. Image stacks were reconstructed into 3D projections for a localized volume (Figure 5b) using VOXX (Indiana University Medical Center, Indianapolis, IN, USA), a freeware voxel-based volume-rendering program.

2.1.2.5 Determination of Nuclear Orientation and Deformation

In the present sub-aim, VIC nuclear orientation and deformation states were measured between the valves as a function of layer and TVP. Preliminary orientation information was acquired from the TPM image stacks, which were imported into a custom Matlab program (The Math-Works, Natick, MA) to acquire the 3D point cloud of each nucleus, from which principle component analysis (PCA) was performed on the segmented VIC nuclei to acquire the 3D nuclear orientation (Figure 6a-b) (141). On average, ~300 VICs were counted per sample. To distinguish the layers in the TPM images, the collagen content derived from the SHG signal was utilized. Specifically, it was found that the spongiosa layer had minimal collagen fiber content as compared to the fibrosa and ventricularis layers. The fibrosa layer was easily distinguished due to its high collagen content, direction, and thicker size. This observation was confirmed to match the Movat's Pentachrome stain.

2D analysis of VIC nuclear aspect ratio (NAR) is a sufficient and robust measure of total VIC deformation (120, 133). Thus, in the present sub-aim additional 2D analysis of VIC deformation was performed on the AV and PV as a function of spatial location and TVP to extend previous studies on the AV (133). Briefly, using Movat's pentachrome stained sections in the transverse-circumferential plane (131, 132), a panoramic image was created from one to five overlapping images in order to span the complete thickness of the leaflet (including fibrosa, spongiosa, and ventricularis). This process was repeated for approximately five different locations across the section. The nuclei were identified, spatial locations recorded, and nuclear aspect ratio (NAR, ratio of the longest to shortest axial lengths) determined. The NAR has been shown to be an accurate index of VIC deformation, with NAR determined in the transmural-circumferential plane (Figure 1). Approximately 60 VICs were counted per panoramic image

across five locations of each leaflet, resulting in 300 VIC counted per pressure level. Statistical analysis for each TVP was determined using an independent-samples *t*-test at $p<0.05$ (PASW Statistics, V. 18). Values are reported as mean ± standard error.

2.1.2.6 Relation of VIC Deformation to Tissue Stress Level

The observed changes in NAR were clarified to estimated local tissue stress levels. The average tissue and fibrosa layer Cauchy stresses, σ, was approximated using the Laplace relation $\sigma=\frac{1}{2}PR/t$, P is the TVP, R is the current radius of curvature, and t is the current thickness. The deformed semilunar heart valves shape was approximated assuming a spherical geometry with a radius of curvature of 10 mm (138, 139). For the thickness both the fibrosa and total thickness of the AV and PV were utilized in the deformed configuration to bracket the estimated stress range. While this assumption of a constant singular radius of curvature does not account for the transverse isotropy of the heart valve, the Laplace relation provides a first approximation of the Cauchy stresses.

2.1.3 Results

2.1.3.1 Structural Differences between the AV and PV Leaflets

In both leaflets the collagen-rich fibrosa, proteoglycan-rich spongiosa, and elastin-rich ventricularis layers were clearly evident (Figure 1). The overall AV and PV leaflet thickness in addition to the relative thickness of fibrosa, spongiosa and ventricularis layers were quantified morphometrically (Table 2). Overall, the AV leaflets were confirmed to be significantly thicker than the PV leaflets. Comparison of the average thicknesses for the fibrosa layer confirmed that the AV fibrosa layer was twice as thick as the PV leaflet fibrosa layer, as previously reported

(122). However, the PV leaflet was not simply a scaled down version of the AV leaflet. The relative thickness of the fibrosa layer of the AV was greater than that of the PV, while the relative thickness of the spongiosa layer of the PV was greater than that of the AV (Table 2). The relative thickness of the ventricularis layer of the AV and PV leaflets was approximately the same for both valves. Hence, on a per layer basis it was confirmed that the overall thickness of the AV leaflet was not only higher than the PV leaflet but the relative layer proportions were also distinct with the fibrosa being thicker for the AV and the spongiosa being thicker for the PV.

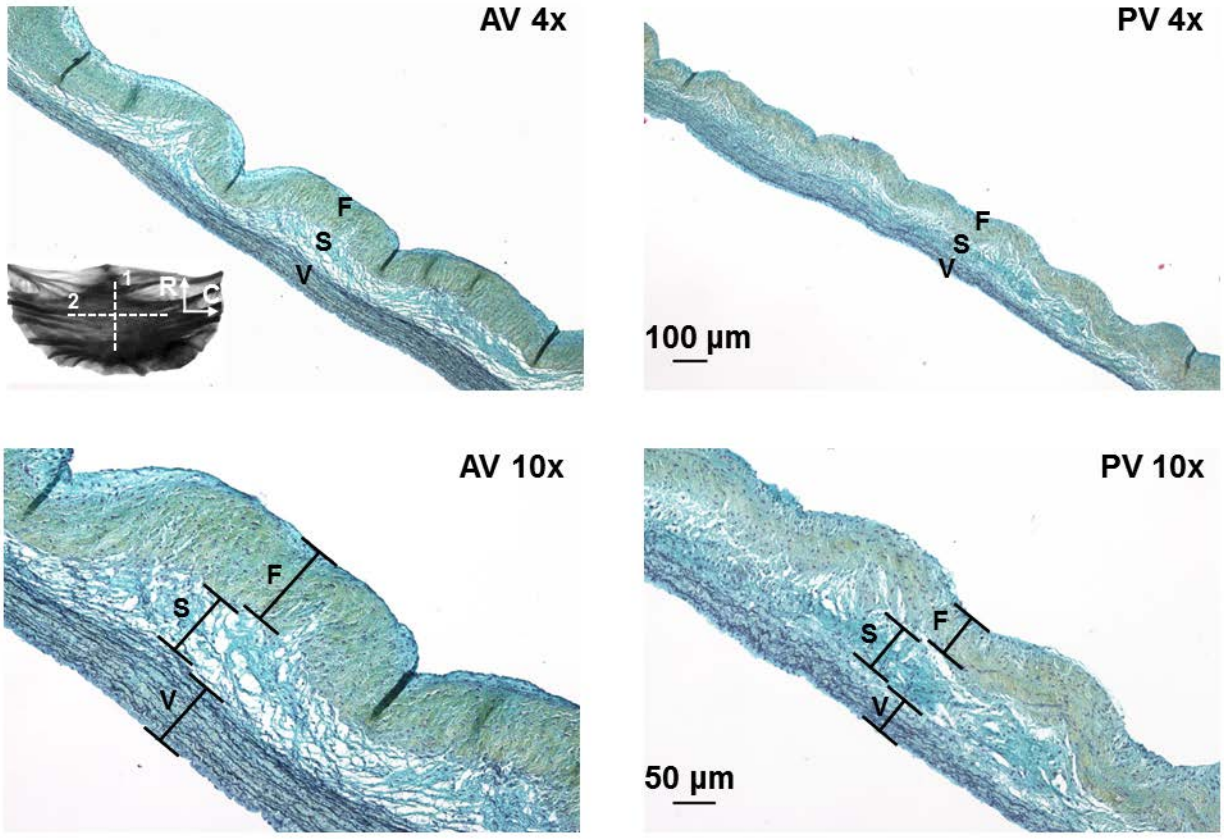

Figure 1: Histological assessment of porcine AV and PV leaflet stratification. F, S, and V represent the fibrosa, spongiosa, and ventricularis, respectively. Relative thickness of the valve ECM layers is indicated by brackets. A partially polarized image of an aortic valve leaflet is also included where C and R represent circumferential and radial direction, respectively.

Table 2: Morphometry of AV and PV stratification. Layer thickness was measured from Movat's Pentachrome images. Calculations of % relative thickness were made from layer thickness/total thickness. Values are reported as mean ± standard error of mean (n=7). Statistical significance of differences between AV and PV dimensions was determined by an independent student's t-test (*p<0.05). V represents ventricularis, S represents spongiosa, and F represents fibrosa.

	Total (μm)*	V (μm)*	S (μm)	F (μm)*	V/Total (%)	S/Total (%)*	F/Total (%)*
AV	446 ± 24	111 ± 9	140 ± 16	194 ± 13	25 ± 1	30 ± 2	45 ± 3
PV	282 ± 17	68 ± 5	118 ± 13	96 ± 6	25 ± 1	41 ± 3	35 ± 2

2.1.3.2 Tissue-Level Biomechanical Differences between the AV and PV

The equi-biaxial tension responses of both semilunar valve leaflets were similar (Figure 2). Both valves followed similar transitions in the radial direction from a low modulus region to a high modulus region. In the circumferential direction both valves had an immediate high modulus with minimal stretch. In the radial direction both valves were compliant with a nonlinear response. The PV was significantly more extensible than the AV in the radial direction reaching a maximum stretch of 1.84 ± 0.10 compared to the AV maximum stretch of 1.56 ± 0.05.

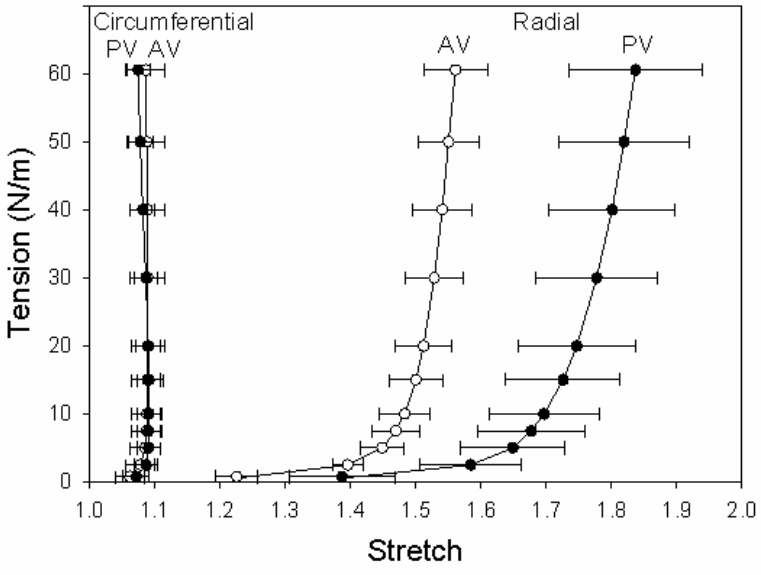

Figure 2: Mechanical characterization of the porcine AV and PV leaflet belly region with a planar biaxial test.

2.1.3.3 Differential Expression of ECM Genes in AV and PV

The mRNA expression levels of genes corresponding to ECM constituents present in all the leaflet layers of the porcine AV and PV were evaluated. Expression of the major load bearing fibrillar collagens *Col1a1* and *Col3a1* was determined, in addition to the expression of the molecular chaperone *Hsp47*, which is an indicator of collagen biosynthesis (142, 143). *Biglycan* was assessed as an indicator of proteoglycan gene expression, based on its expression in all layers together, with filamentous strands in the spongiosa layer (143). Previous studies have indicated differential expression of *MGP* that serves a protective role in calcification, with higher expression in porcine VIC isolated from PV relative to AV (144). Expression of *periostin*, demonstrated to have a role in collagen fibrillogenesis and aortic valve disease, also was assessed (145). *Col1a1*, *Col3a1*, *Hsp47*, and *Biglycan* expression levels were significantly increased in the AV versus PV (Figure 3). *Periostin* was expressed at similar levels in AV and PV (Figure 3), as previously reported (143, 145). The higher level of *MGP* expression in AV compared to the PV was distinct from what was observed in cultured VIC (Figure 3b).

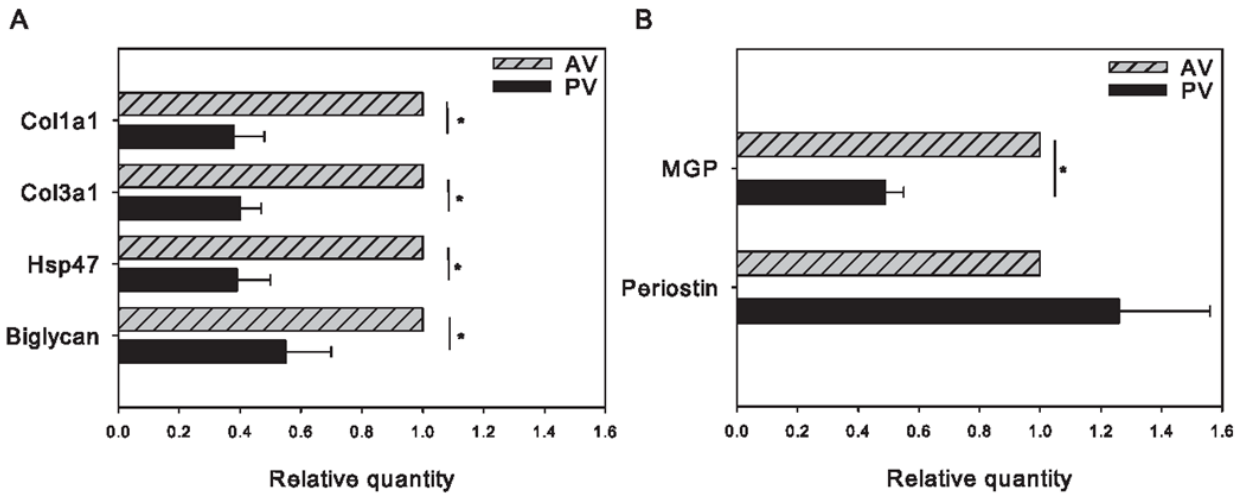

Figure 3: (A) Differential ECM constituent gene expression in porcine AV and PV, and (B) differential gene expression of VIC phenotypic markers was detected by qRT-PCR (*p<0.05).

2.1.3.4 Differences in VIC Deformations as a Function of Valve Layer

From visual inspection of circumferential-transverse sections stained with Movat's Pentachrome stain (Figure 4) both the AV and PV total thickness decreased as a function of pressure. At 0 mmHg, undulations present in the fibrosa layer represented the crimp pattern of the collagen fibers under low tension; the VICs appeared to have a similar circular shape throughout the three layers. As the pressure increased to 90 mmHg, the undulations were no longer present in the fibrosa layer as the collagen fibers are fully loaded (For visualization of this crimp under Picrosirius red stain, see (122) Figure 7a-b). At 90 mmHg, the VICs in the fibrosa layer were mechanically compacted and elongated with an ellipsoidal shape between organized collagen fibers while the VICs in the spongiosa and ventricularis layer still were fairly circular.

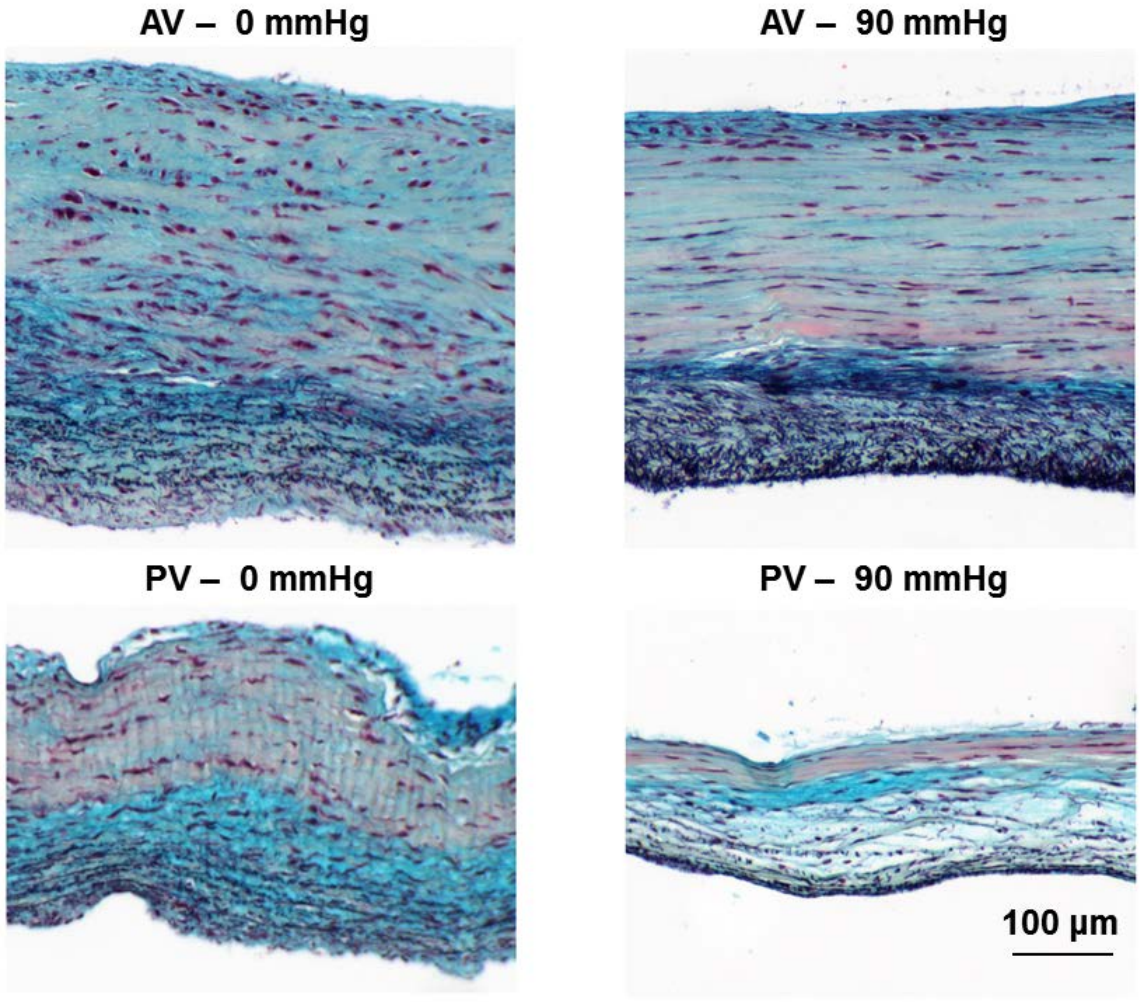

Figure 4: Histological assessment of circumferential-transverse sections of porcine AV and PV leaflet tissue stratification and VIC deformation as a function of low and high pressure under Movats pentachrome stain.

A localized 3D reconstruction of the AV collagen fibril organization and VIC nuclei as a function of the layer and physiological pressure from TPM imaging of a 30 µm circumferential transverse section (Figure 5) confirmed visual observations of layer dependent VIC deformations with pressure from 5 µm circumferential transverse sections stained with Movat's Pentachrome (Figure 4). At 0 mmHg for the fibrosa layer, the collagen fibers were undulated and oriented in the circumferential direction. At 0 mmHg, the VIC nuclei exist above, below and between the

collagen fibers, conforming to the fibers' natural undulations, and were ellipsoidal in shape. Although collagen was present in the spongiosa and ventricularis layer, the collagen fibers were not organized into large fibrous bundles with a distinct orientation. Compared to the fibrosa layer, the spongiosa and ventricularis layer have large areas without collagen, which may contain other ECM constituents.

At 90 mmHg, the collagen fibers were straightened with a decrease in crimp period and amplitude. The space between the fibers was decreased. The VIC nuclei were decreased in sphericity, and were mechanically compacted between the fibers while elongated in the space along the fibers in the circumferential direction. VICs had a higher degree of compaction in the circumferential-transverse plane compared to the circumferential-radial plane, indicating that the spacing between the collagen fibers was smaller in the circumferential-transverse plane. At 90 mmHg, the VIC nuclei in the spongiosa and ventricularis layer do not deform along the circumferential direction. The VICs in the spongiosa and ventricularis layer may not deform with pressure because of the lack of oriented collagen fibers to mechanically compact nearby VICs. Thus, VIC deformation mainly occurred in the fibrosa layer likely due to mechanical compaction by nearby collagen fibers.

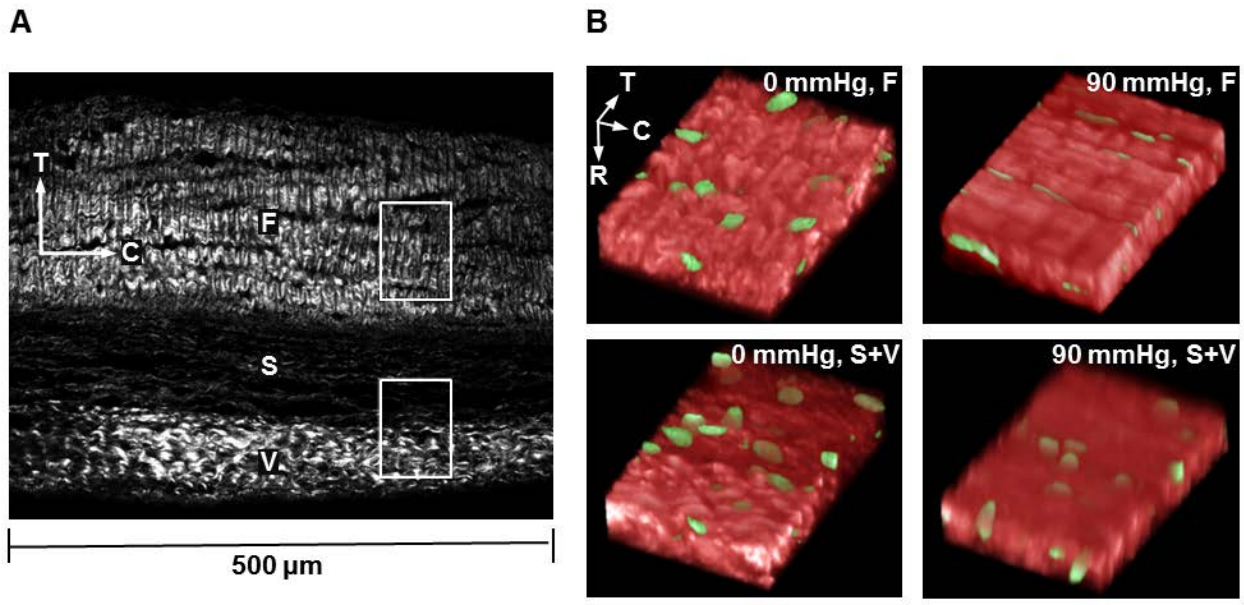

Figure 5: (A) Collagen fibers of a cross-section of the AV leaflet in the circumferential-transverse (C-T) plane (see Figure 1 line label 2) with the fibrosa (F), spongiosa (S), and ventricularis (V). The section was visualized with second harmonic generation (SHG) from TPM microscopy. The white boxes indicate the regions used for the 3D reconstruction in (B). (B) TPM microscopy was used to simultaneously image AV collagen (red) and cell nuclei (green) for a 60x80x20 µm localized volume, via SHG and two-photon excited fluorescence, respectively. C, R, and T represent circumferential, radial and transverse direction, respectively.

To confirm the visual observation that VICs were oriented along the circumferential direction in the fibrosa layer, a preliminary measurement of VIC 3D nuclear orientation was completed from TPM of 30 µm circumferential transverse sections at physiological TVP for both the AV and PV. Overall, the preferred nuclear direction was along the circumferential direction in the circumferential-radial plane, as evidenced by the centroid of θ and Φ at approximately 9.7±2.8° and 5.3±4.1° for all measured nuclei for both the AV and PV (Figure 6a,b). For θ (Figure 6c) there was an increase in alignment for the nuclei in the fibrosa layer of the PV while the nuclear alignment of the AV remained relatively constant. In the spongiosa and ventricularis layer, for θ there was a decrease in overall alignment with load for both the AV and PV. For Φ

(Figure 6d) there was a substantial increase in alignment for both the AV and PV in the fibrosa layer, but a decrease or relatively constant alignment in the spongiosa and ventricularis layers. For the fibrosa layer of the PV, the majority of cellular realignment for both the θ and Φ directions and the majority of fiber realignment occurred by 20 mmHg, the PV physiological TVP (Table 3).

Thus, VIC nuclear orientation in the fibrosa layer correlated with collagen fiber alignment. Although VIC nuclear deformation correlates with collagen fiber alignment, this is not the only factor contributing to VIC deformation. The nuclei normalized orientation index (NOI) for θ (Table 3) in the PV fibrosa layer continued to increase alignment along the circumferential direction in the circumferential-radial plane after physiological TVP at 20 mmHg, although the NOI remained constant after 20 mmHg. Further, the nuclei NOI was higher than the collagen fiber NOI. This indicated that after the majority of collagen fibers align, the nuclei still underwent further deformation and were actually more aligned than the fibers. This confirmed visual observations (Figure 4, Figure 5) that the mechanism of VIC deformation was mechanical compaction, not just collagen fiber organization.

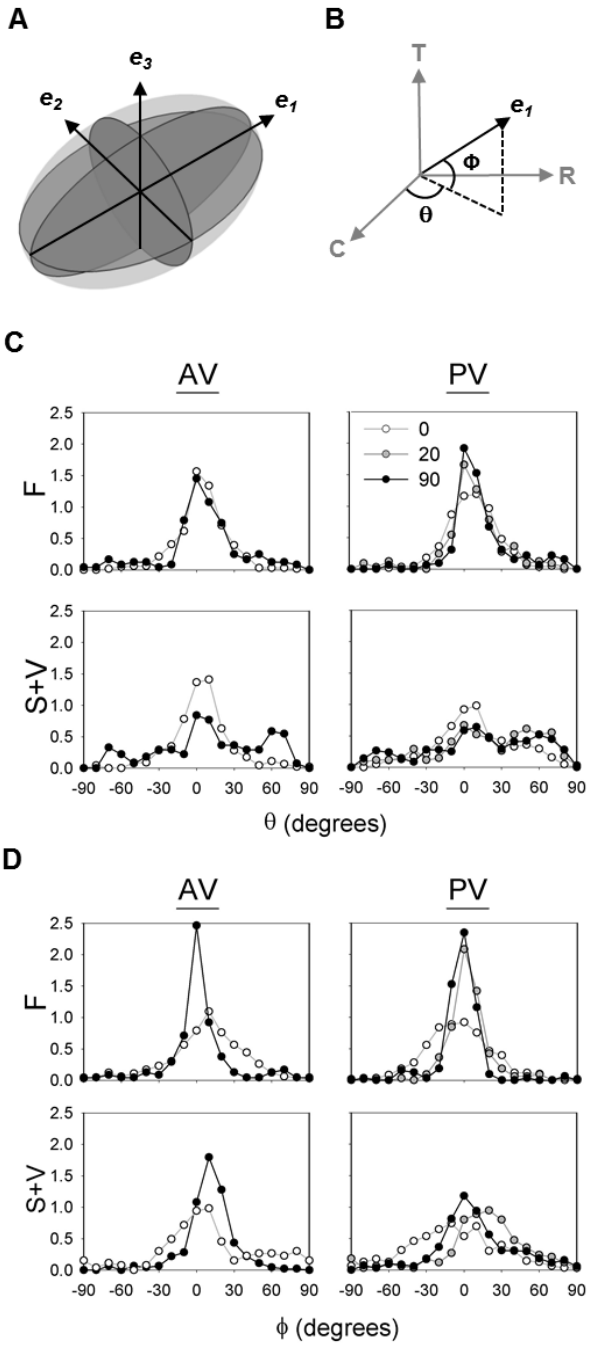

Figure 6: (A) 3D nuclear geometries were acquired and principal axes directions (e_1,e_2,e_3) were found. (B) The major principal axis (e_3) was defined in spherical coordinates from angles θ and Φ as a function of the 3D tissue coordinate system. (C) Nuclei angle distribution for θ and (D) Φ was assessed as a function of physiological and hyperphysiological pressure. Frequency is normalized by area in radians. Figure legend represents pressure in mmHg. F represents fibrosa layer, and S+V represents the combined spongiosa and ventricularis layer.

Table 3: 3D VIC nuclear orientation for the semilunar leaflet layers. The normalized orientation index (NOI) for θ represents nuclei alignment, and the NOI for small angle light scattering technique (SALS) represents the ECM fiber alignment. AV and PV represent aortic valve and pulmonary valve, respectively. F, S, and V represent fibrosa, spongiosa, and ventricularis, respectively. Values are reported as mean ± standard error.

	Nuclei - θ NOI (%)						SALS NOI (%)	
	AV			PV			AV	PV
TVP	F+S+V	F	S+V	F+S+V	F	S+V	F+S+V	
0	75.6	75.6	73.3	66.7	71.1	57.8	50.8±0.9	36.3±2.4
20	NA			57.8	75.6	13.3	62.4±1.5	59.4±2.1
90	57.8	73.3	33.3	46.7	80.0	24.4	62.0±1.3	60.3±1.1

2.1.3.5 Differences in VIC Deformation between the Semilunar Valves

As VICs were oriented along the circumferential direction in the circumferential-radial plane, we were able to simply the NAR deformation analysis to 2D in evaluating valve-specific differences. The NAR was found to be both layer- and valve-dependent as a function of TVP (Figure 7). At 0 mmHg the VIC NAR was between 2.0-2.5 (i.e. moderately ellipsoidal as compared to a spherical value of 1.0). The AV and PV fibrosa layer NAR did not change from 0 to 2 mmHg, but from 2 mmHg to 4 mmHg NAR in both valves experienced a similar rapid increase. At 4 mmHg the PV NAR continued to increase at a more gradual rate, exceeding the rate of increase of the AV NAR. By 60 mmHg, the AV NAR achieved a plateau while the PV NAR continued to gradually increase.

Interestingly, under diastolic loading, the AV fibrosa NAR (90 mmHg diastolic TVP) was similar to the PV fibrosa NAR (18 mmHg diastolic TVP) at approximately six. The AV and PV spongiosa and ventricularis layers combined had a similar modest but significant increase in NAR from 0 to 10 mmHg, and then remained constant from 20 to 90 mmHg reaching a NAR of 2.47±0.07 and 2.67±0.08, respectively (not statistically different). There were minimal

differences between the trends of the separated spongiosa and ventricularis layers compared to the combined spongiosa and ventricularis. At a TVP level of 90 mmHg, mimicking the pressure that the PV experiences in the Ross procedure, the PV fibrosa reached a NAR of 9.67±0.61 that was significantly greater than the AV fibrosa NAR of 5.95±0.27. This difference in VIC deformation in the fibrosa layer is also visually confirmed (Figure 4). Hence, the AV and PV have complex nonlinear layer-specific VIC NAR as a function of pressure.

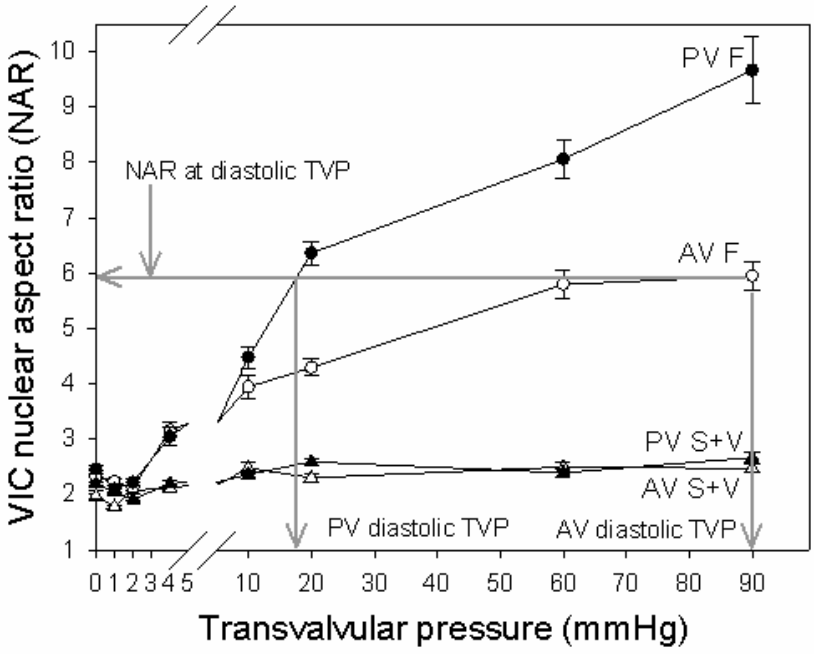

Figure 7: NAR of the porcine AV and PV as a function of TVP and layer. F represents fibrosa, and S+V represents combined spongiosa and ventricularis layer. An increase in NAR represents an increase in the VIC nucleus deformation. The vertical dashed lines denote approximate diastolic TVP of the AV and PV, while the horizontal dashed line represents the similar NAR at these respective TVP.

VIC mechanical coupling to collagen fibers in the fibrosa layer for both the AV and PV was further examined by comparing VIC deformations to collagen fiber straightening (Figure 8). As the TVP increased, the observable straight collagen fiber area increased. The increase in observable straight collagen fiber area was more rapid for the AV compared to the PV, and the

range of observable straight collagen fiber area was larger for the AV compared to the PV (Figure 8a). The NAR of the VICS in the fibrosa layer of the AV and PV also correlated with observable straight collagen fiber area as a function of TVP (Figure 8b). From 0% to 70% observable straight collagen fiber area there was relatively little change in VIC NAR. Above 70% observable straight collagen fiber area, corresponding to approximately 4 mmHg, there was a rapid increase in NAR for the PV compared to the AV. Further, at pressures above 4 mmHg the PV has a higher NAR and a lower observable straight collagen fiber area compared to the AV. At 90 mmHg both the AV and PV have approximately 93% observable straight collagen fiber area, but the PV reached a NAR of 9.67 and the AV reached a NAR of 5.95. This valve-specific correlation between VIC deformation and observable collagen fiber straightening indicated that VIC deformation was specific to the unique mechanical interactions within each valve's collagen fiber network.

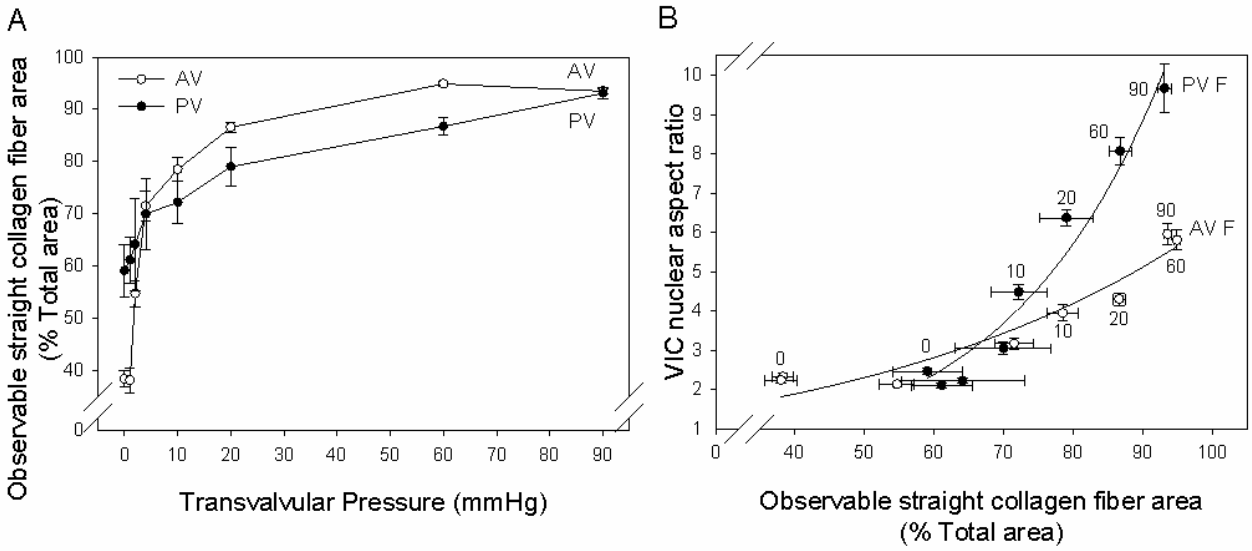

Figure 8: (A) Observable straight collagen fiber area from percent total area as a function of TVP. (B) NAR of the AV and PV fibrosa (F) was assessed as a function of both observable straight collagen fiber area from percent total area and TVP.

NAR of both valves were closer in value at equivalent stresses (Figure 9) compared to equivalent TVP (Figure 7) regardless of which stress metric was utilized, but were still surprisingly distinct for each valve. Specifically, the AV was under three to six times higher stress than the PV at their respective diastolic TVP assuming that either the fibrosa (Figure 9b) or the entire thickness (Figure 9a) bore the load. Thus, the VIC NAR was also a unique function of the local tissue stress within each valve.

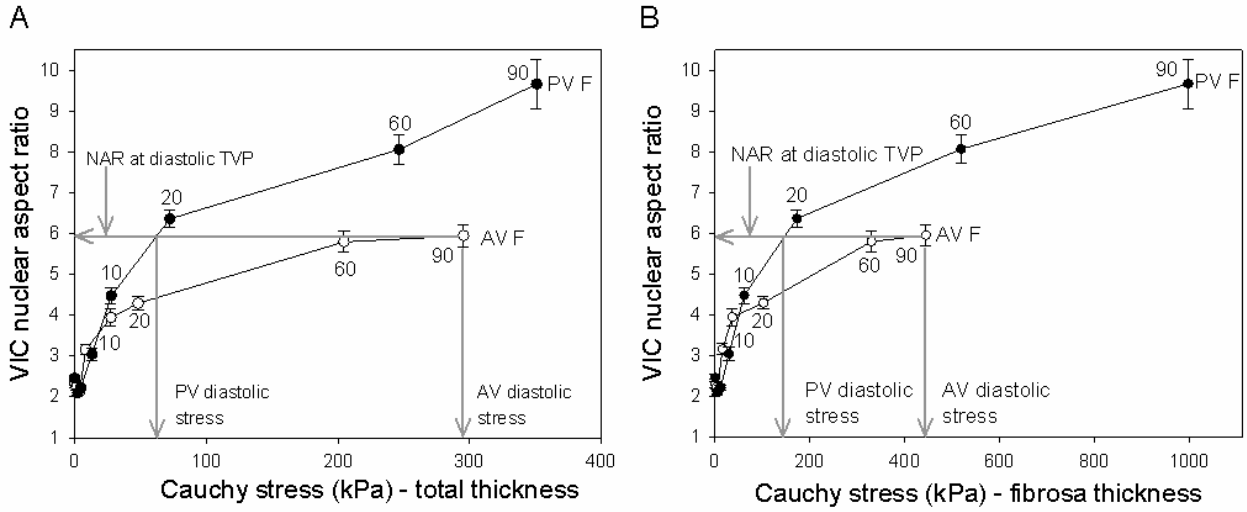

Figure 9: NAR of the AV and PV fibrosa (F) layer as a function of Cauchy stress. TVP was converted to stress through Laplace's law to account for difference in the deformed thickness. (A) It was assumed that the total thickness bears the load. (B) It was assumed that the thickness of only the fibrosa layer bore the load.

2.1.4 Discussion

2.1.4.1 ECM Gene Expression and the Organization of the AV and PV

This sub-aim demonstrated clear structural and functional differences, from the macro to the micro scale, between the semilunar valves. At the macro scale, the ECM stratification is valve specific, with the AV having a greater total and fibrosa layer (both absolute and proportional) thickness compared to the PV (Figure 1) (122). The fibrosa layer is predominantly composed of dense, type I fibrillar collagen that provides the large structural resilience required by the valve to resist the TVP. Thus, the finding that the AV has a thicker fibrosa layer (both in terms of absolute measurement and relative to the total thickness) is not surprising as its diastolic TVP that is six times greater than the PV. Moreover, we estimated larger tissue stresses at diastole in the AV (either total or by the fibrosa layer only, Figure 9). While based on a simple Laplace law approximation, this finding suggests that the thicker AV fibrosa does not fully compensate for the increased AV TVP; the AV fibrosa tissue is actually under effectively higher stresses compared to the PV at their respective diastolic pressures.

These findings are consistent with the observed higher baseline collagen gene expression in the AV compared to the PV (Figure 3), as well as with in-vitro study on isolated VIC culture from all four heart valves (146) where the VICs from valves under the highest TVP (mitral and aortic valves) demonstrated the highest biosynthetic levels. Further, in a recent study that examined collagen hydrothermal stability of heart valve tissues, it was found that collagen in heart valves subjected to higher TVP had lower molecular stability and cross-linking (147). The molecular stability of the collagen in the AV also decreased compared to that of the PV from transition from fetal to neonatal when the TVP in the AV increases due to closure of the foramen

ovale and ductus arteriosus (148). Aldous et al. speculated from these findings that a relationship exists between the turnover rate of collagen and mechanical loading whereby there is a faster rate of damage accumulation and collagen turnover in the valves under higher TVP as a mechanism of resistance to biomechanical fatigue loading. While intriguing, these findings are at present correlative and further studies needed to establish specific mechanisms, such as normalization for any differences in total collagen protein levels and to clarify how mRNA changes correspond to specific changes in protein levels in valvular tissues.

2.1.4.2 VIC ECM Layer Specific Deformation Response

Cellular deformation has been shown to occur as a function of organ level load for both native tissues and engineered tissue scaffolds (133, 141, 149). Critical to understanding the mechanobiological response of VICs is how the collagen fiber network locally deforms VICs with application of organ level loads. Note further that VIC-collagen micromechanical interactions were investigated under increasing TVP to simulate diastolic loading because it is during this phase the leaflets undergo the highest strains. In contrast, during opening/closing the leaflets are submitted primarily to flexure, wherein the leaflets undergo large deflections but small strains (approximately +/- 7% strain (150)).

In the present study, it was observed that VICs in the collagen-rich fibrosa layer significantly deform at higher pressures compared to the VICs in the spongiosa-ventricular layer that deform minimally (Figure 4, Figure 5, and Figure 7). Visual inspection of 3D image stacks (Figure 5) and quantification of VIC orientation and deformation (Figure 6, Figure 7, and Table 3) suggests that VICs in the spongiosa-ventricularis layer deform minimally because of a lack of large organized collagen fibers. Hence, the VIC-ECM coupling in the fibrosa and spongiosa-ventricularis layers is completely different and may have implications on VIC function in each

layer. The present study, taken together with our previous findings (122, 123), clearly indicates that the collagen fiber network organization of each semilunar valve is distinct.

2.1.4.3 General VIC-Collagen Micromechanical Interactions

The findings of this sub-aim indicate that VIC deformation is not a linear relationship with pressure (Figure 7) or tissue level deformations (Figure 2), but is instead dependent on the local rotation and straightening of collagen fibers (Figure 4, Figure 5, Figure 8b). Thus, these findings suggest that VIC deformation within the fibrosa layer is driven by changes in the local (as opposed to larger tissue level) collagen fiber structure as a function of TVP (Figure 8). VICs were found to preferentially align along the circumferential direction, which is the same as the preferred direction of collagen fibers. At a cell-ECM level, VICs are interconnected to the collagen fibers by integrins. It has been shown that blocking of the $\alpha_2\beta_1$ integrin or preventing actin polymerization resulted in a decrease in VIC orientation in the circumferential direction (151). Although demonstrating that integrins are a critical component of VIC-collagen interaction under small loads, under physiological loads it was found that VICs in the fibrosa deform due to mechanical compaction of surrounding collagen fibers (Figure 8, Table 3). Thus, specific organ level deformations do not directly translate to cellular level deformation but are highly modulated by the local collagen fiber structure.

2.1.4.4 Valve Specific Differences in VIC-Collagen Micromechanical Interactions

The substantial differences in the highly nonlinear fibrosa AV NAR compared to the PV as a function of stress confirms that the VIC-collagen micromechanical interactions are fundamentally different between the two valves (Figure 9). At 90 mmHg the PV had approximately a two times greater NAR than the AV. Thus, in pulmonary hypertension or the

Ross procedure, where the PV is under an increased pressure, the PV VICs undergoes a greater deformation than the AV VICs. This increase in cellular deformation may have implications to the PV VIC biosynthetic state, and subsequent leaflet remodeling. The most surprising finding is that AV VIC and PV VIC in the fibrosa have similar NARs at their respective diastolic TVP (Figure 6c, Table 3). Thus the valve collagen fiber network may be organized to induce a nearly constant NAR at peak diastolic TVP. This finding may indicate that the semilunar valves adjust the fiber network organization in response to TVP and this may be an important feature in maintaining semilunar valve homeostasis. Moreover, from these findings it is speculated that this is a common feature to all heart valves.

2.1.4.5 Summary and Implications

Collectively, these results indicate an interrelationship between ECM organization, VIC gene expression, and deformation with TVP that is highly valve specific. At the tissue level, the AV has a thicker fibrosa layer that is also subjected to greater stresses than the PV. At the gene level, this is consistent with higher levels of *Hsp47*, C*ol1a1,* and *Col3a1* mRNA expression in the AV than the PV. At the cell level, VICs undergo substantially larger deformations in the fibrosa layer compared to the spongiosa and ventricularis layers. VIC deformation in the fibrosa layer also appears to be due to mechanical compaction and elongation between local collagen fibers, while the spongiosa and ventricularis layer do not contain large organized collagen fibers and hence may not be able to induce large cellular deformations. Most interestingly, at their respective diastolic TVP for each valve VICs have a similar magnitude of deformation, even though there is a 6-fold difference in pressure and the difference in stress is estimated to be between 3 and 6 fold. Further, at 90 mmHg the PV VIC undergoes a much larger deformation than the AV VIC, which can be reached in pulmonary hypertension, or an autograft repair. Hence, different stress

levels may lead to modification of ECM gene expression and architecture, as seen with age, disease, or repair (121, 128, 134, 142, 148). Such anatomically site-specific complexity of the native heart valves through complex micro-interactions between the cell and fiber network indicate the potential benefits of using site-specific ECM scaffolds for a tissue engineered heart repair.

2.2 MICROMECHANICS OF THE MITRAL VALVE LEAFLET FIBROUS AND CELLULLAR STRUCTURES UNDER PHYSIOLOGICAL LOADING

2.2.1 Introduction

The investigation of the aortic and pulmonary valves indicated site-specific anatomic differences in cellular gene expression, tissue morphology, tissue mechanics, and cell-fiber network coupling. In order to acquire a better understanding of this cell-fiber network coupling the mitral valve was investigated due to its highly complex multi-layered structure, whose ECM constituent content and organization underlie its gross mechanical response under the highest transvalvular pressure of all the heart valves (121, 130, 152, 153). Such understanding of the VIC-ECM fiber network coupling will help to identify if the integrity of different ECM constituents and the fiber network are necessary in an ECM scaffold.

The MV leaflets are composed of the following four layers over most their volume: the atrialis, spongiosa, fibrosa, and ventricularis. The atrialis is composed of both type I and III collagen and elastin, and it is oriented towards the left atrium; the spongiosa is mainly composed of gycosaminoglycans; the fibrosa is the thickest layer and is composed mainly of

circumferentially oriented type I collagen; and the ventricularis is mainly composed of elastin and is oriented towards the left ventricle (154, 155). The circumferentially oriented collagen fibers of the fibrosa layer contribute to a stiffer mechanical response along the circumferential axis compared to the more compliant radial axis (156, 157). The large anisotropic strains found in-vitro through biaxial testing correspond to recent in-vivo measurements during systole (158). Although the valve structure has been qualitatively described in the literature, there is scant quantitative experimental data on how the MV fiber network reorganizes as a function of load, which is critical for implementation of a structural approach.

As tissue stress is closely related to cellular and tissue homeostasis (159-164) it also becomes critical to gain a better understanding of the underlying valvular interstitial cell (VIC) population, which maintain the ECM structure through protein synthesis and enzymatic degradation (129, 165-167). VICs have been demonstrated to be phenotypically plastic from human explants, quiescent under homeostatic conditions, and active in periods of growth and disease (130). It has been found that VICs undergo large scale deformations with tissue level stress (133), and VICs have recently been found to be closely coupled to collagen fibers via $\alpha_2\beta_1$ integrins (151). Hence, organ level loads are being transferred to large scale cellular deformations through the complex fiber network.

The above cited cellular deformations may be implicated in tissue driven mechanotransduction, i.e., translation of organ level mechanical stimuli into cellular responses. Indeed, the left heart side valve VICs (AV, MV) whose valve is under higher transvalvular pressure compared to the right side (PV, TV) are actually both stiffer, and they have a higher collagen biosynthesis (Hsp47) and a more active phenotype (SMA) (146). This finding implicates that VIC phenotypic response may shift due to changes in local stress, in cases such as

hypertension, mitral valve repair, or even calcification. In the case of mitral valve calcification the immediate substrate stiffness surrounding the VIC will be modified, and VIC phenotype is dependent on both substrate stiffness and age (168).

The objective of this sub-aim was to quantitatively characterize the MV microstructure as a function of physiological loads, including localized 3D VIC deformations, and relate it to the fiber network. Physiologic biaxial loads were applied to the anterior mitral valve leaflet under a real time TPM system. In the following experiments, the collagen signal was acquired through SHG, the elastin signal was acquired from autoflourescence, and VIC deformations were acquired through a nuclear stain under controlled physiological loads, and quantified.

2.2.2 Methods

2.2.2.1 Tissue Preparation

Hearts were acquired from 40 kg sheep at a local abattoir (MRG Food LLC). A 1 cm x 1 cm sample was taken from the anterior leaflet just below the annulus to above the first chordae tendineae attachment site (Figure 10a). The samples were split between two separate experiments: real-time deformations and imaging, and fixation and imaging. Four fiducial markers were placed in the center of the square and strains were measured optically by tracking this four marker array with Sony XCD-SX910 camera equipped with a Computar 55 mm telecentric lens interfaced with Labview Measurements and Automations. Samples were loaded into a miniature biaxial testing system: Two loops of 000 nylon suture of equal length were attached to each side of the specimens with four stainless steel hooks, which then connected to a dead weight on each side through a pulley system. Biaxial testing was conducted with the circumferential and radial specimen axes aligned with the device axes and submerged in a bath

of PBS at room temperature. Biaxial testing replicated the high levels of planar deformation experienced by the mitral valve leaflets in the belly region during coaptation (158, 169).

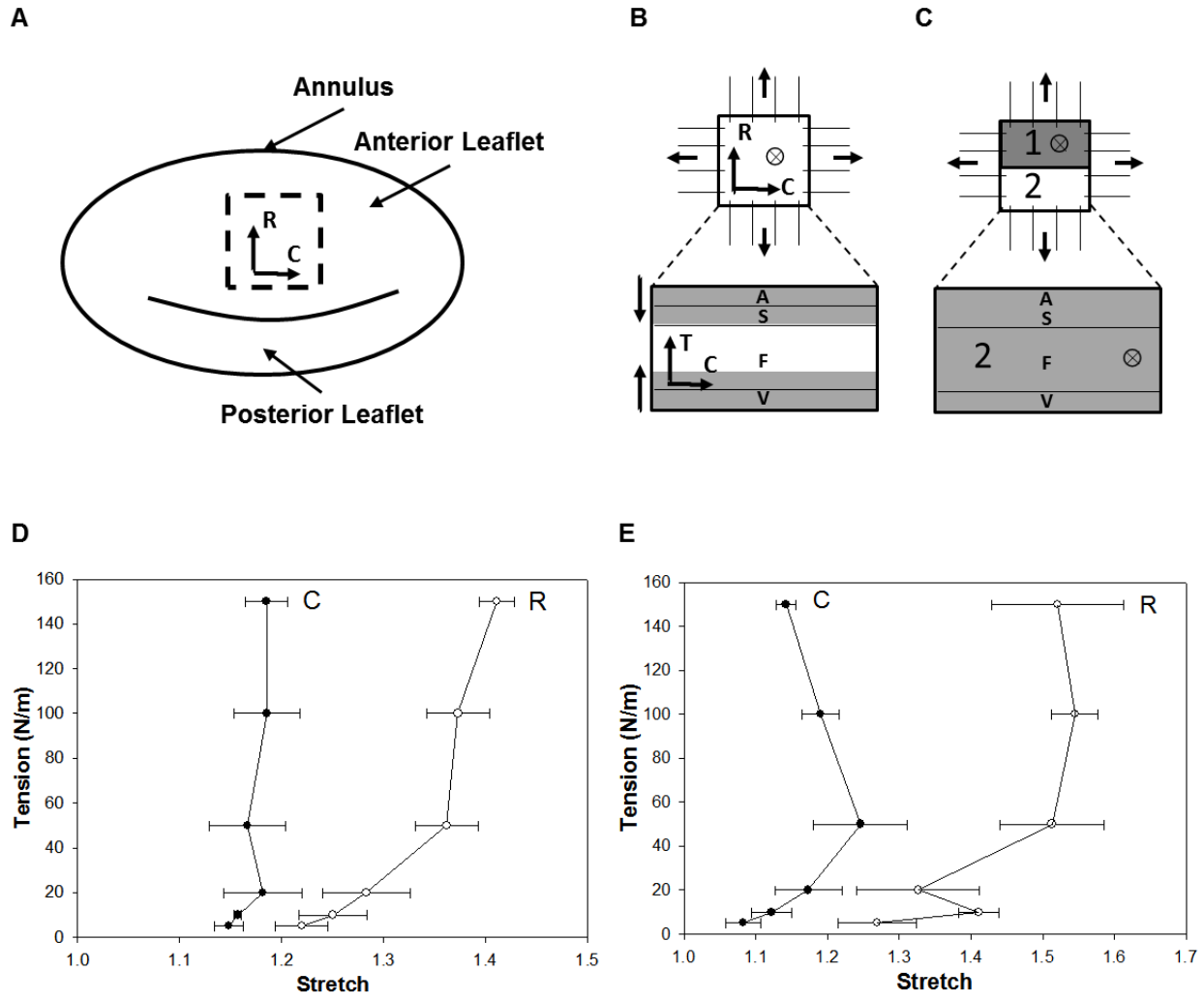

Figure 10: Experimental setup. (A) Diagram of the ovine mitral valve (MV), where C and R represent circumferential and radial direction, respectively. (B) In the first experiment, samples were imaged under real-time deformations enface to 100 µm deep (grey) on both surfaces encompassing the atrialis (A), spongiosa (S), part of the fibrosa (F), and the ventricularis (V). (C) In the second experiment, samples were loaded to a tension level and fixed for two hours in 2% PFA. The respective strain profile for each sample was measured for both the (D) the first experiment and (E) the second experiment demonstrating a transversely isotropic response.

2.2.2.2 Experiment 1 – Real Time Deformations

The first experiment objective was to quantitatively characterize the collagen and elastin fiber network as a function of controlled physiological loads. TPM is able to visualize collagen and elastin without probes that may modify the architecture, can encompass 3D volumes, and has deeper penetration depths than conventional laser scanning microscopy (LSCM). TPM has been used to qualitatively assess collagen and elastin fiber in the native semilunar valves, cryopreserved valves, and TEHV (170). However, these analyses were not quantitative. TPM has been quantitatively analyzed for both articular cartilage (171) and pericellular ECM (172).

The miniature biaxial testing system was mounted underneath an Olympus FV1000 TPM system operated with Olympus fluoview software. The system was equipped with a Chameleon ultra diode-pumped laser, equipped with a 25x XL Plan N objective with a N.A. of 1.05 and a field of view of 500 μm. The excitation wavelength was chosen at 800 nm at a 7% laser intensity transmissivity. The emission wavelengths were received by two filters: The first channel was set to 400±100nm for SHG signal of collagen, and the second channel was set at 525±50 nm for elastin autofluorescence. The sampling speed was set to 2 μs/pixel with a 2 line kalman filter, and the scanning had an incremental z-step of 2 μm.

An equibiaxial tension path was chosen wherein the ratio of axial tension was maintained. The maximum tension level was set to 150 N/m, with a total of seven tension points chosen for the loading path with the majority focused on the initial nonlinear loading phase. A peak tension of 150 N/m was used because it corresponds to in vivo transvalvular pressure when the mitral valves are coapted during systole. The sample was first imaged enface to a maximum penetration depth of 100 μm from the atrialis surface at all seven tension levels, and then the process was repeated from the ventricularis surface. Enface imaging from the atrialis and ventricularis surface encompassed the spongiosa and fibrosa layer, respectively (Figure 10b). Hence, all the layers were encompassed with this technique.

Using Matlab, image stacks were compiled into a maximum intensity z-projection (Figure 11a-b). The superimposed image stack was color channel separated to separate the collagen and elastin content. To quantify the fiber alignment from the z-projection a custom image analysis software was applied separately to the collagen and the elastin content. The image analysis software was written in Matlab by Courtney (173) using an algorithm developed by Chaudhuri (174), and modified by Karlon (175). This algorithm applies a variation of a Sobel operator to obtain the pixel intensity gradient to determine the preferred fiber direction for each sub-region (Figure 11c). The fiber direction from each sub-region was then placed into a histogram to determine the preferred fiber direction of the network. In addition, the fiber orientation index was found using the average over all fiber segments of $\cos^2(\theta)$ (COS OI), where θ represents the angle between a fiber segment and the direction of supposed alignment (176, 177). Statistical analysis compared the preferred fiber direction of the atrialis to the combined fibrosa and ventricularis using an independent-samples *t*-test at $p<0.05$ (PASW Statistics, V. 18). Values are reported as mean ± standard error.

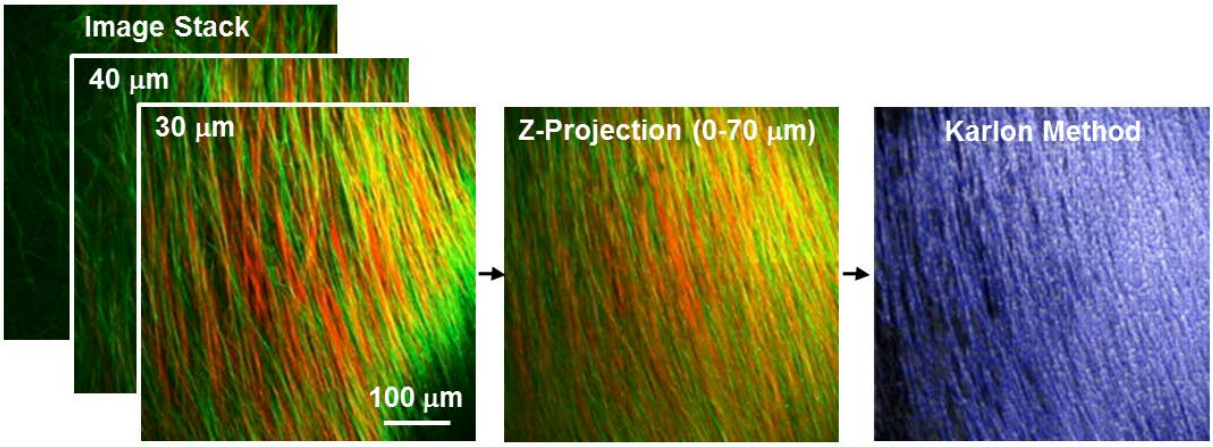

Figure 11: Fiber network analysis. (A) Image stack obtained from TPM visualizing collagen (red) and elastin (green) fibers from SHG and autofluoresence, respectively. (B) The image stack was imported into Matlab and compiled into a single image from a maximum intensity z-projection. (C) The image was then color separated and the Karlon method algorithm was applied to track both collagen and elastin fiber.

2.2.2.3 Experiment 2 – Fixation and Imaging

The second experiment objective was to quantitatively characterize layer dependent VIC deformations under controlled physiological loads as a function of both collagen fiber straightening and alignment. Samples were loaded and fixed at one of the seven loads, with three samples fixed per load for a total of 21 samples. Samples were fixed for 2 hours in 2% paraformaldehyde at the desired tension level. Each sample was split into two sections (Figure 10C).

The first section was used for small angle light scattering (SALS) technique to represent the ECM fiber alignment over the entire area of the sample as a validation of the TPM technique, which focused on a considerably smaller region (178). The sample was glycerol dehydrated in graded solutions of glycerol and saline of 50%, 75%, 87%, and 100% for an hour each and then scanned with SALS. For each sample the resultant intensity distributions for all the spatial

locations was imported into Matlab. A smoothing function was applied to each intensity distribution, and then a dual Gaussian distribution was fit. From this fit the number of local maxima was determined as either one or two, and the resultant fiber direction of each peak was recorded and associated with its respective spatial location.

The second section was paraffin embedded and cryosectioned along the circumferential-transverse surface. One 7 μm section was taken for staining with Movats Pentachrome for thickness measurements. ECM composition and stratification were evaluated in circumferential-transverse histological sections of adult porcine MV leaflets with a 10x and 25x objective (Figure 13a). Movat's pentachrome staining was used to visualize fibrous collagen (yellow), proteoglycan and GAGs (blue), and elastic fibers (black). In the MV leaflet, the collagen-rich fibrosa, proteoglycan-rich spongiosa, and elastin-rich atrialis and ventricularis layers were evident.

Another 30 μm section was taken for nuclear staining and imaging on TPM: Slides were deparaffinized, permeabilized with Triton™ X-100 for 20 minutes, and stained with Sytox Green (Invitrogen) at a 1:250 concentration for 30 minutes. Slides were then gelvatol mounted and cover-slipped. Slides were then imaged under the TPM system at an excitation wavelength of 830 nm with an incremental step of 1 μm. The first channel was set to 400±100nm for SHG signal of collagen, and the second channel was set at 525±50 nm for cytox green nuclear signal. In the second channel the elastin autoflouresence intensity was minimal compared to the cytox green intensity.

Image stacks were imported into Imaris software for 3D nuclear deformation visualization and quantitative analysis (Figure 12). An automated surface was fitted to each nuclear point cloud, and erroneous detections were eliminated using an automated maximum

voxel threshold, and a minimum voxel threshold of 250. The eigenvectors associated with each surface, and the major and minor axes of an ellipsoid fit to each surface was imported into Matlab. The major and minor axes were converted into the nuclear aspect ratio, an indicator of cellular deformation, and the eigenvectors were converted into spherical coordinates to define theta and phi for the 3D orientation of the VIC. The user identified the four layers of the MV from a maximum intensity z-projection of the collagen network, and then the quantitative data for each nucleus was automatically associated with its respective layer. Statistical analysis of principal directions was determined with a one-way analysis of variance (ANOVA) with valve layers as the independent variable followed by a post-hoc Tukey's test at $p<0.05$ (PASW Statistics, V. 18). Values are reported as mean ± standard error.

Representative slices of the image stack were imported into ImageJ for further collagen structure analysis. Percent observable collagen crimp was found with the thresholding function for the fibrosa region (n=3 per tension level). Collagen fiber crimp period was also investigated. In the unloaded state, the collagen fibers were crimped with an identifiable period (Figure 14a). With application of load, the majority of the collagen fibers lost their crimp as they were mechanically engaged, although some residual crimp remained (Figure 14b). Collagen fiber crimp was quantified for the collagen fibers of the atrialis and fibrosa layer. Collagen crimp period was found by manually measuring ten different crimp periods per sample (n=3 per tension level). The crimp period for the fibrosa was determined from transverse sections as it encompassed the entire fibrosa layer, and for the atrialis layer crimp period was measured from enface real time imaging.

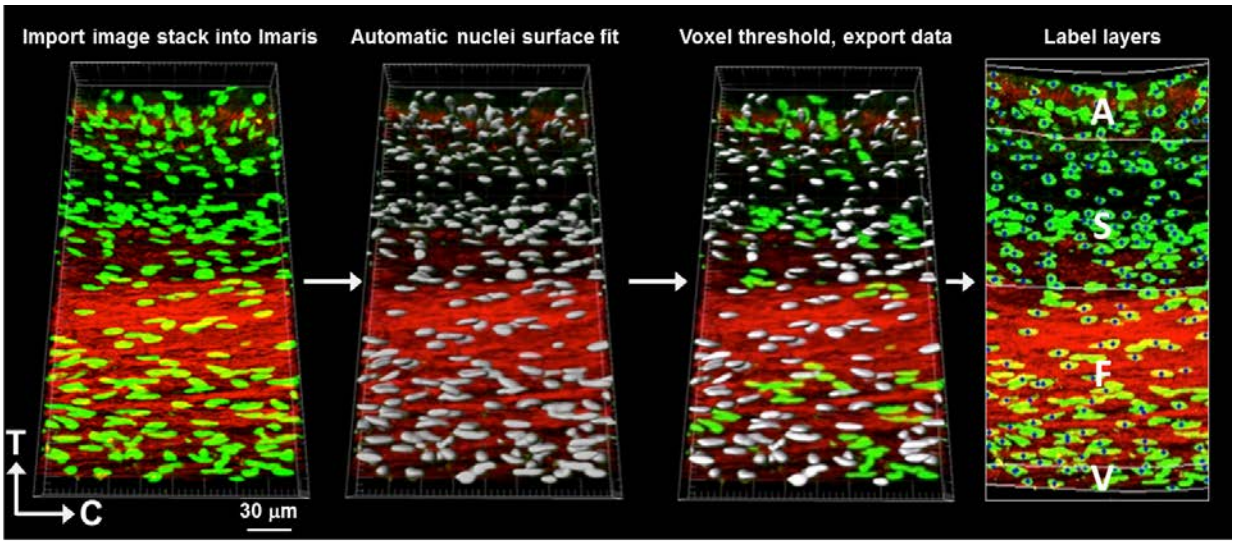

Figure 12: Cell deformation analysis. Image stack obtained from TPM were imported into Imaris software to visualize the Cytox Green stained cell nuclei in 3-D. Using built in image analysis functions in Imaris, 3-D surfaces were fit to all nuclei in the stack. Next, voxels were thresholded out by size to allow for more accurate nuclei surface fitting. Quantitative data was gathered including NAR and orientation angle. Finally, the data for each nucleus were associated with their respective MV layer with a custom Matlab algorithm.

2.2.3 Results

2.2.3.1 Mechanical Response

Consistent with previously published results, the biaxial response of the MV was nonlinear, and transversely isotropic (158, 169). The circumferential and radial directions reached strains of 20%, and 40%, respectively (Figure 10D). These strains from planar biaxial testing closely matched previously reported in-vitro analysis of the surface strains in the anterior leaflet of the functioning mitral valve apparatus (Refer to reference (169) Figure 5a). The MV followed a transition in the radial direction from a low modulus region to a high modulus region, while in the circumferential direction the valve had an immediate high modulus with minimal stretch. The

strain levels reached was similar to previously reported in-vivo analysis suggesting that biaxial equibiaxial tension protocol accurately approximated the strain field present during valve closure. More variation in the strain field for experiment 2 (Figure 10E) was seen compared to experiment 1 (Figure 10D) because comparisons were made between different animals with different thicknesses at each tension level for experiment 2, but the overall trend was found to be the same.

2.2.3.2 Fiber Network Analysis

The elastin-rich atrialis also contained collagen (Figure 13b-c), but the ventricularis layer was only a thin surface layer of elastin that transitioned to the collagen-rich fibrosa layer. The fibrosa layer was the thickest layer of the MV, while the ventricularis layer was the thinnest. From circumferential-transverse sections, the collagen (Figure 13b) and elastin (Figure 13a) in the atrialis was more punctate indicating an out-of-plane orientation in the radial direction, while the collagen in the fibrosa layer (Figure 13a-b) and elastin in the ventricularis (Figure 13a) was oriented perpendicular to the fibers in the atrialis layer along the circumferential direction. The perpendicular collagen and elastin orientation of the outer layers were further confirmed with enface TPM imaging of intact valves (Figure 13c). It was also found that the collagen and elastin in the atrialis layer were closely packed together (Figure 13c). This finding of a perpendicular fiber network was quantified with the application of a previously published automated algorithm (173) (Figure 13d).

Confirmation of these two fiber networks on a larger scale was performed with SALS (178). Whereas TPM is isolated to a 500 μm area, SALS can cover an entire leaflet and is a composite of the entire volume. A custom Matlab algorithm first detected if two fiber populations exist. Two fiber populations may not be detected if they were very close together, or

if the thickness of the valve was beyond 500 μm in any area. The algorithm indicated that if two distinct fiber populations arose – one was oriented along the circumferential direction, and the other was oriented along the radial direction (Figure 13e). This corresponded with the collagen and elastin oriented radially in the atrialis, and the collagen and elastin oriented circumferentially in the fibrosa and ventricularis, respectively.

The collagen fibers of the atrialis lost their crimp by about 10 N/m, while the collagen fibers of the fibrosa layer retained some residual crimp through 150 N/m (Figure 14c). This more immediate crimp removal for the collagen fibers in the atrialis layer corresponded with a smaller fiber diameter than those of the fibrosa layer, which were harder to define as distinct fibers compared to a sheet like structure (Figure 13c). Although residual crimp existed through 150 N/m for the fibrosa layer, the majority of observable crimped collagen area was removed by 20 N/m (Figure 14d). The removal of crimp at 20 N/m corresponded to when the biaxial mechanical response in the circumferential direction reached maximum strain. However, the removal of collagen crimp in the radial direction at 10 N/m did not correspond to when the biaxial mechanical response in the radial direction reached maximum strain.

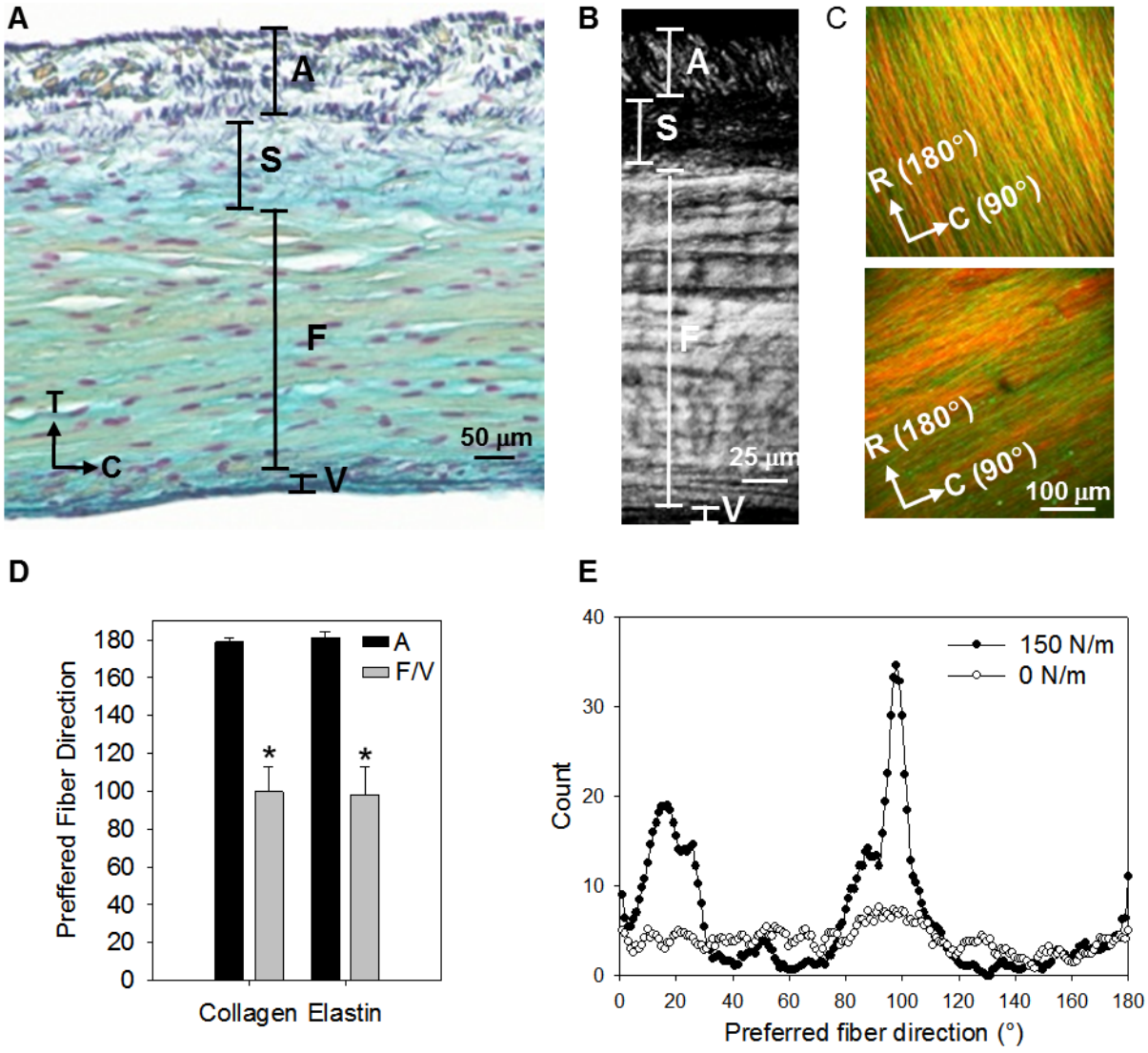

Figure 13: The atrialis layer had a distinct population of fibers that were oriented perpendicular to the fibrosa and ventricularis layer. This finding was confirmed with multiple methodologies. (A) Histological assessment of ovine anterior MV leaflet stratification with Movat's pentachrome stain, where C and T represent circumferential and transverse direction, respectively. A, S, F, and V represent the atrialis, spongiosa, fibrosa, and ventricularis, respectively. (B) SHG image from a circumferential-transverse section. (C) SHG and autoflourescence from TPM of intact tissue imaged enface with collagen (red) and elastin (green). (D) Collagen and elastin preferred fiber direction were calculated. (E) Normalized orientation index (NOI) was calculated for the collagen and elastin fiber network as a function of tension and layer from SALS. Error bars represent standard error, and * indicates significance from atrialis at $p<0.05$.

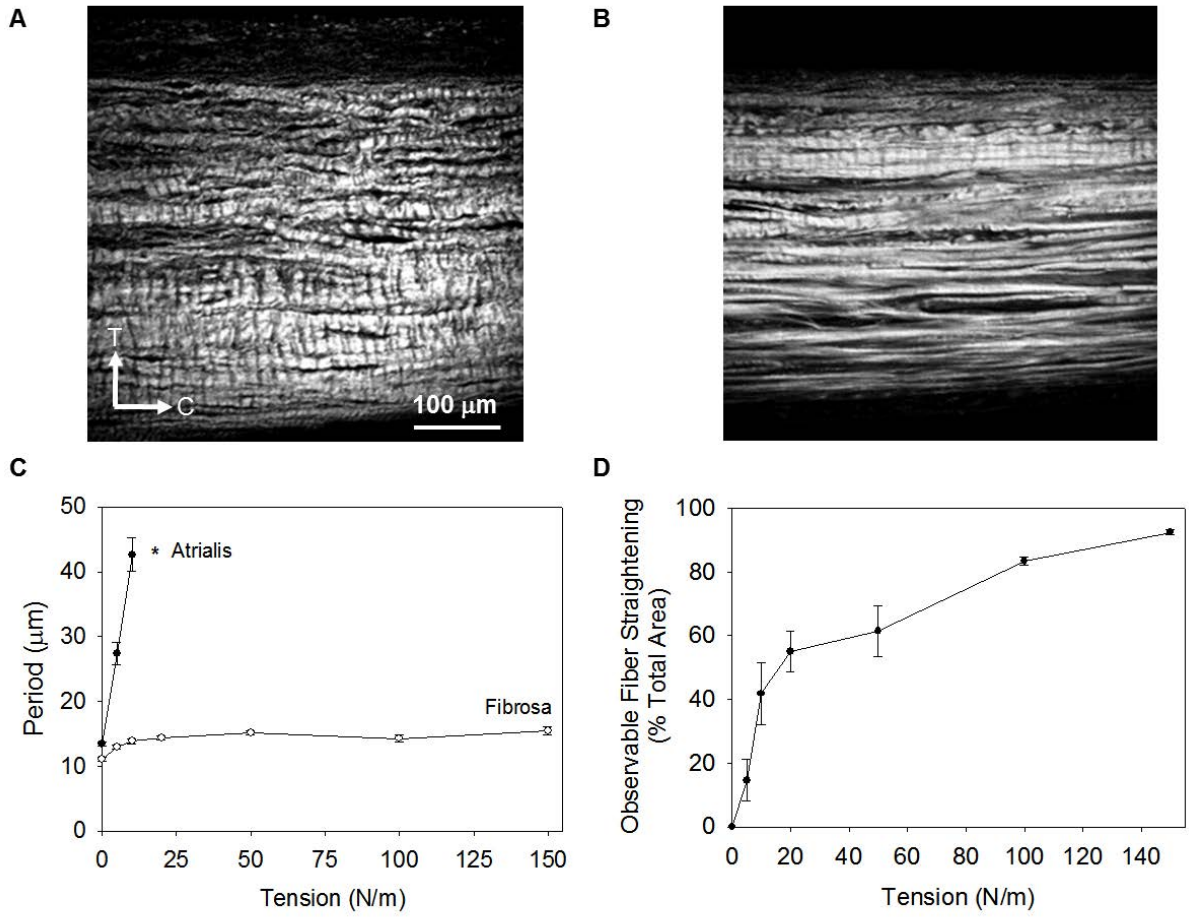

Figure 14: Collagen fibers were visualized with SHG from TPM for transverse cryosections at both (A) 0 and (B) 150 N/m loads. (C) The collagen crimp period as a function of layer, (D) Observable fiber straightening area from percent total area. Error bars represent standard error.

2.2.3.3 VIC Deformation Analysis

The VICs in the fibrosa layer and ventricularis layer deformed significantly more than those of the atrialis and spongiosa layer, reaching a NAR of 3.3 (Figure 15a). The deviations for each layer were large indicating that per each layer there was a large amount of variation in the amount of VIC deformation. This corresponds well to the residual crimp that existed in some areas of the fibrosa layer at maximum load: Some VICs were compacted by straightened

collagen fibers while other fibers still had residual crimp, and thus, were not deforming VICs to the same magnitude. The VICs also had an intrinsic ellipsoidal configuration at the free float state having a NAR of 2.5.

In addition to VIC deformation, the 3D orientation of each VIC was determined. By comparing the orientation of the VICs in each layer as a function of tension it was clear that a reorientation occurred as a function of layer. At the free float configuration the VICs were not well oriented with high standard errors. At maximum physiological tension, the VICs of the fibrosa and ventricularis oriented towards the circumferential direction while the VICs of the atrialis and spongiosa oriented towards the radial direction. Note that the VIC populations were oriented along the preferred fiber direction of their respective layers. Although the spongiosa VICs were orienting towards the radial direction, they showed a larger standard error compared to the VICs of the atrialis layer that had an aligned fiber network (Figure 15d). With tension, there was also a reorientation of the VIC populations in the circumferential-radial plane, or in-plane deformation, except for the atrialis layer (Figure 15e). This corresponded to the direction of collagen sheet orientation for the atrialis and fibrosa layer.

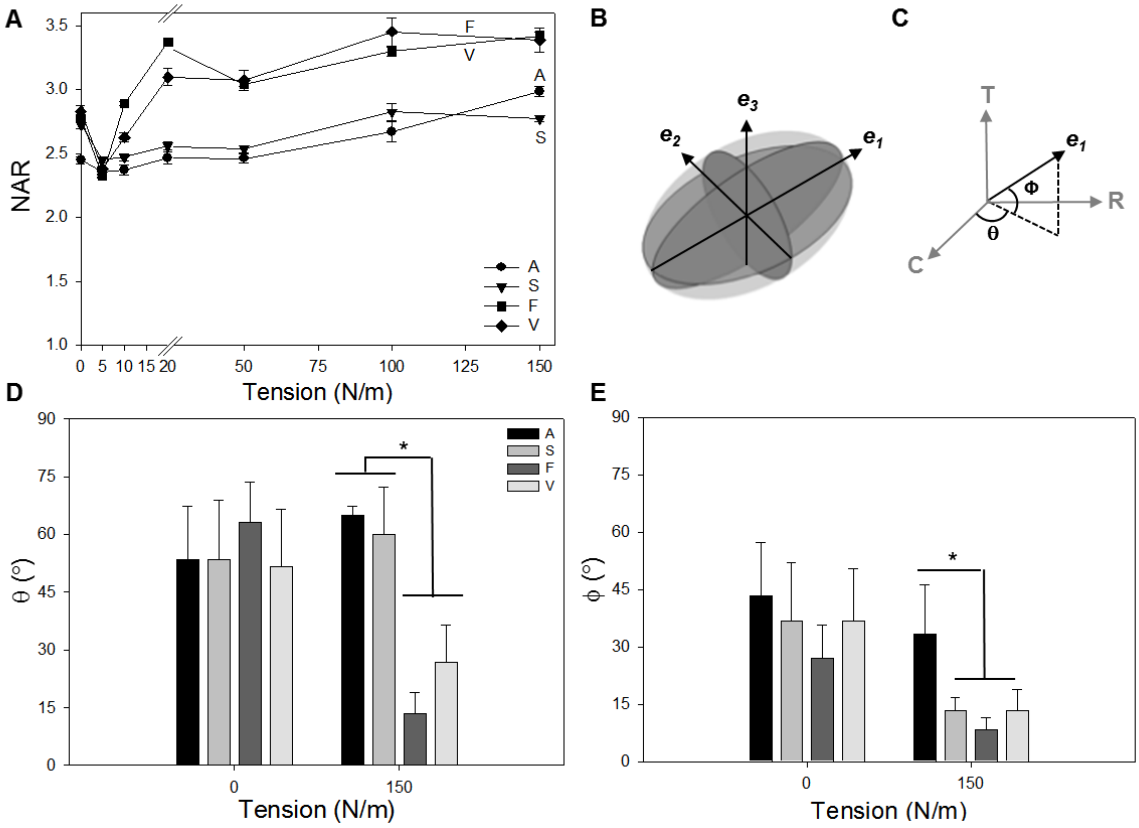

Figure 15: (A) MV nuclear aspect ratio (NAR) with respect to tension for each of the valves layers. A, F, S, V represent the atrialis, fibrosa, spongiosa, and ventricularis, respectively. (B) 3D nuclear geometries were acquired and principal axes directions (e_1, e_2, e_3) were found. (C) The major principal axis (e_1) was defined in spherical coordinates from angles θ and Φ. (D) The orientation angle of VIC nuclei off of the circumferential axis (θ) was compared as a function of layer and tension. (E) The in-plane orientation angle of VIC nuclei (Φ) was compared as a function of valve layer and tension. Error bars represent standard error, and * indicates significance at $p<0.05$.

2.2.4 Discussion

For the first time, the MV collagen and elastin fiber kinematics in addition to VIC deformation was quantified under controlled biaxial loading which replicated physiologic strain levels (157,

169). The study of MV layer-dependent fiber architecture and kinematics is critical to understanding the complexity of the native heart ECM. It is clear that the MV cell-fiber kinematics are complex as seen with mitral valve surgical repair whereby remodeling is initiated due to changes in leaflet stress distribution and resultant closure mechanics. This sub-aim provides an in-depth quantitative assessment of VIC deformation and associated ECM fiber network micromechanics.

2.2.4.1 Two Opposing Fiber Networks

This sub-aim found subtle layer differences in collagen and elastin fiber planar organization. Surprisingly, two opposing collagen and elastin networks exist on the opposite sides of the mitral valve leaflet. This structure is not seen in the AV. The AV collagen is circumferentially oriented and mainly exists in the fibrosa layer, and the elastin is oriented radially and existed in the ventricularis layer. Why does the MV have two separate opposing networks compared to the semilunar valve architecture? The MV is under the highest TVP gradient and may need a secondary fiber network in the atrialis to provide further support during the loading cycle. However, this could be simply achieved with an increase in thickness or a single randomly oriented network. Instead, there exist two fiber networks on opposite sides of the valve that are perpendicular to each other. The existence of opposing fiber networks in the mitral valve is similar to that of the alternating collagen fiber bundles in the heart (94).

For both the AV and MV the bulk collagen fibers are in the fibrosa oriented in the circumferential direction resulting in minimal strain along this axis. However, there is a large radial deformation in the AV, and the secondary network of the MV in the atrialis is oriented along the radial direction. Hence, the radially oriented collagen in the MV atrialis layer may serve to decrease compliance along this axis with strains only reaching 40% compared to the AV

reaching 60%. Also, the radially oriented elastin in the atrialis may further aid in returning the valve to its initial configuration, as seen for the AV in the ventricularis (179, 180). The distribution of two separate networks may also allow for greater controllability over two axes of flexure to further optimize the gross 3-dimensional leaflet deformations during the closure mechanics of the valve.

Another question that arises is how did these two distinct networks form? The elastin is oriented radially along the blood ejecting surfaces for both the MV (atrialis surface) and AV (ventricularis surface), whereas the elastin is oriented circumferentially for the ventricularis surface of the MV. Thus, flow may be a potential mechanism in either the formation or the orientation of elastin. Specifically, endothelial cells are known to be sensitive to the directionality of flow in-vitro (181). Although VICs are not in contact with blood, evidence indicates that valvular endothelial cells regulate the phenotype of VICs (182). Hence, endothelial cells may play a critical role in the regulation of the directional formation of elastin.

2.2.4.2 Layer Dependent VIC-Collagen Micromechanical Coupling

The ECM is a dynamic environment with proteins being continuously degraded and replaced. Perturbations to this system have been shown to be caused with age and disease. In order to gain a better understanding of MV remodeling it is necessary to gain a better understanding of VIC mechanobiology, ie. how VICs' biosynthetic activity is impacted by organ level loads. There is a lack of understanding of how local forces are transduced to VICs from organ level loads. In this sub-aim, MVICs experienced layer specific deformations with load, as reported for the semilunar valves (133). VICs in the fibrosa layer underwent the largest deformation compared to those in the other layers. As previously concluded in the first section of Specific Aim 1 (183), deformation of VICs is largest in the fibrosa layer because they are compacted by straightened

collagen fibers. We found that VICs in the atrialis orient more toward the radial direction in parallel to the collagen fibers in that layer, while VICs in the fibrosa orient towards the circumferential direction in parallel to the collagen fibers in that layer. Although collagen fibers exist in the atrialis layer they are thinner, more fibrous, and have more spacing compared to the collagen fibers in the fibrosa layer that display a sheet organization. This additional spacing between the collagen fibers in the atrialis results in less compaction corresponding to a lower deformation level than seen in fibrosa layer VICs. This finding confirms that VIC deformation is closely coupled to collagen fiber orientation, being compacted and extending between the spaces of the collagen fibers.

2.2.4.3 Summary and Implications

These subtle layer differences in ECM planar organization and the intricate interrelationship between ECM planar organization and VIC deformation indicate the promising potential of anatomically site-specific ECM scaffolds. Compared to the inherent limitations of synthetic platforms to engineer a three dimensional biomaterial that mimic the complexities at the microstructural level for heart repair or replacement, ECM scaffolds are derived from tissues and may retain the complexity of the native ECM fiber network. However, the manufacturing process to produce an ECM scaffold from native tissue requires the usage of many chemicals including detergents. Detergents such as SDS are known to result in denaturation of collagen fibers but are used in the majority of decellularization protocols, especially creating cardiac ECM scaffolds. The questions arise both whether this decellularization indeed damages the complex composition and structure of the native heart ECM, and whether any damage to the biochemical and/or structural properties of the ECM impacts this complex cell-ECM interaction.

3.0 COMPOSITION, STRUCTURE AND MECHANICS OF DETERGENT TREATED TISSUE[2]

3.1 INTRODUCTION

Specific Aim 1 established that the native heart is extremely complex with site-specific cellular gene expression, fiber network organization, and cell-ECM coupling. Site-specific ECM scaffolds may retain this anatomically specific composition and three-dimensional fiber network organization. However, the manufacturing of ECM scaffolds is a complex process that requires balance between achieving successful decellularization to prevent an adverse immune response and minimizing damage to the composition, biologic activity, and mechanical integrity of the ECM (61).

[2]This work has been adapted from the following published manuscript:

Faulk DM, Carruthers CA, Warner HJ, Kramer CR, Reing JE, Zhang L, D'Amore A, Badylak SF. The effect of detergents on the basement membrane complex of a biologic scaffold material. Acta Biomaterialia. 2013; Doi: 10.1016/j.actbio.2013.09.006.

3.1.1 Criteria for Successful Decellularization and Relationship to Host Response

A stringent set of criteria for successful decellularization were developed based upon previous findings (100, 184). These criteria are defined as follows:

1. No visible nuclear material by histological examination with H&E and DAPI stain
2. DNA content of less than 50 ng/mg day weight
3. No remnant DNA with base pair length greater than 200

The focus upon DNA is justified because it directly correlates with adverse host reactions (105). For example, poor cytocompatibility was found upon reintroduction of cellular tissue, even autologous, in a rodent partial thickness abdominal wall defect. This poor cytocompatibility was characterized by the deposition of dense connective scar tissue and a predominantly M1 macrophage phenotype. In contrast, properly prepared acellular ECM scaffolds elicited a constructive remodeling response with the formation of site specific functional tissue and a predominantly M2 macrophage phenotype (104). Another study found that more aggressive decellularization of SIS was associated with a shift in macrophage phenotype from M1 to M2 in-vitro, with notable differences found in-vivo in a rodent model in the distribution of M1 versus M2 macrophages (105). Thus, if the aforementioned decellularization criteria are not reached such that residual cellular material is still present within the ECM, an adverse host response may result.

3.1.2 Adverse Effects of the Manufacturing Process

Successful decellularization is only one contributing factor toward preventing an adverse host response to an ECM scaffold. Both the chemicals and methods of terminal sterilization used in the manufacturing process are known to effect an ECM scaffold's composition, ultra-structure, and the subsequent host response. For example, while SIS in a rodent model elicited a predominantly M2 macrophage phenotype and constructive remodeling at 16 weeks, a cross-linked SIS had chronic inflammation. Chemical crosslinking has been correlated with delayed degradation (185), a chronic mononuclear cell accumulation around the device (43, 185), and scar tissue formation (43, 44, 185).

The method of terminal sterilization affects the structural and mechanical properties of an ECM scaffold. It was found that UBM sterilized with gamma (2.0 Mrads) and electron-beam (2.2 Mrads) radiation had a decrease in uniaxial and biaxial strength, maximum tangential stiffness, and energy dissipation while UBM treated with ETO (750 mg/hr for 16 hr) had the least detrimental effect (186). The method of sterilization also correlated with distinct differences in the host response (43).

While the described studies have mechanistically investigated the effect of remnant cellular content, cross-linking, and terminal sterilization on the ECM scaffold's composition, structure, and cytocompatibility there is a lack of understanding on how different detergents in the manufacturing process impact these parameters. Detergents are used in the manufacturing process to both solubilize cell membranes and dissociate DNA from proteins. Several methods for generating ECM scaffolds have been published, each of which describes a unique and

specific recipe of enzymes and detergents. Table 4 lists three protocols for whole organ decellularization of the heart and one protocol for decellularization of myocardium sheets.

Table 5 lists additional protocols that have been reported for other organs and tissues. As seen in Table 4's and Table 5's list of commonly used manufacturing protocols, there is clearly a large degree of variability in detergent type, incubation time, and concentration in the literature. Most of the manufacturing protocols contain multiple steps with more than one detergent. The detergents used range from non-ionic detergents such as Triton™ X-100 to ionic detergents such as SDS.

The majority of heart decellularization protocols contain a step that uses SDS for at least 12 hours (Table 4), and an SDS step is also prevalent for decellularization of other organs and tissues (Table 5). While ionic detergents such as SDS can be more effective for removal of cellular material than non-ionic and zwitterionic detergents (187), studies have shown that subjecting tissues to harsher detergents such as SDS can disrupt the ECM structure (188), eliminate growth factors (106), and denature essential proteins (114-116, 189). While there has been some comparison of multiple step protocols used to achieve decellularization (72, 103, 106-113) none have comprehensively isolated and compared individual detergents' effect on scaffold composition, structure, or mechanics. The hypothesis of this aim is that ionic detergents such as SDS will result in a loss of ECM constituents and a decrease in mechanical strength that is correlated at the micro-structural scale.

Table 4: Protocols for heart decellularization.

Whole Organ Decellularization			Tissue Decellularization
Porcine Heart (71, 190)	Porcine & Rat Heart (72, 113, 191)	Rat Heart (113)	Porcine Myocardium Sheets (60)
0.02% Trypsin (3 hr)	1% SDS (12 hr)	1% SDS (12 hr)	1% SDS (60-120 hrs)
3% Triton™ X-100 (2.5 hr)	1% Triton™ X-100 (0.5 hr)	20% glycerol (12 hr)	1% Triton™ X-100 (0.5 hr)
4% Sodium deoxycholate (3 hr)	1x PBS (124 hr)	1% Saponin (12 hr)	Type I water (12-24 hrs)
0.1% Peracetic acid (1.5 hr)		20% glycerol (12 hr)	
Type I water & 2x PBS rinses (0.5 hr)		200 UI/ml Dnase I (12 hr)	

Table 5: Protocols for liver, kidney, lungs, bladder, and cornea decellularization.

Whole Organ Decellularization				Tissue Decellularization	
Rat Liver (58)	Rat Liver (64)	Rat Kidney (192)	Rat Lungs (67)	Porcine Bladder (102)	Cornea (193)
0.02% Trypsin (2 hr)	0.1% SDS (72 hr)	3% Triton™ X-100	CHAPS (3 hrs)	Mechanical Separation	0.3% SDS (20 hr)
3% Triton™ X-100 (24 hr)		Dnase		PAA (2 hrs)	Dnase 1 (3 hr)
0.1% PAA (1 hr)		4% SDS			
Type I water 2x PBS rinses (0.5 hr)					

3.2 METHODS

3.2.1 Tissue Source

Two source tissues were chosen for their relevance in application to cardiac repair: Urinary bladder and heart. Urinary bladder was chosen as a source material because it has been used to

create a clinically relevant material for cardiac repair known as UBM (88, 89). Further, urinary bladder supports an epithelial cell layer upon a BMC, and is commonly decellularized as a sheet with detergent immersion and mechanical agitation. Porcine urinary bladders were obtained from animals at a local abattoir (Thoma's Meat Market, PA). Bladders were frozen (>16 hr at −80 °C) and thawed completely before use. The BMC and underlying lamina propria were mechanically isolated and harvested from the bladders as previously described (102, 186, 194). The term “detergent treated bladder” will refer to detergent treatment of the isolated BMC and underlying lamina propria of the urinary bladder.

Heart tissue was chosen because it is a site-specific ECM scaffold that has been used for cardiac repair (66, 87). Further, heart tissue supports an endothelial layer and is effectively decellularized through whole organ retrograde detergent perfusion (Figure 16). Porcine hearts were obtained under controlled conditions to minimize damage to the vasculature near the surface (Tissue Source, Indiana). Hearts were frozen (>16 hr at −80 °C) and thawed completely before use. For subsequent analysis after decellularization the right ventricle free wall was used because of its previous usage as a cardiac patch (87).

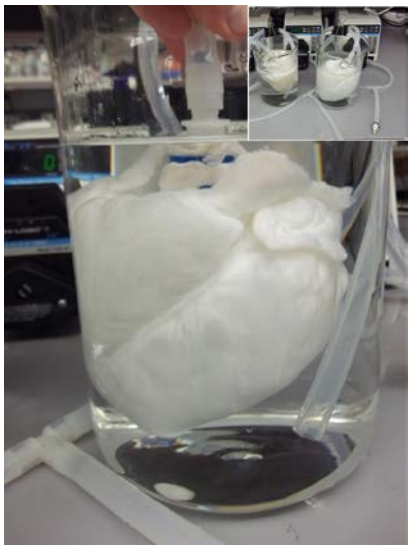

Figure 16: Whole organ heart decellularization by retrograde perfusion with a peristaltic pump.

3.2.2 Decellularization Protocol

Tissues were subjected to one of four commonly used detergents (From Table 4 and Table 5):

1. A non-ionic detergent called Triton™ X-100
2. A zwitterionic detergent called 3-[(3-cholamidopropyl)dimethylammonio]-1-propanesulfonate (CHAPS)
3. An ionic detergent called sodium deoxycholate
4. An ionic detergent called sodium dodecyl sulfate (SDS)

Thus, the detergent selection represents the three categories of detergents (non-ionic, zwitterionic, and ionic detergents), and also accounts for the different molecular sizes and structure of two ionic detergents (sodium deoxycholate, and SDS). The concentration for decellularization of bladder and heart was chosen to both replicate those used in the literature while maintaining similar molarities (Table 6). The majority of the detergents were above the critical micelle concentration (CMC) to effectively form micelles for removal of cellular components. CHAPS was the only detergent used at its CMC, and was only used for treatment of the bladder due to both cost constraints and its usage in the literature for only decellularization of a sheet such as the cornea.

The bladder was treated with these detergents through mechanical agitation at 3000 RPM (102, 186, 194), while the heart was treated with these detergents through retrograde perfusion (65, 71, 190). During the whole organ heart decellularization process the speed of the peristaltic pump was incrementally increased from 400 ml/min to 2.2 L/min following a previously reported protocol (190). The speed was incrementally increased to account for the decrease in heart resistance with decellularization in an attempt to estimate a pressure control system.

A protocol was formulated to subject both the bladder and the heart to these commonly used detergents under controlled conditions with all other variables constant (Table 7). Heart tissue was treated for 12 hours because this is the most commonly used duration for heart decellularization (Table 4). Porcine bladders were treated for double this period at 24 hours to mimic some of the longer decellularization protocols in the literature (Table 5). For both tissues a commonly used step of treatment with trypsin was included to detach cells from the tissue. Additionally, between each step a rinse of hypertonic and hypotonic solution was used to lyse cells. After the tissue was subjected to a detergent a prolonged rinse was completed to remove residual detergent. Because whole organs are more difficult to decellularize many reported protocols use multiple detergents. Therefore, an established multiple step protocol from the literature (71, 190) was also included to investigate serial detergent usage for heart decellularization. A control was included for both the bladder and heart tissue. For the bladder the control was defined as treatment with 0.02% trypsin, and 0.05% EDTA for 2 hours. For the heart the control was defined as the native tissue. The goal of detergent treatment was not necessarily to reach the criteria for successful decellularization, but to compare the effect of detergent treatments on the source tissue under similar controlled conditions. Detergent treated tissues were either fixed in 10% neutral buffered formalin, 2.5% gluteraldehyde, or frozen in liquid nitrogen for subsequent analysis.

Table 6: Concentration of selected detergent solutions

	Percent Solution (%)	Molarity (mM)	Critical Micelle Concentration (mM)	Molecular Weight (g/mol)
Triton™ X-100	3.0	48	0.5	625
CHAPS	0.5	8	8	615
Sodium deoxycholate	2.0 (heart) 4.0% (bladder)	49 72	4	415
SDS	1.0	35	9	288

Table 7: Decellularization protocols

Bladder Protocol	Heart Protocol	Heart Multiple Step Protocol (71, 190)
0.02% Trypsin, 0.05% EDTA at 37 °C (2 hrs)	0.02% Trypsin, 0.05% EDTA at 37 °C (2 hrs)	0.02% Trypsin, 0.05% EDTA at 37 °C (3 hr)
2x PBS, Type I water (0.25 hr, 2x)	2x PBS, Type I water (0.25 hr, 2x)	2x PBS, Type I water (0.25 hr, 2x)
Detergent (24 hrs)	Detergent (12 hrs)	3% Triton™ X-100 (2.5 hr)
1x PBS, type I water rinse (0.25 hr, 2x)	1x PBS, type I water rinse (0.25 hr, 2x)	2x PBS, Type I water (0.25 hr, 2x)
1x PBS rinse (24 hrs)	1x PBS rinse (24 hrs)	4% Sodium deoxycholate (3 hr)
		2x PBS, Type I water (0.25 hr, 2x)
		0.1% Peracetic acid (1.5 hr)
		1x PBS rinse and type I water rinses (0.25 hr, 2x)

3.2.3 Double Stranded DNA Quantification

ECM Scaffolds were digested in 0.6% Proteinase K solution for at least 24 hours at 50°C until no visible tissue remained. Phenol/Chloroform/Isoamyl alcohol was added and samples were centrifuged at 10,000xg for 10 min at 4°C. The top aqueous phase containing the DNA was

transferred into a new tube. Sodium acetate and ethanol was added to each sample and the solution was mixed and placed at -80°C overnight. While still frozen, the samples were centrifuged at 4°C for 10 min at 10,000xg. Supernatant was discarded and all residual alcohol was removed. Pellet was suspended in TE buffer. Double stranded DNA (dsDNA) was quantified using Quant-iT PicoGreen Reagent (Invitrogen Corp., Carlsbad, CA, USA) according to the manufacturer's instructions in duplicates. Samples were normalized to dry weight of the ECM scaffold. The dry weight is defined as the material after decellularization and lyophilization that was used in the initial proteinase k solution digestion.

3.2.4 Soluble Collagen and Sulfated GAG Quantification

10 mg ECM/ml (dry weight) were enzymatically digested in a solution of 1 mg/ml porcine pepsin (Sigma Aldrich, St. Louis, MO) in 0.01 N HCl under a constant stir rate for 72 h at room temperature. The pH neutralized pepsin digests were diluted and assayed for soluble, triple helical collagen content using the Sircol Collagen Assay (Biocolor Ltd., Carrickfergus, United Kingdom) per the manufacturer's instructions. The pH neutralized pepsin digest were also analyzed for total protein recovered using the BCA protein assay (Pierce). A pepsin buffer solution was used as the negative control and subtracted from the signal. Similarly, 50 mg/ml of powdered ECM in 100 mM Tris (pH 7.5) was digested with 0.1 mg/ml proteinase K (Sigma) at 50 ºC for 24 h with gentle agitation. The proteinase K digests were then assayed for sulfated GAG concentration using the Blyscan Sulfated Glycosaminoglycan Assay (Biocolor Ltd.) per the manufacturer's instructions. All results were normalized to dry weight tissue. Assays were performed in duplicate on three independent samples for each treatment group.

3.2.5 Growth Factor Assays

Three hundred (300) mg of detergent treated urinary bladder powder was suspended in 4.5 ml of urea-heparin extraction buffer. The extraction buffer consisted of 2 M urea and 5 mg/ml heparin in 50 mM Tris with protease inhibitors [1mM Phenylmethylsulfonyl Fluoride (PMSF), 5 mM Benzamidine, and 10 mM N-Ethylmaleimide (NEM)] at pH 7.4. The extraction mixture was rocked at 4^{o}C for 24 hours then centrifuged at 3,000 g for 30 minutes at 4^{o}C. Supernatants were collected, and 4.5 ml of freshly prepared urea-heparin extraction buffer was added to each pellet. Pellets with extraction buffer were again rocked at 4^{o}C for 24 hours, centrifuged at 3,000 g for 30 minutes at 4^{o}C, and supernatants were collected. Supernatants from first and second extractions were dialyzed against Barnstead filtered water (three changes, 80 to 100 volumes per change) in Slide-A-Lyzer Dialysis Cassettes, 3500 MWCO (Pierce, Rockford, IL). The concentration of total protein in each dialyzed extract was determined by the bicinchoninic acid (BCA) Protein Assay (Pierce, Rockford, IL) following the manufacturer's protocol, and extracts were frozen in aliquots until time of assay.

Concentrations of basic fibroblast growth factor (bFGF),and vascular endothelial growth factor (VEGF) in urea-heparin extracts of detergent treated urinary bladder samples were determined with the Quantikine Human FGF basic Immunoassay (R&D Systems, Minneapolis, MN), and the Quantikine Human VEGF Immunoassay (R&D Systems). Manufacturer's instructions were followed for both growth factor assays. Each assay for bFGF and VEGF was performed in duplicate, and each growth factor assay was performed two times. It should be noted that growth factor assays measured the concentration of each growth factor and did not measure growth factor activity.

3.2.6 Histologic Staining and Immunolabeling of the Detergent Treated Tissue

The BMC is one of the first ECM structures made by the developing embryo with its major constituent laminin-111, synthesized at the eight cell stage (195). This BMC is the first ECM structure with which embryonic stem cells interact and represents a key biosignal for separating endoderm from ectoderm; thus, it is logical that the BMC can represent an important structure in an ECM scaffold. ECM Scaffolds containing a BMC are used in a variety of pre-clinical and clinical applications (88, 118, 196-203), and some of these ECM scaffolds are seeded with cells before use (204-206). The UBM, originating from urinary bladder, is an example of an ECM scaffold that contains a BMC structure. Thus, the treated bladders were immunolabeled for ECM constituents that are known to be present in the BMC (200).

Fixed detergent treated bladders were embedded in paraffin and cut into 5µm sections. Sections were either stained with Hematoxylin and Eosin (H&E), Movat's Pentachrome, or used for immunolabeling. For immunolabeling, slides were manually deparaffinized, placed in Citrate Antigen Retrieval Buffer (10 mM, pH 6), and heated to 95°C for 20 min. Slides were then cooled to room temperature, rinsed in 1X PBS three times for 3 min, placed in humidity chamber to incubate for 1 hr with blocking solution (2% Goat Serum, 1% BSA 0.1% Triton™ X-100 0.1% Tween) at room temperature, then incubated overnight at 4°C with anti-collagen I antibody (Sigma-Aldrich, C2456, 1:1000) in blocking solution. Slides were then rinsed with 1X PBS as above, treated with 30% hydrogen peroxide in methanol solution for 30 min, and re-rinsed. Biotinylated secondary antibody Horse Anti-Mouse IgG (Vector Labs, 1:100) was then applied for 30 min. Slides were rinsed as above, ABC solution applied for 30 min in humidity chamber at 37°C, re-rinsed, and 3,3'-diaminobenzidine (DAB, Vector Labs) was applied under microscope.

To stain collagen IV (ab6586, Abcam, 1:500), laminin (L9393, Sigma-Aldrich, 1:100), and Collagen VII (C6805, Sigma-Aldrich, 1:10) staining was conducted using the same protocol as collagen I with an added 0.05% pepsin in 0.01 mM hydrochloric acid for 15 minutes in humidity chamber at 37°C following citrate acid buffer antigen retrieval. Collagen VII additionally used a blocking solution that contained a higher concentration of goat serum (4%) and BSA (2%), and a 1 hour hydrogen peroxide incubation time. After DAB staining, all slides were counterstained with hematoxylin, dehydrated and manually coverslipped using standard mounting medium. Images were taken at the luminal interface of the tissue.

3.2.7 Analysis of the ECM Fiber Network

Scanning electron micrographs (SEM) was used to examine the surface topology of bladders and hearts treated with each detergent. Samples were fixed in 2.5% glutaraldehyde in 1X PBS, cut into blocks of approximately $8mm^3$, and washed thoroughly in 1X PBS for three times at 15 minutes each. Samples were then fixed in 1% OsO_4 in 1X PBS for 15 minutes each, dehydrated in graded series of alcohol (30%-100%) baths for 15 minutes each. Samples were then critically point dried with Hexamethyldisiloxane mounted on studs, sputter coated, and stored in a desiccator until imaged. SEM images of the luminal surface were captured using a JEOL 6335F Field Emission SEM with backscatter detector.

A complete set of fiber network descriptors was collected from SEM images including: pore size distribution, node density (number of fibers intersections per μm^2), and fiber diameter. Porosity was described by the mean of the pore size (μm^2) histogram. Automated extraction of these fiber architectural features was achieved with an algorithm, which has been previously described in detail (207). Briefly, the SEM image is digitally processed by a cascade of steps

including equalization with a 3x3 median filter, local thresholding through the Otsu method, thinning, smoothing, morphological operators, skeletonization, binary filtering for Delaunay network refinement, and ultimately the detection of fiber network architecture and its descriptors. Per each treatment 8 images were processed.

3.2.8 Quantification of Collagen Fiber Denaturation via SHG

To both visualize and quantify the integrity of the collagen fiber network of the detergent treated tissue, intact samples were imaged enface from the luminal surface of the detergent treated tissue with an Olympus FV1000 TPM. The Olympus FV1000 TPM system was operated with Olympus fluoview software, and was equipped with a Chameleon ultra diode-pumped laser, and a 25x XL Plan N objective with a N.A. of 1.05 and a field of view of 500 μm. The excitation wavelength was chosen at 800 nm at a 5% laser transmissivity. The photomultiplier voltage was maintained at 400 V across all samples for subsequent signal intensity analysis. The emission wavelength was received by a filter set to 400±100nm for second harmonic generation signal of collagen. Image scans were performed at depths of 25 μm, 50 μm, 75 μm, and 100 μm with a sampling speed set to 2 μs/pixel with a 2 line Kalman filter.

Image sections were then imported into ImageJ for intensity analysis. A threshold background subtraction was applied, and then the integrated density function whereby area*intensity. Per each treatment 3 images were processed. This parameter provides a relative measurement of the SHG signal. It has previously been found that denaturation of collagen fibers results in the destruction of the SHG due to the loss of the noncentrosymmetric crystalline structure at the molecular level (208). Additional image stacks were acquired for select samples with an incremental z-step of 0.5 μm to a depth of 100 μm for 3D reconstruction and visualization using Imaris software.

3.2.9 Mechanical Assessment

A MTS Insight Electromechanical 2 kN standard length (MTS Co., Eden Prairie, MN) tensile test machine was used with a ball-burst compression cage to measure the passive biaxial strength of the detergent treated heart tissue. A load cell was used. The ball-burst cage and the MTS machine were used according to the Standard Test Method for Bursting Strength of Knitted Goods, Constant-Rate-of-Traverse (CRT) Ball- burst Test (ASTM D 3787-07). A 25.4mm polished steel ball was advanced at a constant rate (25.4mm/min) through the sample (102). The ring clamp has an internal diameter of 44.5 mm. The ball-burst strength is defined as the force that is required to burst the sample when applied perpendicular to the plane of the sample. The stiffness is defined as the derivative of the force versus displacement curve. Experiments were performed on three separate detergent treated hearts per group on the right ventricular free wall.

3.2.10 Statistical Analysis

A one-way ANOVA was completed for each data set, where the independent variable was detergent treatment, with significance at $p<0.05$. if significance was found, either a post-hoc Dunnett's test or Tukey's test was completed to determine the specific differences between detergent treatment groups with significance at $p<0.05$. Graphs show mean ± standard error unless otherwise specified.

3.3 RESULTS

3.3.1 Urinary Bladder Analysis

3.3.1.1 dsDNA Content

No visible nuclei were observed by imaging of Hematoxylin and Eosin stained sections (Figure 17). dsDNA quantification of detergent treated bladders showed significant removal compared to the control. Bladders treated with SDS contained significantly less dsDNA than those treated with CHAPS, or sodium deoxycholate. SDS was the only detergent able to meet a previously established decellularization criterion of 50 ng dsDNA/mg tissue (209).

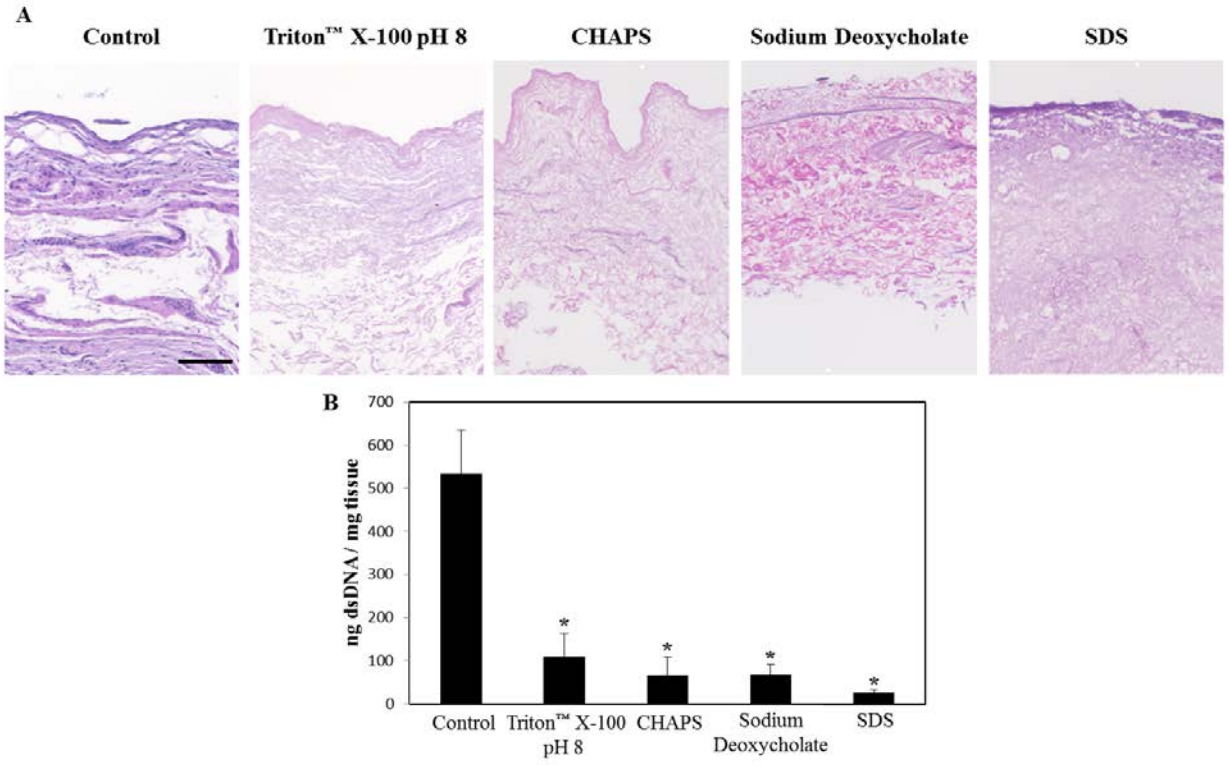

Figure 17: Decellularization assessment of the detergent treated bladder with (A) H&E to identify cellular content, and (B) Picogreen assay to quantify dsDNA. Scale bar represents 200 µm. Graph shows mean ± standard error, and * indicates significance from control at $p<0.05$.

3.3.1.2 Collagen, Sulfated GAG, and Growth Factor Content

While bladders treated with Triton™ X-100, CHAPS, and sodium deoxycholate retained a level of soluble collagen similar to that of the control, treatment with SDS resulted in a significant loss of detectable soluble collagen (Figure 18). While this assay only detected soluble collagen such that higher levels of non-soluble remnant collagen may still exist, this finding indicated that detergent treatment with SDS resulted in either a decrease in soluble collagen present or modification of the molecular structure to the point of insolubility. The higher level of soluble collagen for Triton X-100 compared to the water control is an artifact of the normalization to dry weight. More specifically, the relative density of ECM to total weight is increased after

decellularization for Triton X-100 because of the removal of cellular content compared to the control. Bladders treated with Triton™ X-100 retained GAGs similar to that of the control, while bladders treated with sodium deoxycholate and SDS retained no detectable GAGs. CHAPS retained a lesser amount of detectable GAGs than the control. The majority of the detergent treated bladders retained less VEGF and bFGF than the control (Figure 19), but there was almost no detectable VEGF for bladders treated with sodium deoxycholate and SDS.

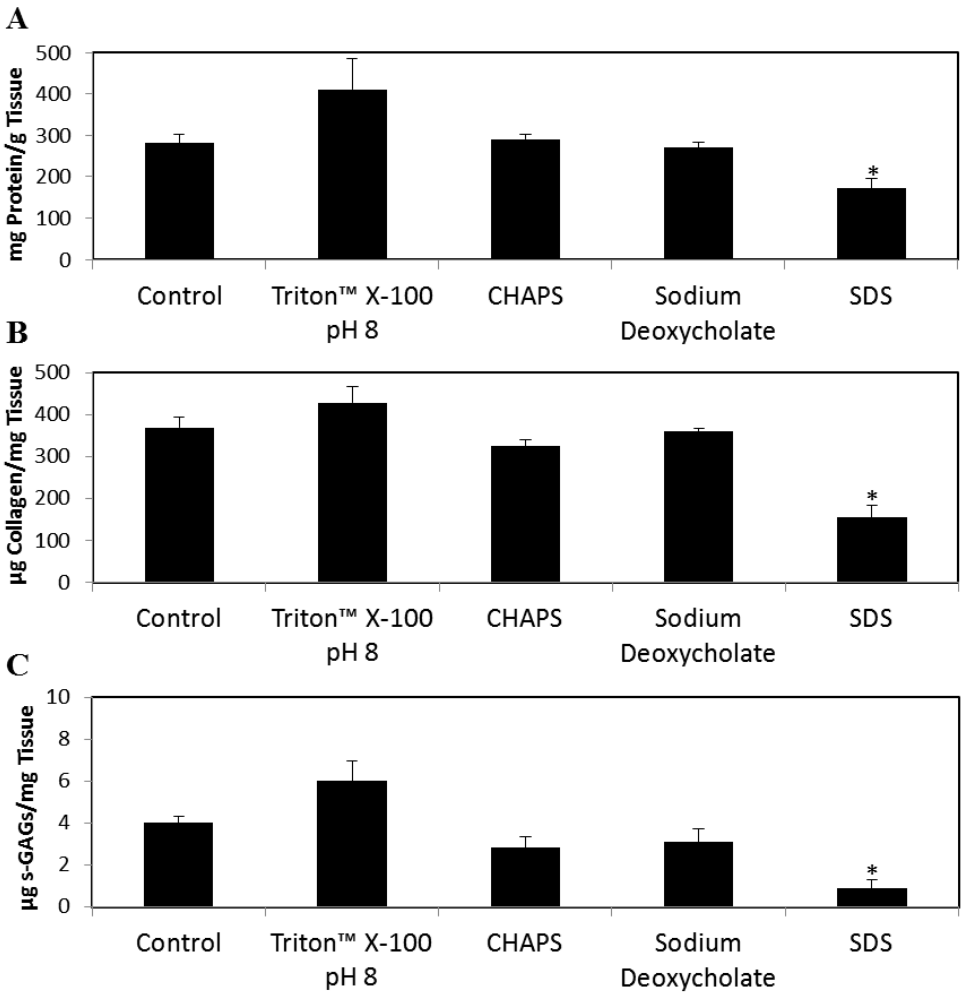

Figure 18: Biochemical assay of the detergent treated bladder to quantify soluble (A) protein, (B) collagen, and (C) GAGs. Graph shows mean ± standard error, and * indicates significance from control at $p<0.05$.

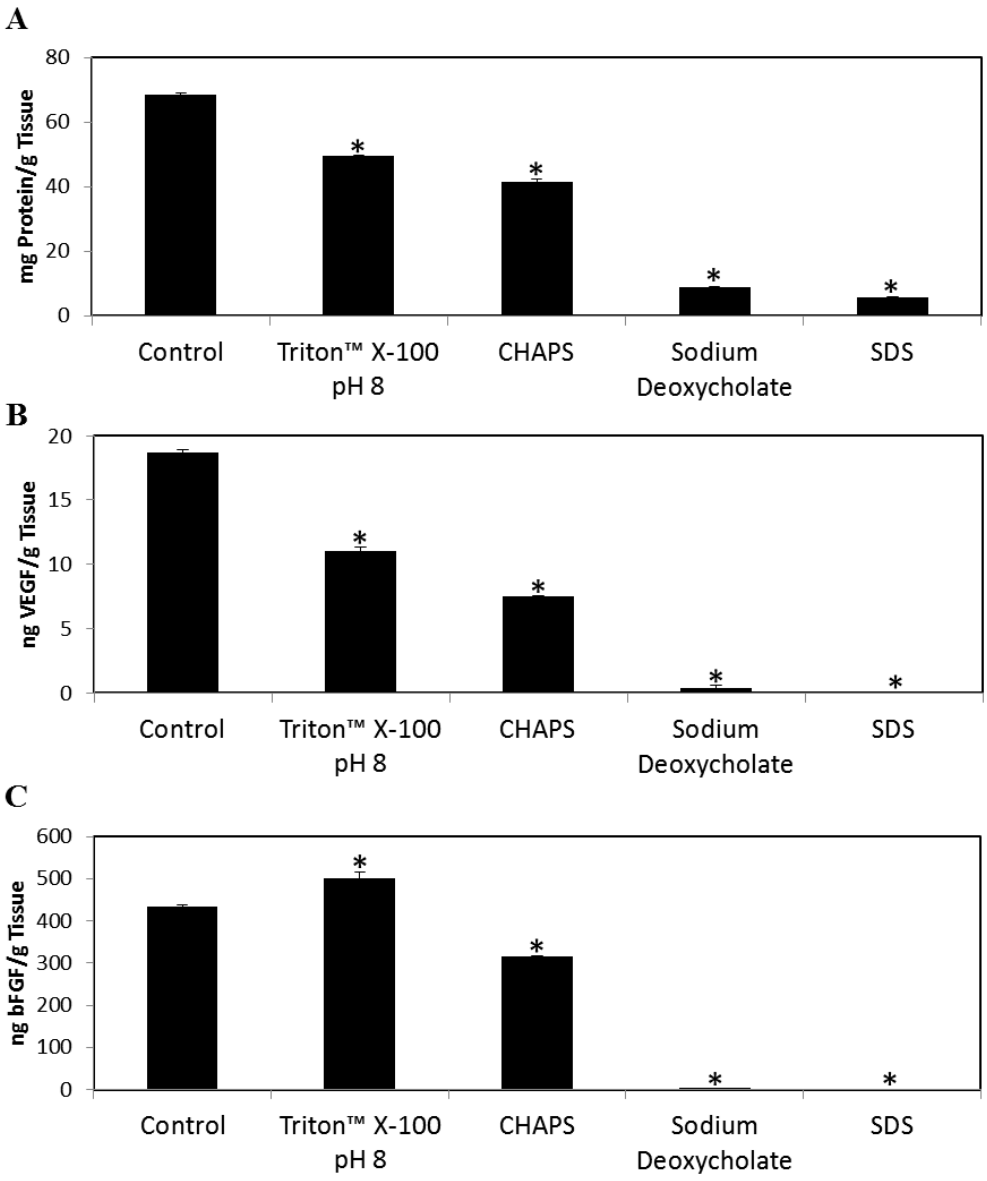

Figure 19: Biochemical assays to quantify soluble (A) protein, (B) VEGF, and (C) bFGF normalized to dry weight tissue. Graph shows mean ± standard error.

3.3.1.3 Immunolabeling

The control showed positive staining at the BMC surface of collagen I, collagen IV, collagen VII, and laminin as previously reported (Figure 20) (200). All bladders treatments were positive for collagen I staining. No detergent treated bladders stained positive for collagen VII, or

laminin. While bladders treated with CHAPS and SDS did not stain positive for collagen IV, bladders treated with Triton™ X-100 and sodium deoxycholate had positive expression of collagen IV. However, this positive staining was not localized to the surface as would be expected for an intact BMC.

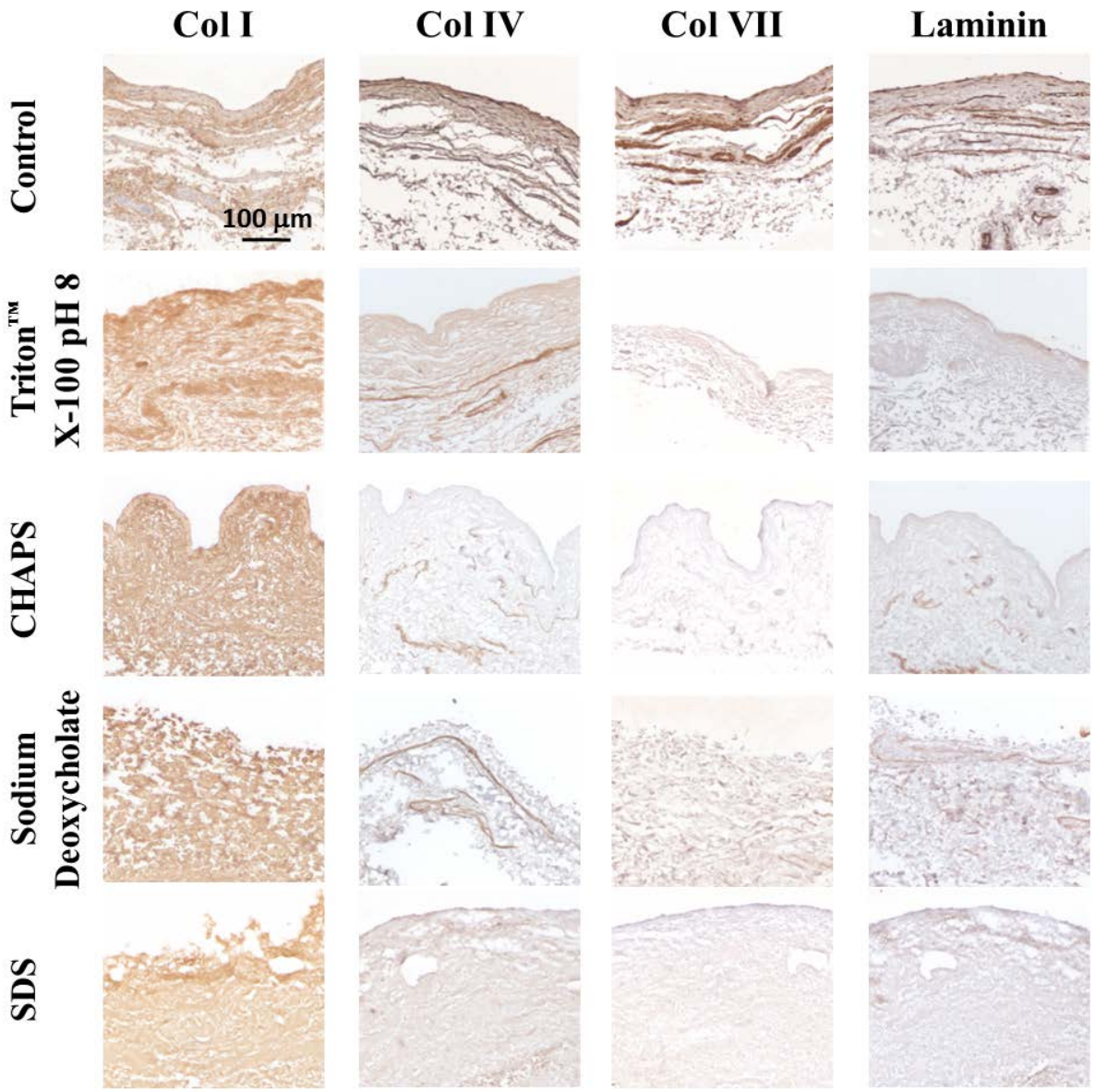

Figure 20: Immunolabeling of proteins associated with the BMC for detergent treated bladder to assess BMC integrity. Scale bar represents 100 µm.

3.3.1.4 Movats Stain

Bladders treated with Triton™ X-100 and sodium deoxycholate retained elastin fibers, whereas CHAPS had no visible elastin fibers and SDS had only a small portion of thin fragmented fibers (Figure 21). GAGs were visible in both bladders treated with Triton™ X-100 and CHAPS while not visible for bladders treated with sodium deoxycholate and SDS. This observation was consistent with the sulfated GAG measurement (Figure 18).

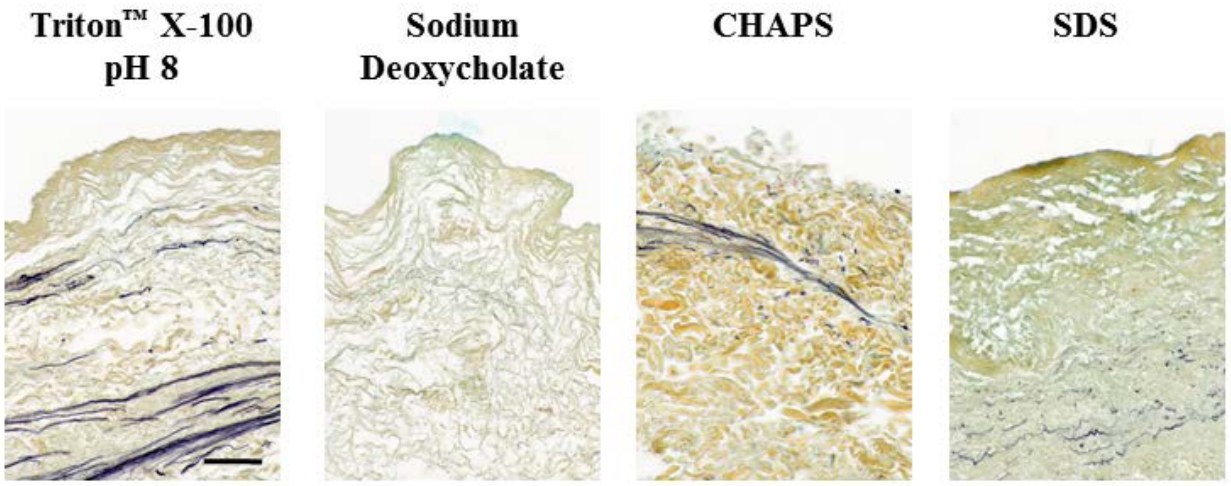

Figure 21: Movats Pentachrome of the detergent treated bladder where yellow, blue, and purple represents collagen, proteoglycans and GAGs, and elastin, respectively. Scale bar represents 100 µm.

3.3.1.5 Analysis of the Fiber Network

SEM of the luminal surface of bladders showed qualitatively that treatment without a detergent, with Triton™ X-100, or with sodium deoxycholate retained an intricate fiber network (Figure 22A). However, treatment with CHAPS and SDS resulted in an amorphous structure lacking distinct fibers. The fiber diameter was not different for bladders treated with Triton™ X-100 or sodium deoxycholate compared to the control (Figure 22B). While there was a slightly smaller pore size for bladders treated with Triton™ X-100 and sodium deoxycholate compared to the

control, and a higher node density for bladders treated with Triton™ X-100 these changes were small compared to previously published variations (207, 210). Thus, bladders treated with Triton™ X-100 and sodium deoxycholate were able to retain the fiber network original configuration. TPM imaging confirmed a loss of a distinct fiber network for bladders treated with SDS compared to Triton™ X-100 (Figure 23). The lower collagen signal intensity for bladders treated with SDS indicates fiber denaturation. The higher signal intensity value for Triton™ X-100 and sodium deoxycholate compared to the water control may be due an increase in the density of ECM constituents from a loss of cellular material. The signal intensity values provide a relative comparison of detergent treatments that are consistent in finding with visual observations of the fiber network from SHG and SEM images.

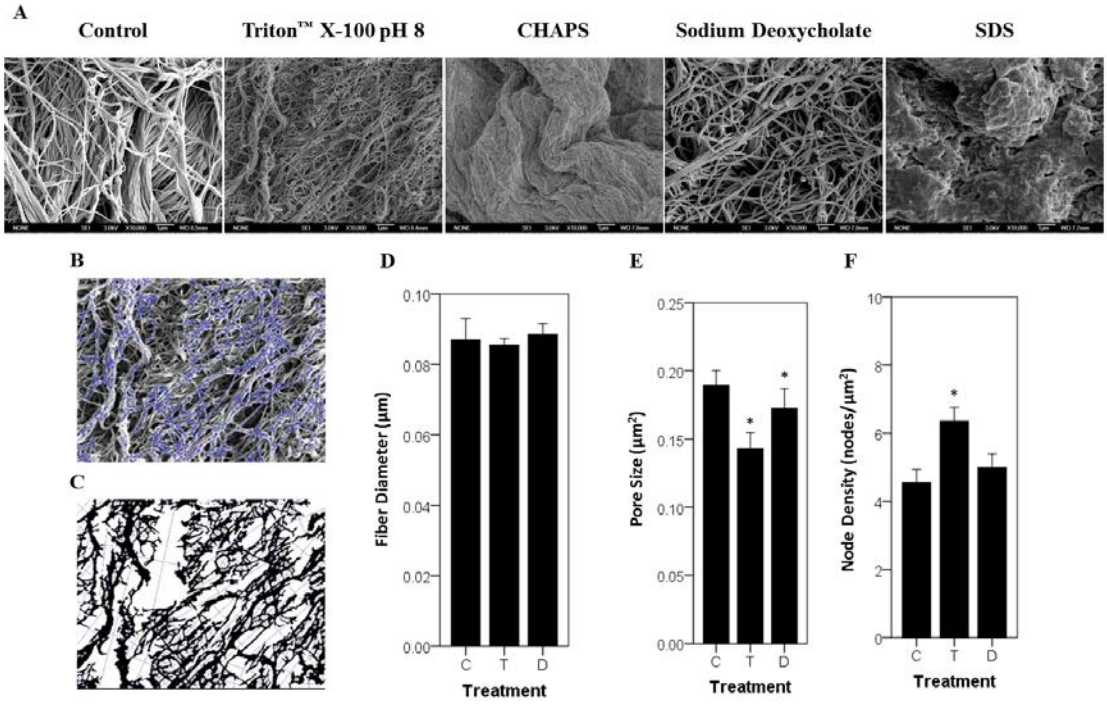

Figure 22: (A) Scanning electron microscopy of the detergent treated bladder fiber network. An (B-C) automated algorithm was applied to quantify fiber network parameters of (D) fiber diameter, (E) pore size, and (F) node density [24]. C, T, and D represent the control, Triton™ X-100 pH 8, and sodium deoxycholate, respectively. Graph shows mean ± standard error, and * indicates significance at $p<0.05$.

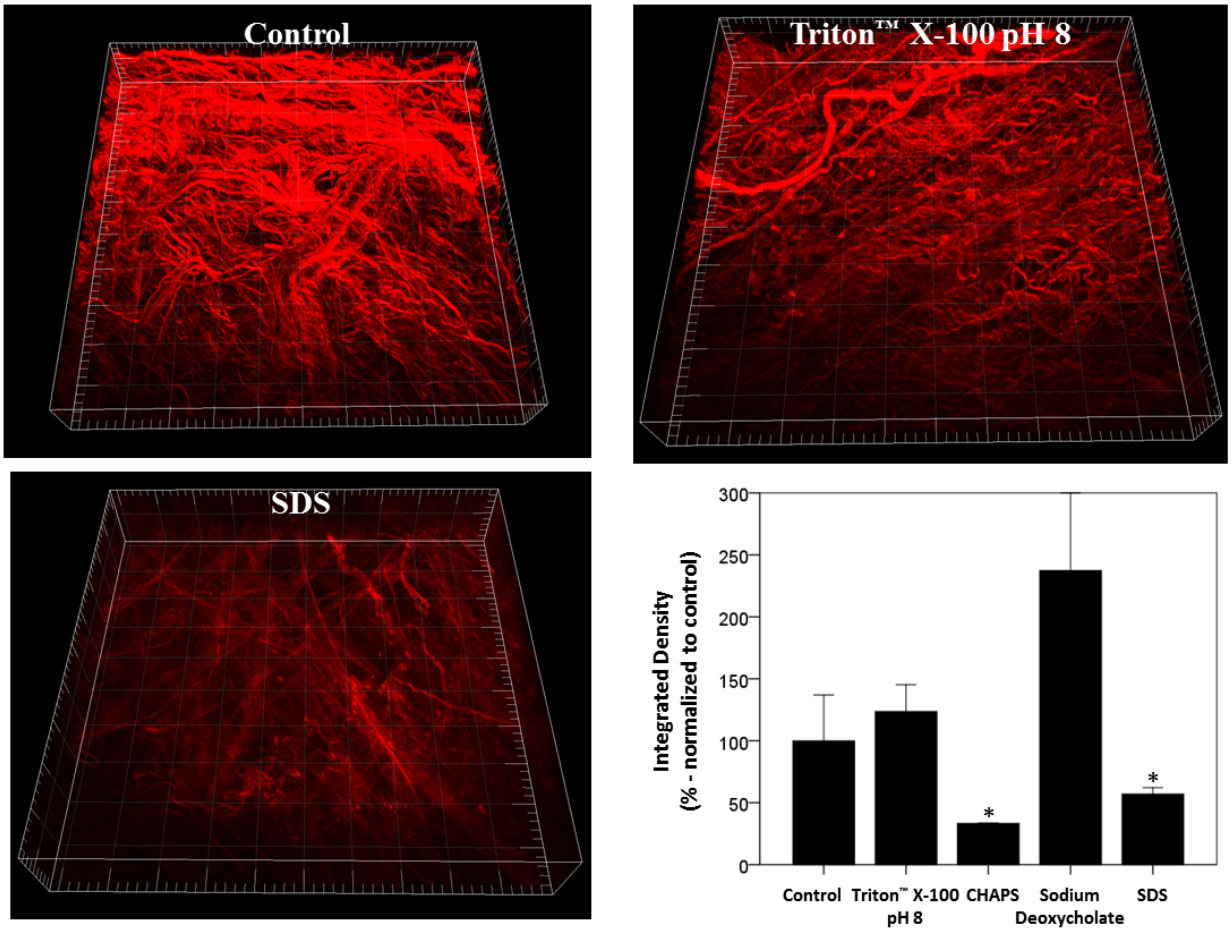

Figure 23: 3-dimensional collagen fiber network rendering of the detergent treated bladder from SHG signal with TPM. Major tick represents 50 µm, whereby the total length and depth is 500 µm and 100 µm, respectively. An integrated density function was applied and normalized to the control. Graph shows mean ± standard error, and * indicates significance at $p<0.05$.

3.3.2 Heart Analysis

3.3.2.1 dsDNA Content

No visible nuclei were observed by imaging of Hematoxylin and Eosin stained sections (Figure 24A). dsDNA quantification of the detergent treated hearts showed significant removal compared to the control (Figure 24B). Hearts treated with Triton™ X-100 with a pH 8 had the

largest amount of remnant dsDNA above 1000 ng/mg. Increasing the pH of Triton™ X-100 to 11.4 more than halved the amount of remnant dsDNA. Hearts treated with sodium deoxycholate and SDS had the least amount of remnant dsDNA reduced to less than 100 ng/mg (209). Thus, the heart compared to the bladder required ionic detergents to achieve decellularization. This may be potentially due to unique differences in composition and structure such as the myocardium containing a higher tissue density and thickness than that of the bladder.

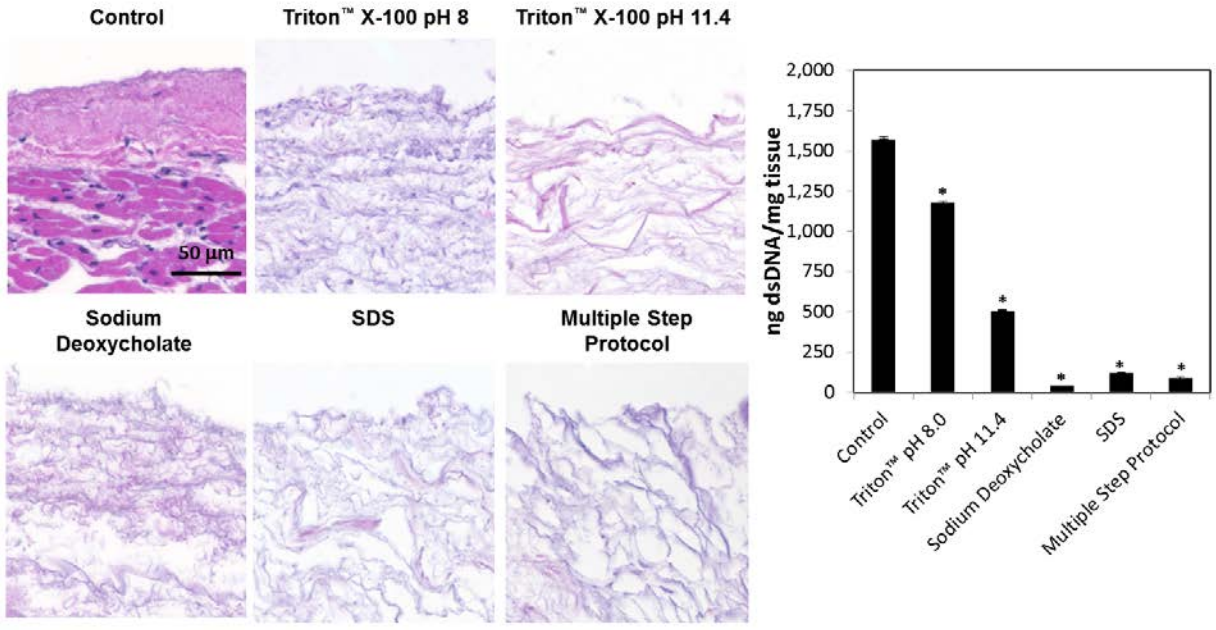

Figure 24: Decellularization assessment of the detergent treated heart with (A) H&E to identify cellular content, and (B) Picogreen assay to quantify dsDNA. Scale bar represents 50 µm. Graph shows mean ± standard error, and * indicates significance at $p<0.05$.

3.3.2.2 Collagen and Sulfated GAG Content

No decrease in soluble collagen was found for the detergent treated hearts (Figure 25). A decrease in soluble GAGs was found with treatment of all detergents except for Triton™ X-100 pH 8.

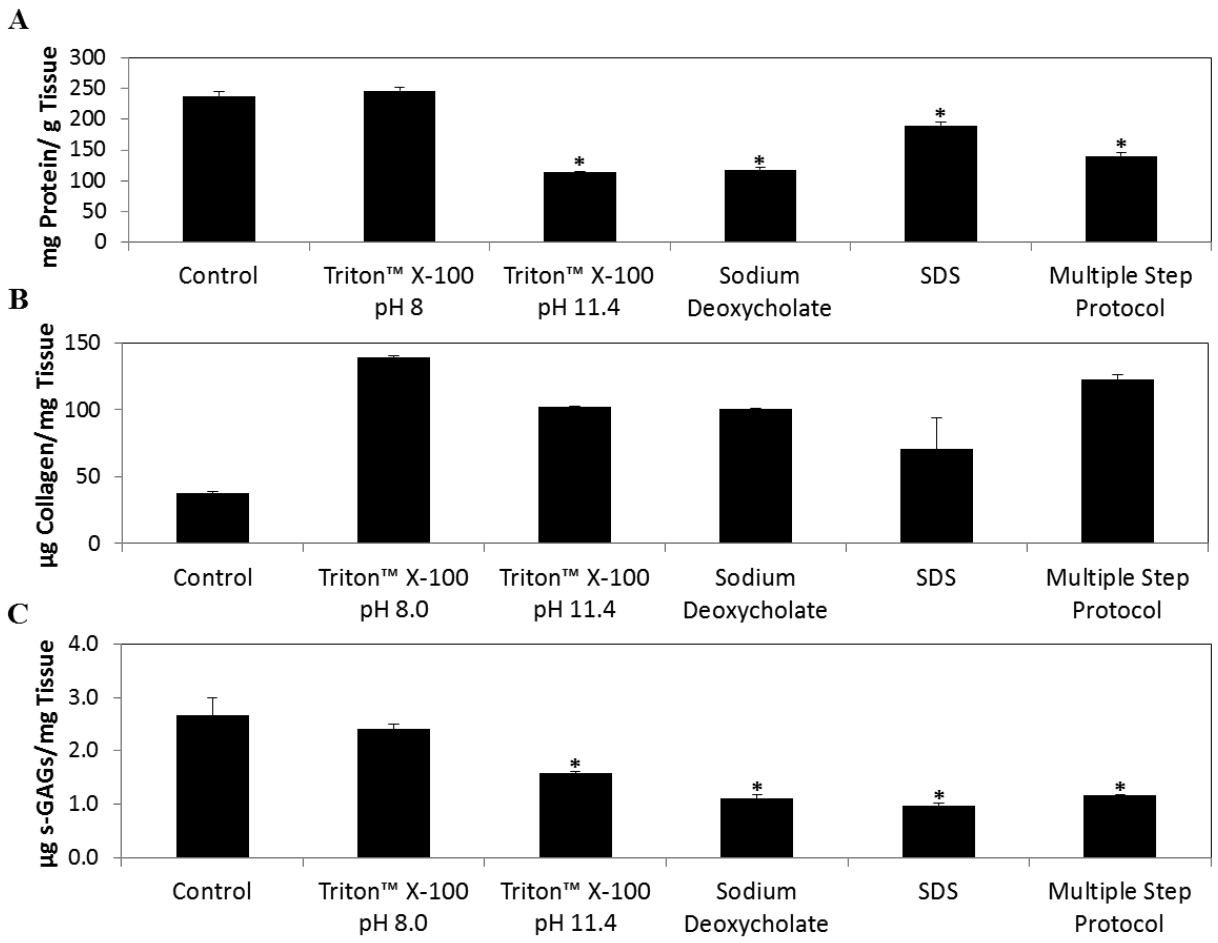

Figure 25: Biochemical assay of the detergent treated heart to quantify soluble (A) protein, (B) collagen, and (C) GAGs. Graph shows mean ± standard error, and * indicates significance from control at $p<0.05$.

3.3.2.3 Analysis of the Fiber Network

SEM of the endocardial surface of the heart showed similar findings to that of the luminal surface of the bladder (Figure 26): Hearts treated with Triton™ X-100 pH 8, and sodium deoxycholate retained the original collagen fiber network compared to treatment with SDS. Surprisingly, increasing the pH of Triton™ X-100 to 11.4 resulted in an increase fiber diameter and decrease pore size possibly due to fiber fusion from denaturation (Figure 27). A multiple step protocol was also found to retain the original collagen fiber network.

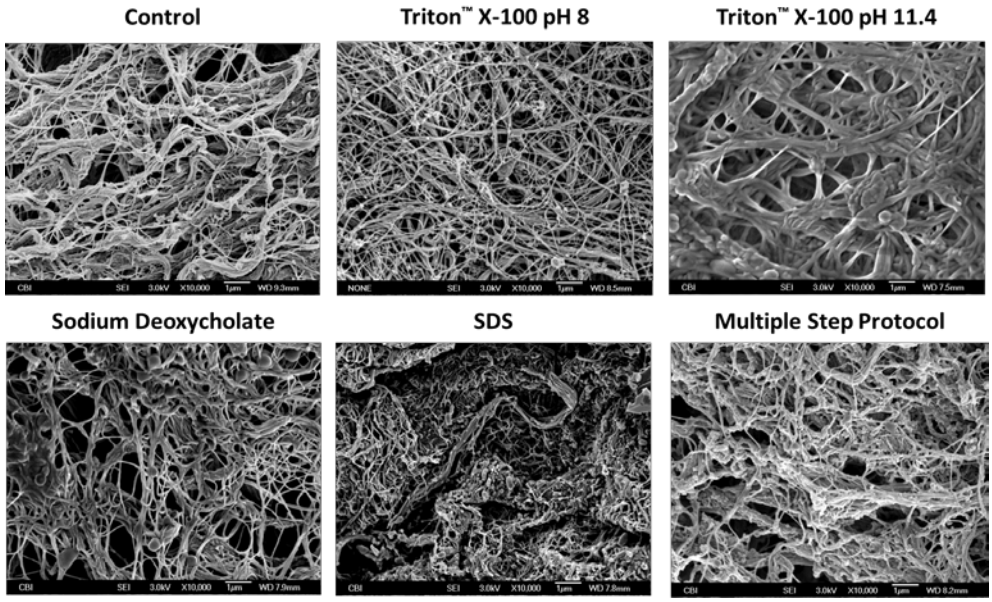

Figure 26: Scanning electron microscopy of the detergent treated heart fiber network.

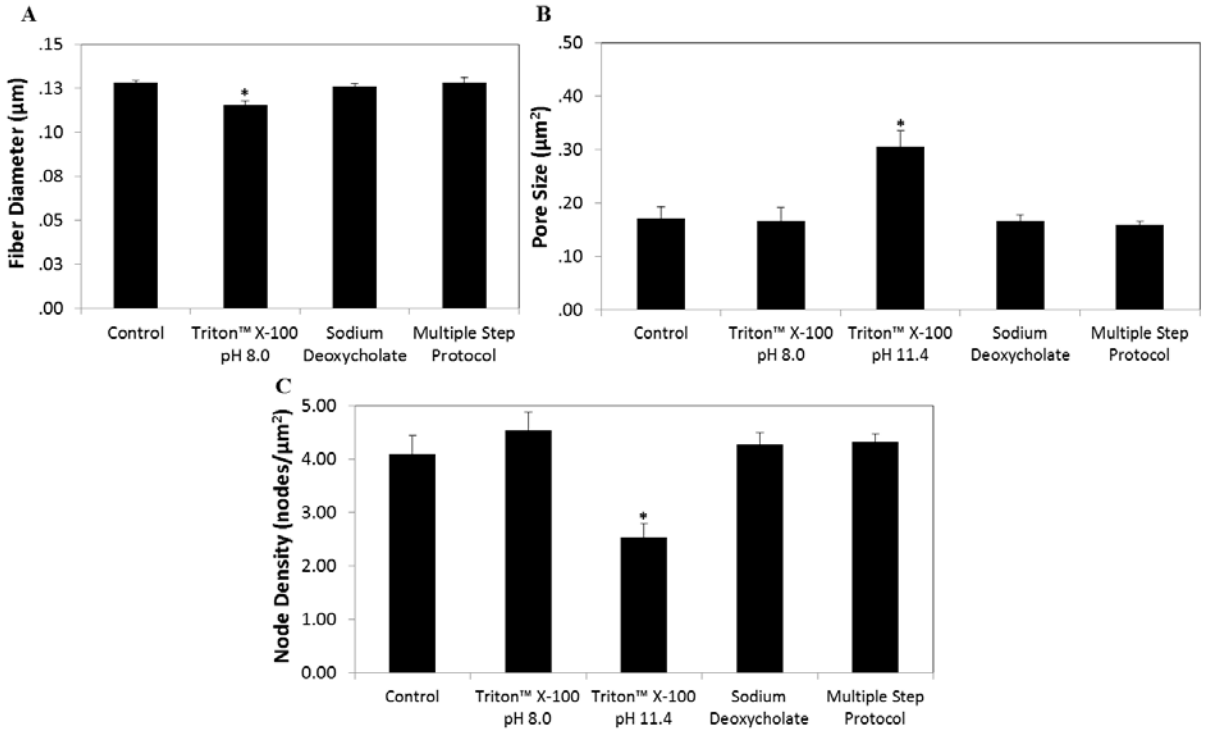

Figure 27: automated algorithm was applied to Figure 26 to quantify fiber network parameters of (A) fiber diameter, (B) pore size, and (C) node density [24]. Graph shows mean ± standard error, and * indicates significance at $p<0.05$.

TPM imaging confirmed a loss of a distinct fiber network for hearts treated with SDS compared to Triton™ X-100 (Figure 28). The elastin fiber network was completely lost for treatment with either SDS or Triton™ X-100 at a pH of 11.4 (Figure 29).

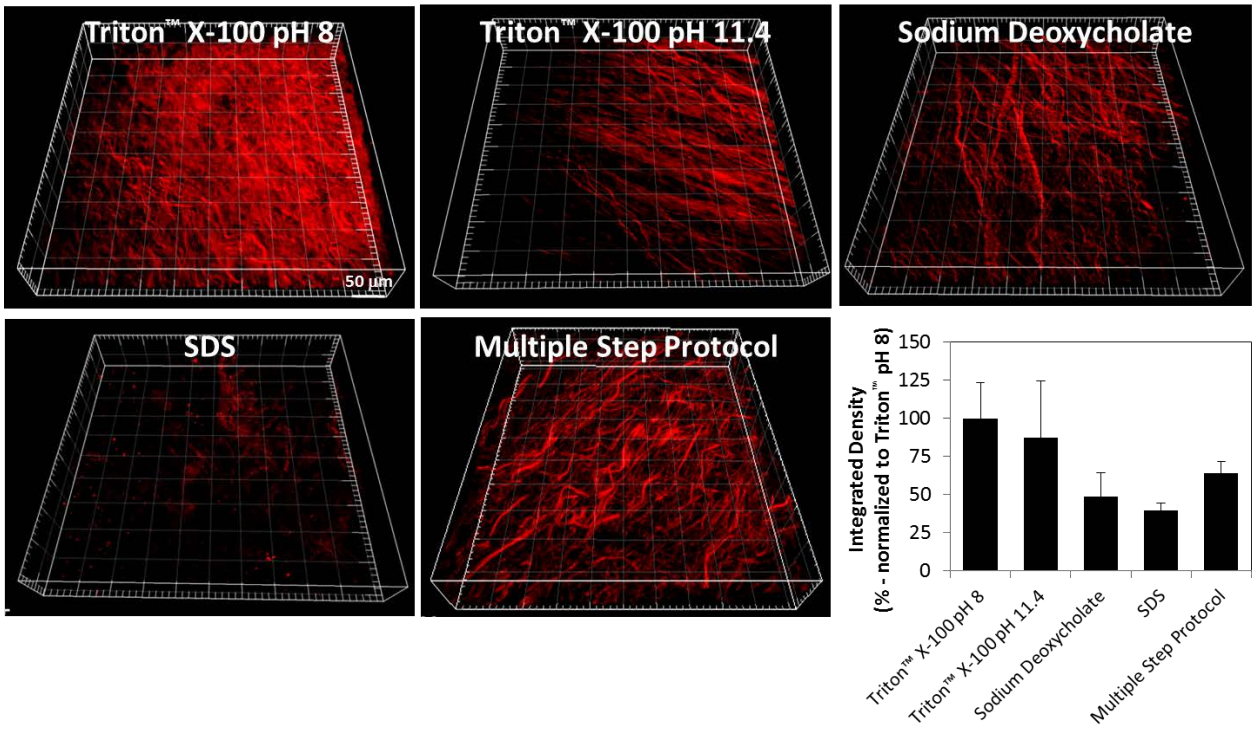

Figure 28: 3-dimensional collagen fiber network rendering of the detergent treated heart from SHG signal with TPM. Major tick represents 50 µm, whereby the total length and depth is 500 µm and 100 µm, respectively. An integrated density function was applied and normalized to the control. Graph shows mean ± standard error.

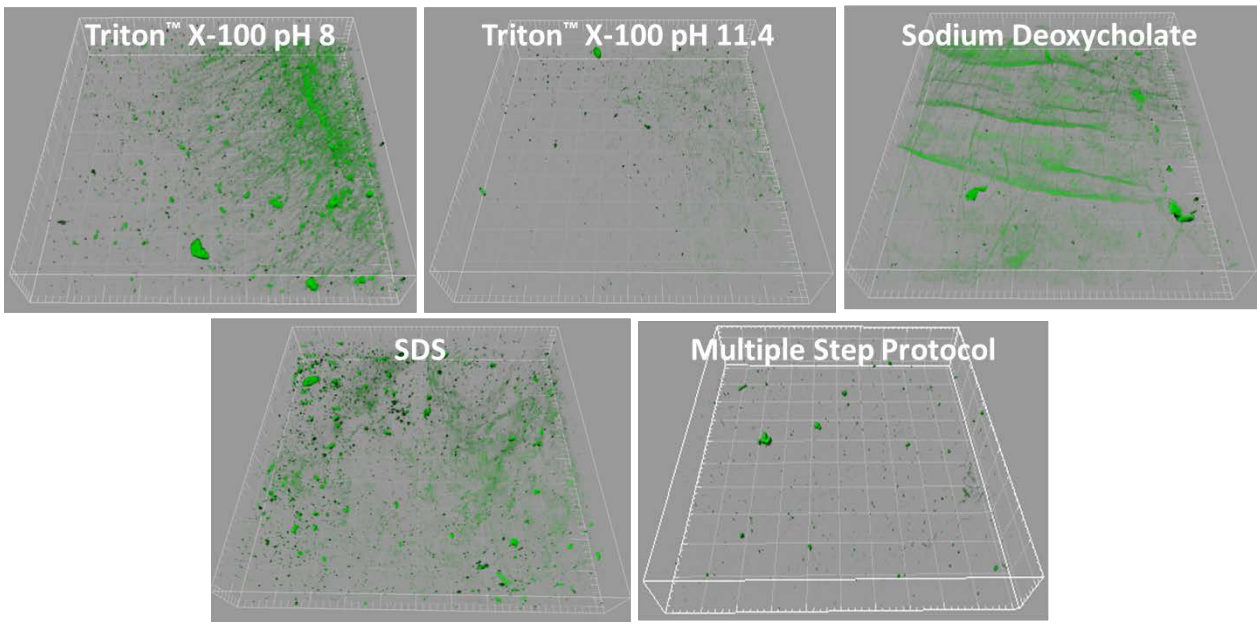

Figure 29: 3-dimensional elastin fiber network rendering of the detergent treated heart from autofluorescence. Major tick represents 50 µm, whereby the total length and depth is 500 µm and 100 µm, respectively.

3.3.2.4 Mechanical Evaluation

The passive failure force and stiffness of detergent treated heart tissue was found to be similar to that of the control (Figure 30). Thickness was found to decrease significantly after treatment as the muscle was removed during the decellularization process.

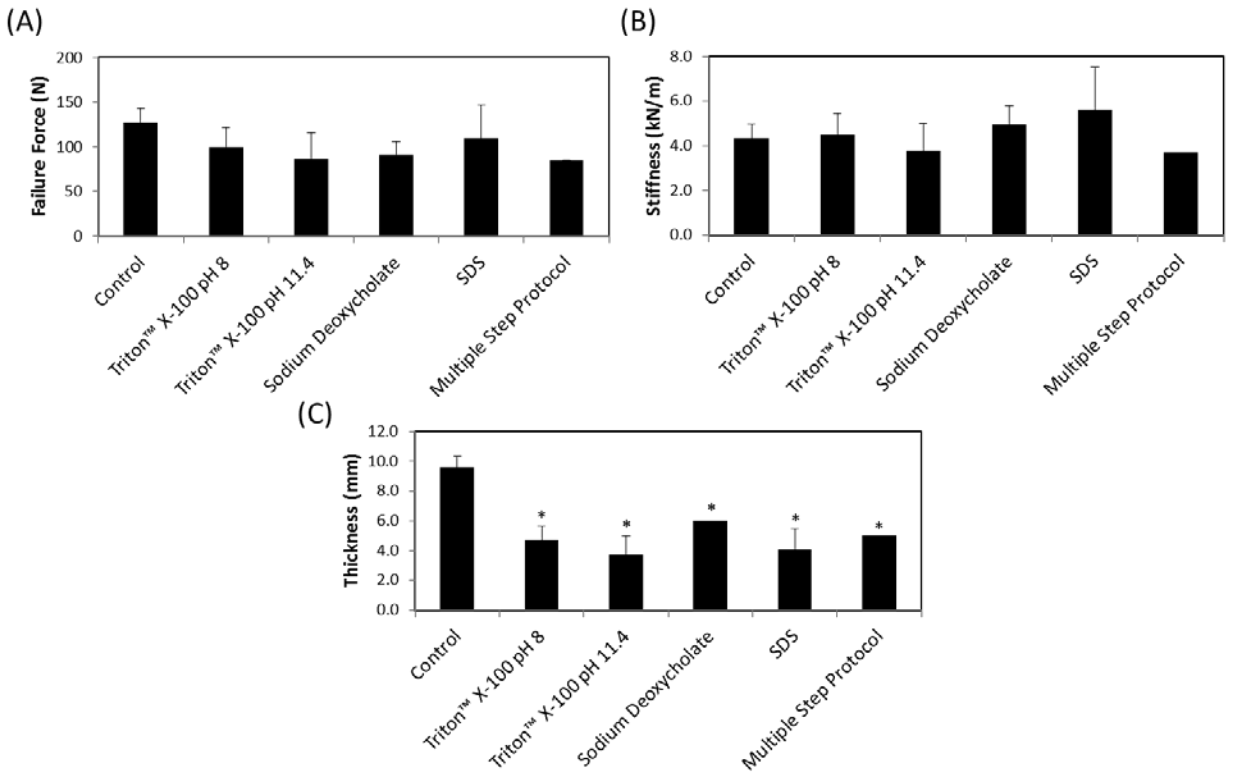

Figure 30: Ball burst test of detergent treated heart tissue with (A) failure force, (B) stiffness, and (C) the associated initial thickness. Graph shows mean ± standard error, and * indicates significance from control at $p<0.05$.

3.1 DISCUSSION

Thorough decellularization of tissues and organs is essential for promoting a constructive remodeling host response when such decellularized structures are used as therapeutic bioscaffolds for cardiac repair. However, exposure to certain decellularization agents can markedly disrupt the ECM. While some disruption of the ECM is inevitable, efforts should be made to minimize these detrimental effects. Four detergents commonly used for decellularization

of tissues and organs were systematically evaluated and compared for their effect on the composition, structure, and mechanics of two clinically relevant source tissues for cardiac repair.

The detergents investigated were Triton™ X-100, sodium deoxycholate, CHAPS, and SDS. The detergents (88) were selected because of their frequent use as decellularization agents and their different chemical characteristics. Triton™ X-100 is non-ionic and disrupts lipid–lipid and lipid–protein interactions, while leaving protein–protein interactions intact. In contrast, sodium deoxycholate and SDS are anionic detergents which can solubilize cytoplasmic and nuclear membranes, denature ECM proteins, and disrupt native tissue structure. CHAPS is zwitterionic and exhibits properties of both non-ionic and anionic detergents. Therefore, it is not surprising that these detergents each have distinctly different effects on the ECM. Results of this aim show that these detergents may change the ultrastructure and composition of the ECM. While Triton™ X-100 most effectively retains the composition and structure of the ECM, it is less effective at removing dsDNA from dense and thick tissues such as the heart. Similarly, while SDS is effective at removing dsDNA, it is clear that it substantially damages the composition and structure of the ECM. Sodium deoxycholate was able to effectively remove dsDNA and retain the structure of the ECM. Surprisingly, while some detergents damaged the structure of the heart, the passive failure strength was unaffected. The passive failure strength is only one mechanical parameter measured at failure, and therefore does not necessarily imply that the mechanics of the heart are unaffected by detergent treatment.

This aim provides the first comprehensive investigation of detergents for both tissue and whole organ decellularization examining the relationship of composition, structure and mechanics. These findings provide a template to formulate novel decellularization protocols depending on the complexity of the tissue of interest. For example, a thin cornea may possibly be

decellularized with a non-harsh detergent such as Triton™ X-100 to remove cellular material, but a dense thick tissue such as dermis may require a multiple step protocol. Indeed, in this aim a multiple step protocol that serially applies Triton™ X-100 and then sodium deoxycholate (190) was applied to the heart and successfully decellularized the tissue while retaining its structure.

The choice of detergent used for the decellularization of a tissue or organ is an important factor in the preparation of an ECM scaffold for therapeutic applications. Each detergent, depending on its chemical characteristics, has unique and distinct effects on ECM composition and structure. Less disruptive non-ionic detergents, such as Triton™ X-100, will maintain the native structure and composition compared to harsher detergents, such as SDS, which denature essential ligands and proteins within the ECM. The disruption or denaturing of the native ECM architecture may negatively impact the interaction of the host cells with the ECM scaffold. The results of this study can aid in the formulation of tissue and organ decellularization protocols such that the innate biological activity of the resulting ECM scaffold is maximally preserved.

4.0 CYTOCOMPATIBILITY OF DETERGENT TREATED TISSUE[3]

4.1 INTRODUCTION

Specific Aim 2 identified damage to both the composition and structure of two relevant source tissues used to manufacture ECM scaffolds for cardiac repair after treatment with the detergents CHAPS and SDS. However, it is unknown whether these distinct structural differences may affect an ECM scaffold's cytocompatibility. While a recent study found no difference in in-vitro cytocompatibility between three different rodent heart decellularization protocols, only a C2C12 myoblast cell line was used to compare multiple step protocols (113). The observed compositional and structural changes in Specific Aim 2 may correspond with damage to specific domains of ECM constituents called ligands that are critical to cell-ECM interaction, and thus, warrant a more in depth cytocompatibility analysis.

[3]This work has been adapted from the following published manuscript:

Faulk DM, Carruthers CA, Warner HJ, Kramer CR, Reing JE, Zhang L, D'Amore A, Badylak SF. The effect of detergents on the basement membrane complex of a biologic scaffold material. Acta Biomaterialia. 2013; Doi: 10.1016/j.actbio.2013.09.006.

A few previous examples of the composition and structure of an ECM scaffold influencing the host response should be recalled:

1. Remnant cellular material (104, 105), or cross-linking an ECM scaffold is characterized by chronic inflammation and scar tissue formation.
2. The method of terminal sterilization correlates with distinct differences in the host response (43).
3. Site specific ECM scaffolds promoted significant improvement in differentiation and function in an in-vitro cell culture of a primary cell line (62, 63).

Thus, the methodology of detergent treatment in Specific Aim 2 on two source tissues is repeated to investigate the relationship of an ECM scaffold's composition and structure to cytocompatibility. It is hypothesized that the less harsh detergents which were shown in Specific Aim 2 to retain the structure and composition of ECM will have a higher level of cytocompatibility compared to the harsher detergents.

4.2 METHODS

4.2.1 Tissue Source

The same two source tissues were used for their relevance in application to cardiac repair: Urinary bladder and heart. The tissue preparation protocol as described in Specific Aim 2 was followed. In brief, porcine urinary bladders were obtained from animals at a local abattoir (Thoma's Meat Market, Pittsburgh PA). Bladders were frozen (>16 hr at −80 °C) and thawed completely before use. The BMC and underlying lamina propria were mechanically isolated and

harvested from the bladders as previously described (102, 186, 194). The term detergent treated bladder refers to detergent treatment of the BMC and lamina propria of the bladder. Porcine hearts were obtained under controlled conditions to minimize damage to the vasculature near the surface (Tissue Source, Lafayette Indiana). Hearts were frozen (>16 hr at −80 °C) and thawed completely before use. For subsequent cell seeding after decellularization the right ventricular free wall was used because of its previous use as a cardiac patch (87).

4.2.2 Decellularization Protocol

The decellularization protocol as described in Specific Aim 2 was followed. In Brief, tissues were subjected to one of four commonly used detergents:

1. A non-ionic detergent called Triton™ X-100
2. A zwitterionic detergent called 3-[(3-cholamidopropyl)dimethylammonio]-1-propanesulfonate (CHAPS)
3. An ionic detergent called sodium deoxycholate
4. An ionic detergent called sodium dodecyl sulfate (SDS)

The concentration for decellularization of bladder and heart was chosen to both replicate those used in the literature while maintaining similar molarities (Table 6). CHAPS was only used for treatment of the bladder due to both cost constraints and its usage in the literature for only decellularization of a sheet such as the cornea. Table 7 from Specific Aim 2 describes in detail the decellularization protocol. Briefly, porcine bladders were treated with detergents by mechanical agitation while hearts were treated with detergents by whole organ retrograde perfusion. A multiple step protocol from the literature (71, 190) was also included to investigate serial detergent usage for heart decellularization because whole organs are more difficult to

decellularize. The goal of detergent treatment was not necessarily to reach the criteria for successful decellularization, but to compare the effect of detergent treatments on the source tissue under similar controlled conditions. Lastly, these detergent treated tissues were sterilized via gamma irradiation at a dose of 2 x 10^6 RADS.

4.2.3 Cell Seeding and Culture

The luminal surface of the sterilized detergent treated bladder and heart (i.e. endocardial) was placed facing up in a 6 well plate. The luminal surface was selected because of the presence of a BMC in the source tissue, an important structure for supporting endothelial cells (200). The regrowth of endothelium is critical to any cardiac repair strategy. Two cell lines were selected for their relevance to cardiac repair: An immortalized human microvascular endothelial cell line (HMEC-1) and a mouse myoblast cell line referred to as C2C12 cells. HMECs were chosen due to their relevance in assessing in-vitro whether endothelial cells can re-endothelialize on the surface of detergent treated tissues. C2C12 cells were chosen to assess if the detergent treated heart can support a muscle cell line. While it is understood that C2C12 cells differentiate into skeletal muscle instead of cardiac muscle this cell line was chosen as a first approximation of assessment.

HMECs (a gift from Francisco Candal, Center for Disease Control and Prevention, Atlanta, GA) were cultivated in MCDB-131 medium containing 10% fetal bovine serum, 2 mM L-glutamine, 100 U/mL penicillin and 100 µg/mL streptomycin. MCDB-131 medium was from Invitrogen (Carlsbad, CA); all other reagents for cell growth were from Thermo Fisher Hyclone (Logan, Utah). HMEC cells were grown at 37°C in 5% CO_2 and were harvested for seeding when they were approximately 100% confluent. C2C12 cells were cultured in Dulbecco's

Modified Eagle Medium (DMEM) (Invitrogen) supplemented with 10% fetal bovine serum (FBS, Hyclone) and 100 U/ml penicillin/100 mg/ml streptomycin (Invitrogen). C2C12 cells were grown at 37°C in 5% CO_2 and were harvested for seeding when they were approximately 70% confluent.

HMECs and C2C12 cells were seeded on the luminal surface of each treatment group in triplicate. A total of 1 x 10^6 cells were cultured on each detergent treated tissue within a 2 cm diameter stainless steel culture ring containing 5 ml of culture medium. Detergent treated tissues were then placed in an incubator at 37°C in 5% CO_2 for 24 hrs of culture, at which time the culture rings were removed and the seeded samples were transferred to a new 6 well plate with fresh media. Culture media was then replaced on day 2 and day 5. After 7 days of culture, seeded samples were fixed in 10% neutral buffered formalin, or gluteraldehyde for subsequent analysis.

4.2.4 Scanning Electron Microscopy

SEM was used to examine the surface topology of bladders treated with each detergent. SEM was also taken of the HMEC seeded detergent treated tissues after 7 days of culture on each sample. Samples were fixed in 2.5% glutaraldehyde in 1X PBS, cut into blocks of approximately 8 mm^3, and washed thoroughly in 1X PBS for three times at 15 minutes each. Samples were then fixed in 1% OsO_4 in 1X PBS for 15 minutes each, and dehydrated in graded series of alcohol (30%-100%) baths for 15 minutes each. Samples were then critically point dried with Hexamethyldisiloxane mounted on studs, sputter coated, and stored in a desiccator until imaged. SEM images were captured enface using a JEOL 6335F Field Emission SEM with backscatter detector.

4.2.5 Semi-Quantitative Cell Scoring

After 7 days of culture samples were fixed in formalin for at least 24 hours, embedded in paraffin and cut into 5 µm transverse sections. Detergent treated bladder tissue seeded with HMEC, and detergent treated cardiac tissue seeded with HMEC and C212 cells were sectioned and stained with Hematoxylin and Eosin (H&E). Images were taken of the HMEC – luminal interface. The images were then evaluated by five blinded investigators using a standardized system (106). Criteria included cellular infiltration, confluence, and cell phenotype. All aspects were evaluated on a scale of 0 to 100 percent described in Table 8 and Figure 31.

Table 8: Description of semi-quantitative scoring of HMECs and C2C12 cells following seeding on the luminal surface of detergent treated urinary bladder and heart.

Confluence (%)	The confluence score is defined as the percentage of the surface covered with cells. A score of 100 would indicate a fully coated surface with adjoining cells and no gaps.
Phenotype (%)	The phenotype score is defined as the percentage of healthy appearing cells. A healthy cell is fully adhered to surrounding tissue and other cells. An unhealthy cell is round and not adhered to the surrounding tissue or other cells. Healthy HMECs cells become flat while C2C12 cells are more spindle shaped like a fibroblast.
Infiltration (%)	The infiltration score is defined as the percentage of the total depth in which cells have migrated within the tissue. For example, if cells are found halfway into the tissue, this would correspond to an infiltration score of 50.

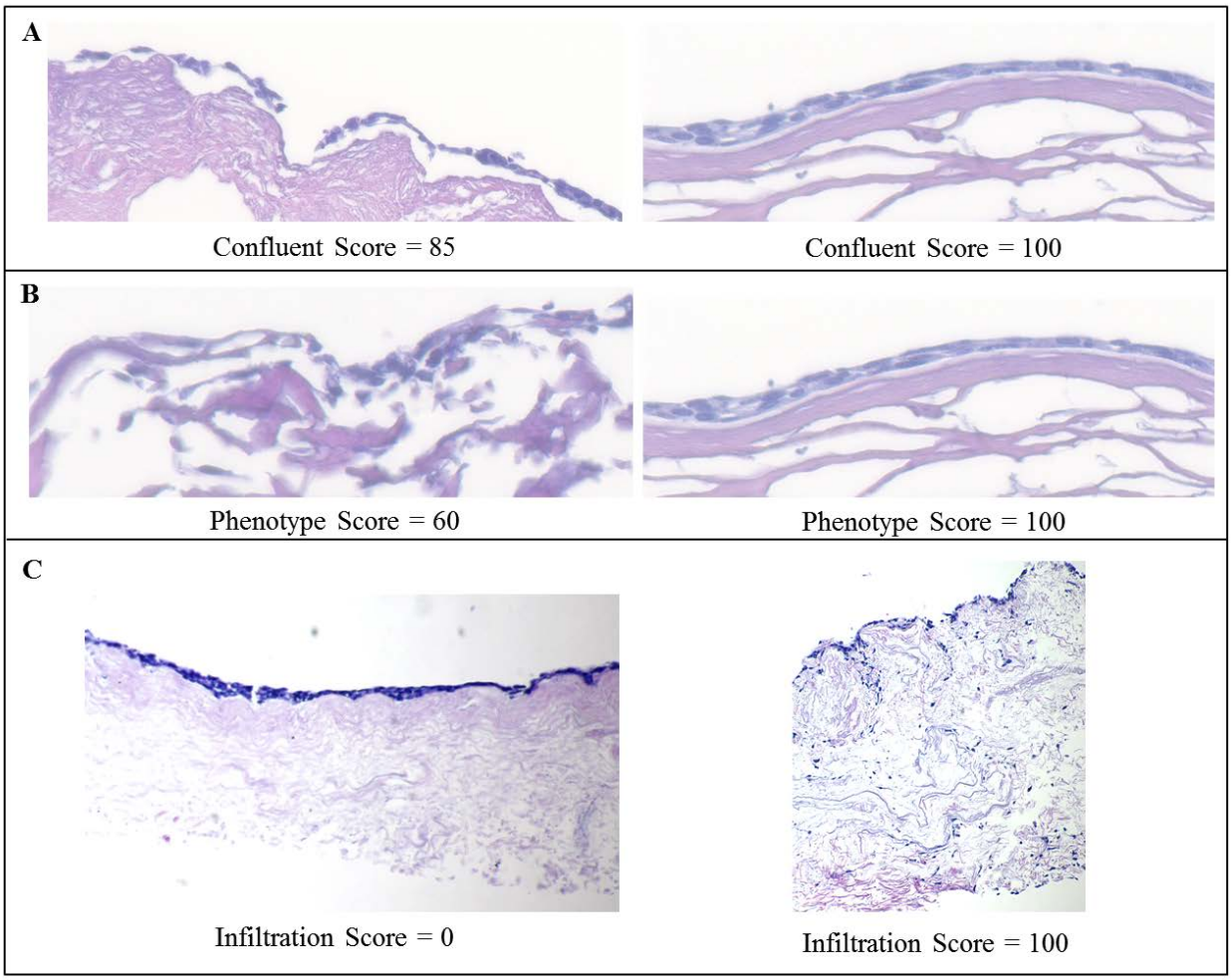

Figure 31: Example images with associated semi-quantitative score for the metrics of (A) confluence, (B) phenotype, (C) and infiltration.

4.2.6 Immunolabeling of Seeded HMECs on Detergent Treated Bladder

Detergent treated bladder tissue sections were immunolabeled with integrin β1 because the luminal surface of intact bladders contain a BMC, and integrin β1 is critical to endothelial cell adhesion, migration, and survival (211). Slides for immunolabeling were deparaffinized and rehydrated with decreasing concentration of alcohol and water. Antigen retrieval was performed with Citrate Antigen Retrieval Buffer (10mM, pH6). Retrieval buffer was heated until a boiling

point was reached, slides were immersed, removed from heat, and cooled for 20 min. Slides were washed with 1X PBS 3x for 3 min each. 0.05% Pepsin digest was applied to samples for 15 min minutes in humidity chamber at 37°C. Blocking solution was applied (2% Goat serum, 1% BSA, 0.1% Triton™ X-100, 0.1% Tween) for 1hr at room temp. Slides were washed with 1X PBS as above. Rabbit anti-integrin β1 (Abcam, AB52971, 1:1000) in blocking buffer was applied to each sample. The samples were then incubated at 4°C overnight. Slides were washed with 1X PBS as above. Alexa-Flour 594 goat anti rabbit (invitrogen, 1:200) was applied for 1 hr at room temperature. Slides were washed with 1X PBS as above. Coverslips were added with anti-FADE containing DAPI (Invitrogen, P36931).

4.2.7 Statistical Analysis

A one-way ANOVA was completed for each data set where the independent variable was detergent treatment with significance at $p<0.05$. if significance was found, either a post-hoc Dunnett's test or Tukey's test was completed to determine the specific differences between detergent treatment groups with significance at $p<0.05$. Graph shows mean ± standard error unless otherwise specified.

4.3 RESULTS

4.3.1 Urinary Bladder Analysis

4.3.1.1 SEM of Seeded HMECs

Enface SEM of HMECs cultured on bladders treated with Triton™ X-100 (refer to methods for definition of bladder treated term) showed similar morphology and cell coverage to that of the control. SEM images of seeded bladders treated with sodium deoxycholate showed areas of HMEC coverage as well as exposed ECM. CHAPS and SDS, however, showed greater area of exposed ECM and less HMEC coverage than Triton™ X-100 and sodium deoyxcholate (Figure 32).

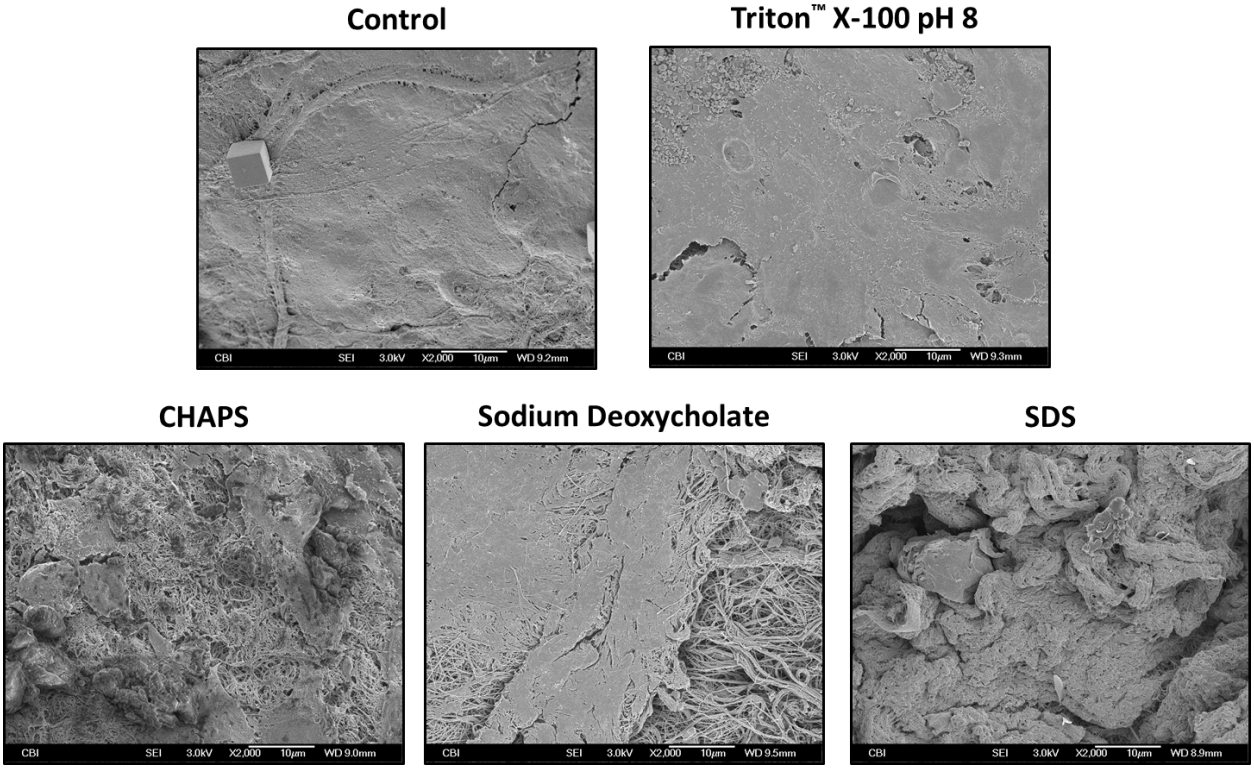

Figure 32: SEM images of HMECs cultured for 7 days on the luminal surface of detergent treated bladder tissue.

4.3.1.2 Semi-Quantitative HMEC Scoring

HMECs cultured on detergent treated bladders that were treated with Triton™ X-100 had a similar level of confluence, a lower infiltration depth, and a similar phenotype compared to cells cultured on the control characterized by a flat morphology (Figure 33). HMECs cultured on the bladders treated with CHAPS were less confluent, had a greater infiltration depth, and an atypical phenotype compared to HMECs cultured on the control. HMECs cultured on bladders treated with sodium deoxycholate were less confluent, had a similar infiltration depth, and an atypical phenotype compared to cells cultured on the control. HMECs cultured on bladders treated with SDS had a similar percentage of confluence, had a similar infiltration depth, but had a less normal phenotype compared to cell cultured on the control.

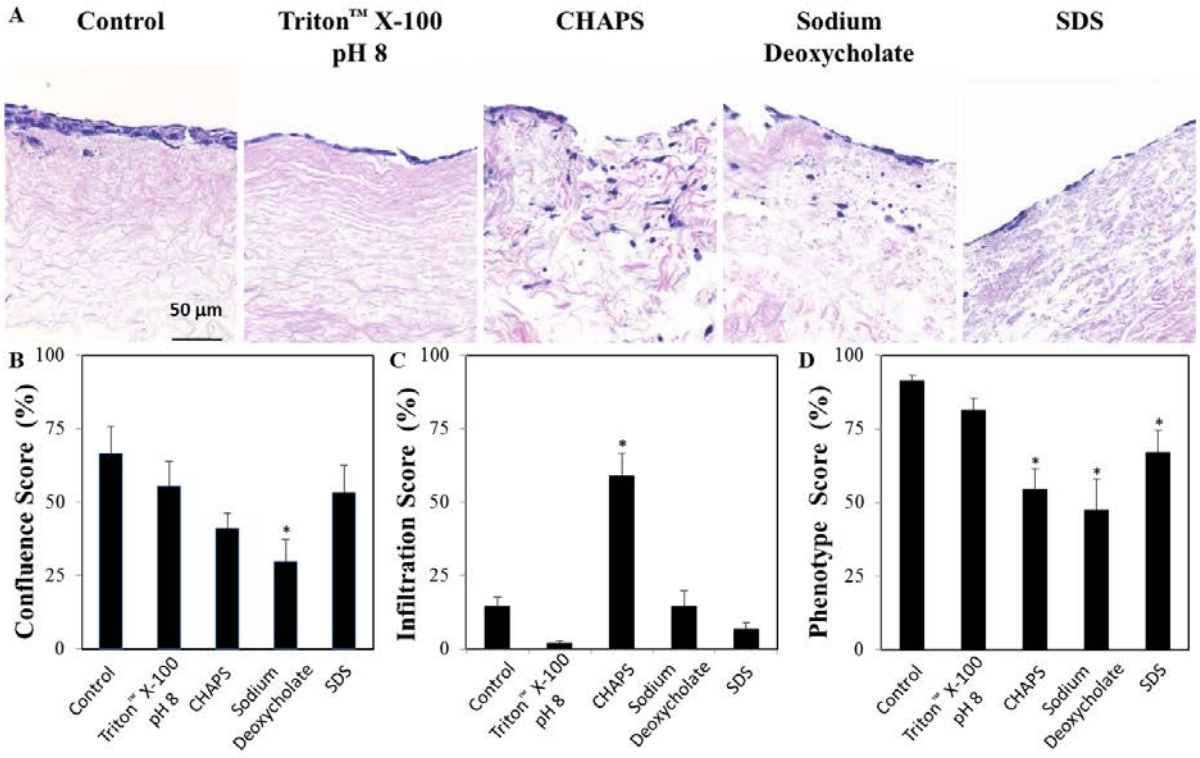

Figure 33: (A) Representative H&E images of HMECs cultured on the luminal surface of detergent treated bladder tissue for 7 days. These images were semi-quantitatively analyzed by five blinded scorers for the level of HMEC (B) confluence, (C) infiltration, and (D) phenotype. Scale bar represents 50 µm. Graph shows mean ± standard error, and * indicates significance at $p<0.05$.

4.3.1.3 Integrin β1 Expression

HMECs cultured on the bladders treated with CHAPS and SDS had a lower number of cells stained positive for integrin β1 compared to HMECs cultured on the control. HMECs cultured on the bladder treated with Triton™ X-100 and sodium deoxycholate had a similar percentage of cells expressing integrin β1 compared to cells cultured on the control (Figure 34).

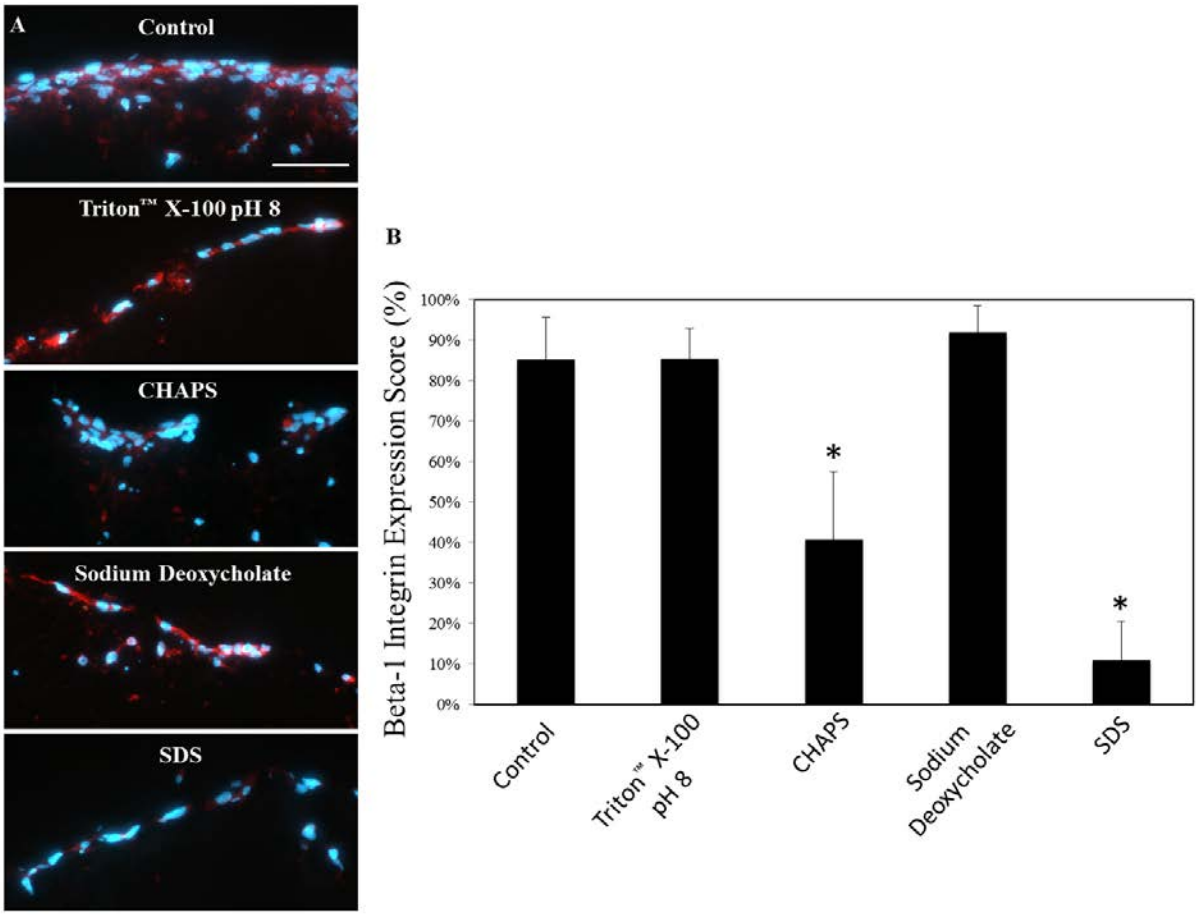

Figure 34: (A) Immunofluorescent images of integrin β1 (red) and DAPI (blue) of HMECs cultured on detergent treated bladder tissue for 7 days. (B) Percentage of cells positive for integrin β1 was determined for each group. Scale bar represents 50 μm. Graph shows mean ± standard error, and * indicates significance at $p<0.05$.

4.3.2 Heart Analysis

4.3.2.1 Seeded HMEC Evaluation

SEM of HMECs cultured on detergent treated hearts had a similar response to that seen in detergent treated bladder (Figure 35). Confirmation through scoring of HE stains (Figure 36 & Figure 37) found that hearts treated with Triton™ X-100 at pH 8 had a confluent layer while

increasing the pH to 11.4 resulted in some areas of exposed ECM. Hearts treated with sodium deoxycholate showed areas of HMEC coverage as well as areas of exposed ECM, and hearts treated with SDS and a multiple step protocol showed large amounts of exposed areas of ECM. While both hearts treated with SDS and a multiple step protocol had large areas of exposed ECM by transverse H&E, examination with enface SEM revealed patches of confluence for hearts treated with the multiple step protocol but not for SDS.

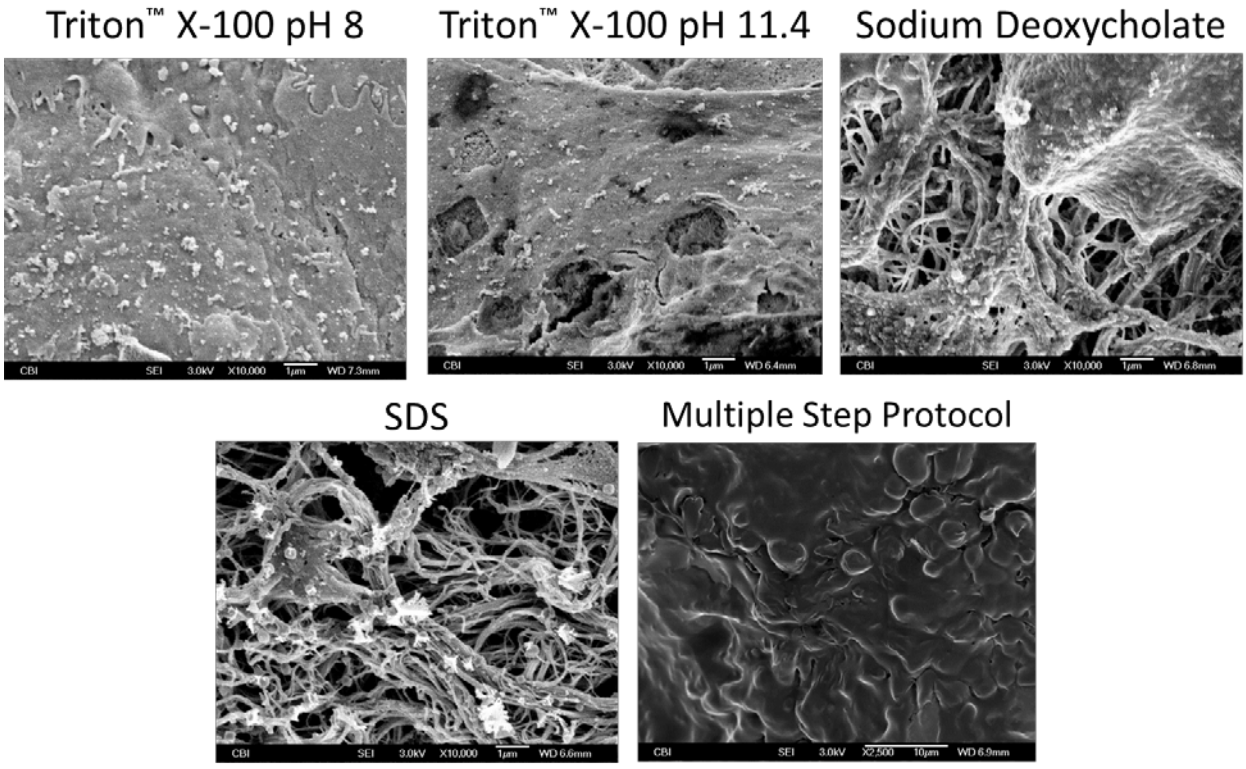

Figure 35: Enface SEM images of HMECs cultured for 7 days on detergent treated heart tissue.

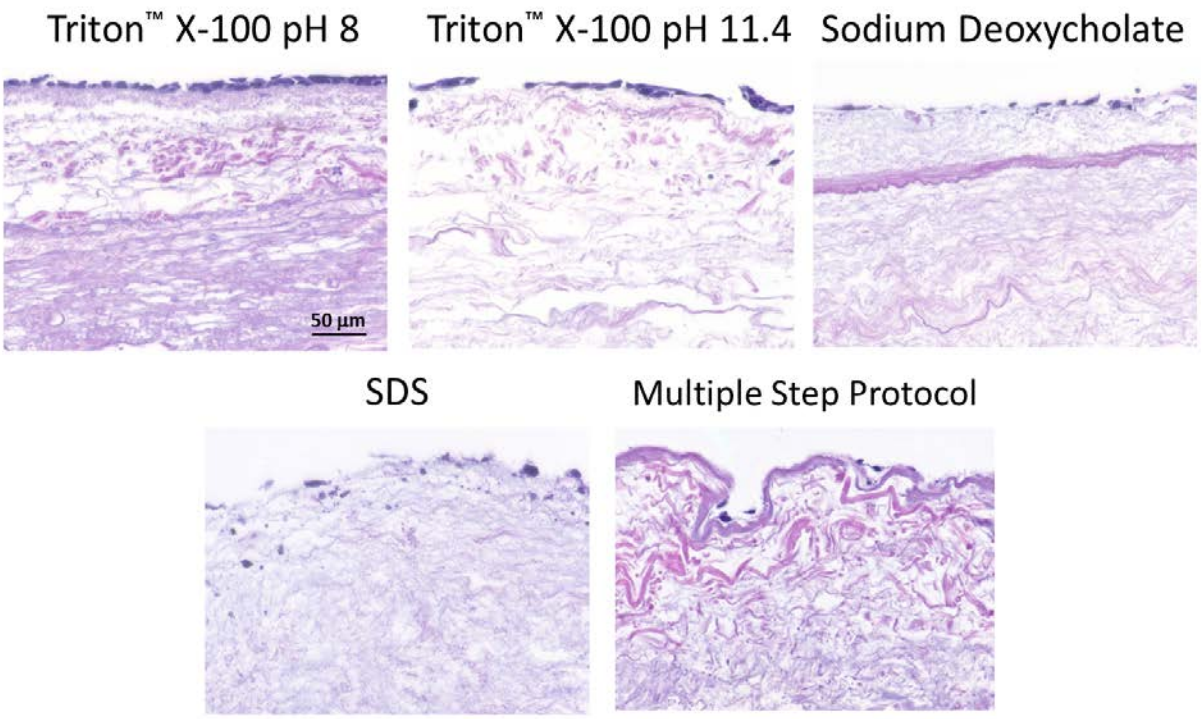

Figure 36: Representative transverse H&E images of HMECs cultured on detergent treated heart tissue for 7 days. Scale bar represents 50 µm.

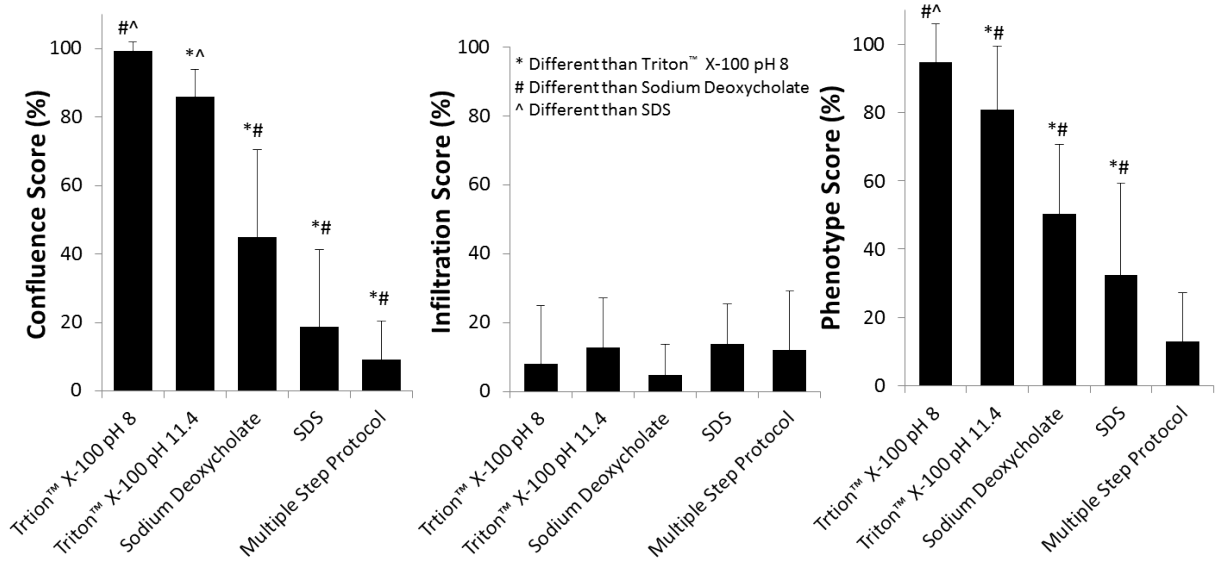

Figure 37: H&E images of detergent treated heart tissue reseeded with HMECs for 7 days were semi-quantitative analyzed by five blinded scorers for HMEC (A) confluence, (B) infiltration, and (C) phenotype. Graph shows mean ± standard error, and * indicates significance at p<0.05.

4.3.2.2 Seeded C2C12 Evaluation

C2C12 culture on detergent treated heart tissue found confluent cell layers on all surfaces from enface SEM (Figure 38), transverse H&E (Figure 39), and scoring of tranverse H&E images (Figure 40). Hearts treated with SDS treatment also had a higher level of cellular infiltration compared to treatment with Triton™ X-100 and sodium deoxycholate indicating disruption of the luminal surface. From enface SEM, the morphology of C2C12 cells was also irregular for hearts treated with SDS.

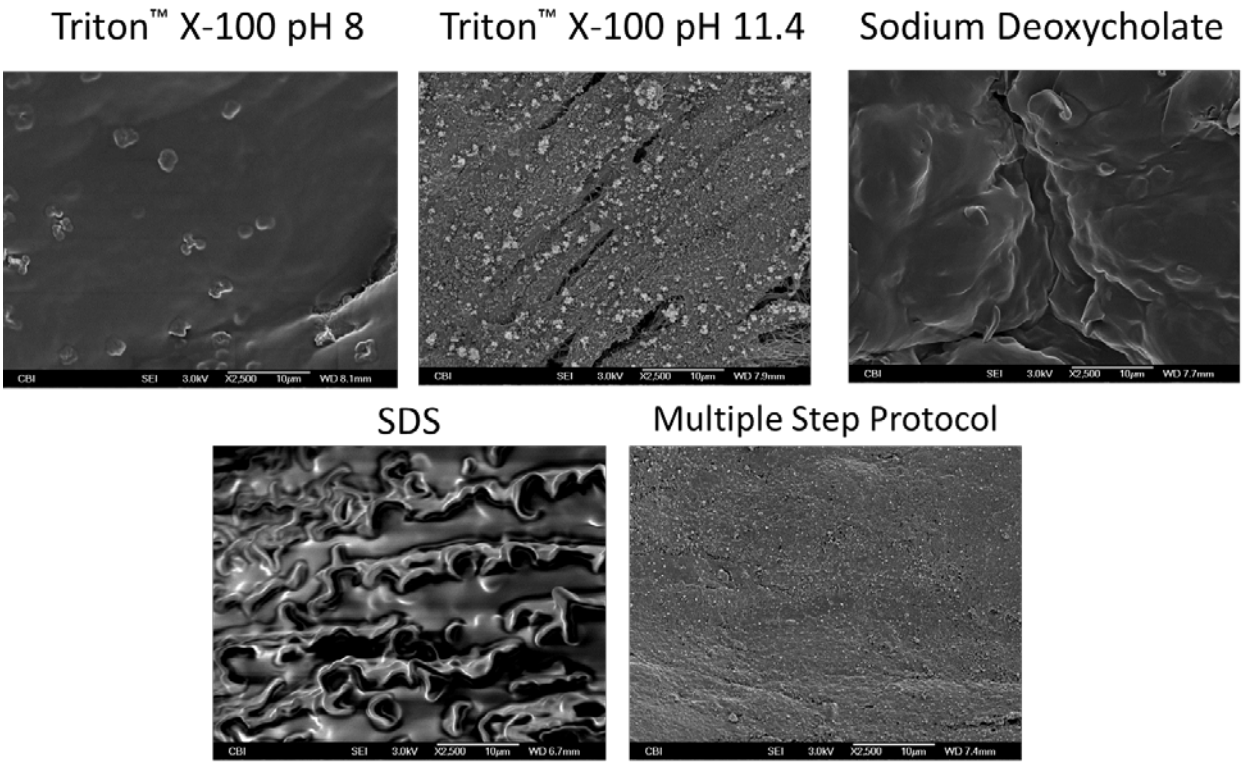

Figure 38: SEM images of C2C12 cultured for 7 days on detergent treated heart tissue.

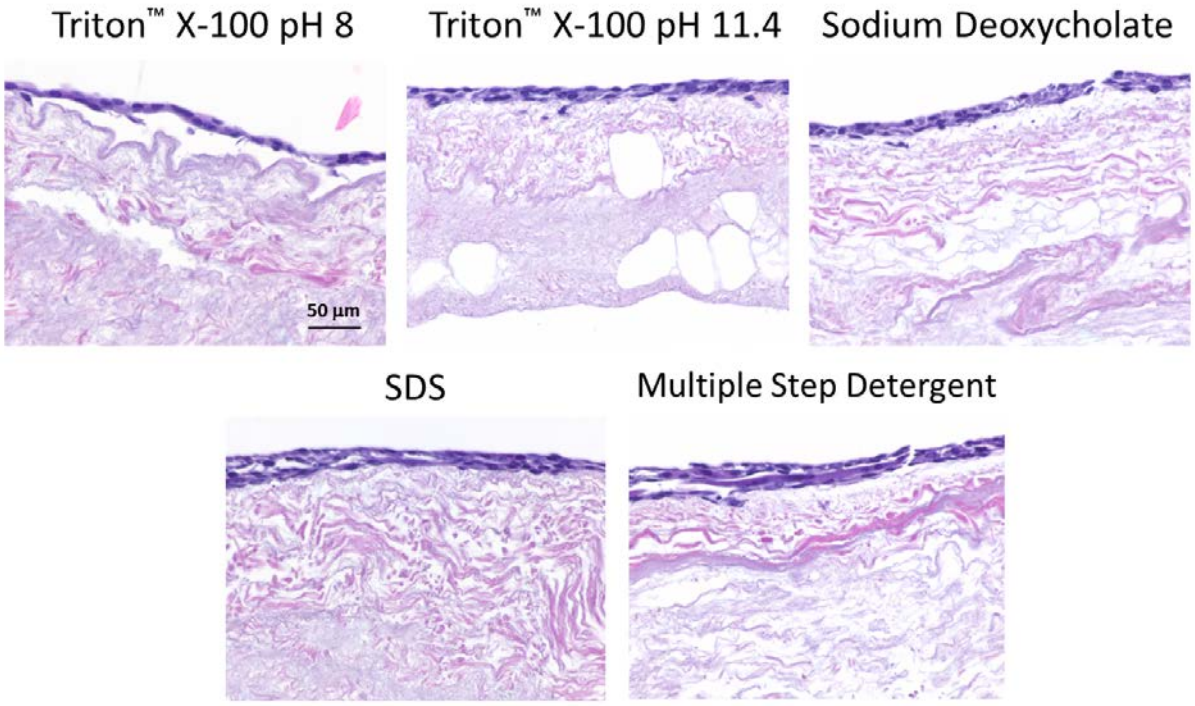

Figure 39: Representative H&E images of C2C12 cultured on detergent treated heart tissue. Scale bar represents 50 µm.

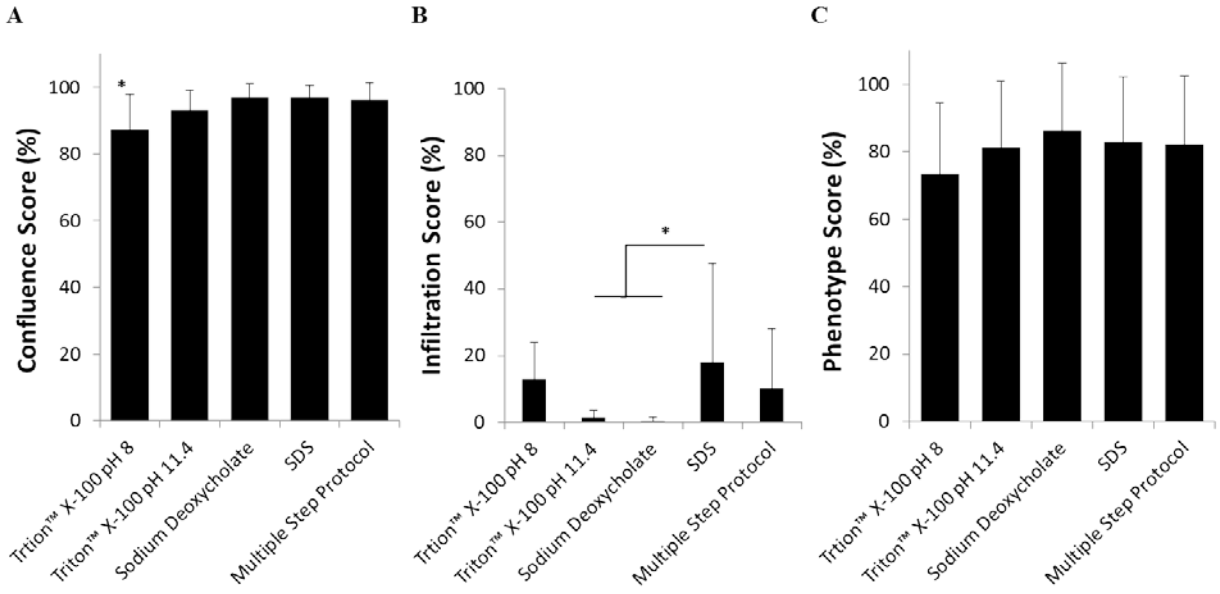

Figure 40: H&E images of detergent treated heart tissue reseeded with C2C12 for 7 days were semi-quantitative analyzed by five blinded scorers for C2C12 (A) confluence, (B) infiltration, and (C) phenotype. Graph shows mean ± standard error, and * indicates significance at $p<0.05$.

4.4 DISCUSSION

A strong relationship that was dependent on the cell type was found to exist between the detergent treatment and cytocompatibility for two source tissues relevant to cardiac repair. Specifically, Triton™ X-100 treatment had a high level of in-vitro HMEC-1 cytocompatibility followed by sodium deoxycholate, whereas CHAPS and SDS treatment had poor cytocompatibility. A multistep protocol combining treatment with Triton™ X-100 and sodium deoxycholate also had a moderate level of in-vitro HMEC-1 cytocompatibility. C2C12 cells were found to be less sensitive to the differences between detergent treated samples. These findings correlated well with the findings from Specific Aim 2 that indicated that the composition and structure of the ECM were best retained through treatment with Triton™ X-100 and sodium deoxycholate, whereas treatment with CHAPS and SDS damaged the fiber network and triggered a loss of ECM constituents. While only two immortalized cell lines were investigated, this finding of a complex relationship between the type of cell and ECM is well known.

The relationship between the cells and ECM is related to cell integrin-ECM ligand interaction. Cellular integrins form adhesions to ECM constituents such as collagen, fibronectin, and laminin through specific ECM domains known as ligands which contain recognizable sequence motifs such as RGD (212, 213). Cellular integrins are heterodimeric transmembrane glycoprotein receptors with a head domain connected to either adjacent cells or these ECM ligands and a cytoplasmic tail domain that is bound to the cytoskeleton-signaling network. Integrins are defined by their non-covalently associated α and β subunits, with most integrins binding to more than one ECM protein, and most ligands recognized by more than one integrin.

This aim examined the β1 subunit for its relevance to the HMEC-1 cell line. β1 integrin was not present when CHAPS or SDS was used. This lack of β1 integrin for CHAPS and SDS

detergent treatment correlated with the damaged composition and structure of the ECM, and the poor cytocompatibility of the ECM. This lack of β1 integrin may be due to the cell's inability to recognize important ECM ligands resulting from damage to the ECM as seen from other criteria in Specific Aim 2. This concept is further supported by the previous finding that investigated the surface of ECM scaffolds which were either prepared from different source tissues or cross-linked, and analyzed by the techniques of SEM and time of flight secondary ion mass spectroscopy. These techniques found differences between the different treatment groups with respect to their ligand landscapes (194).

The finding of a lack of cell-ECM interaction for harsher detergents clearly results in a decreased number of cells remaining on the ECM, but also may affect signal transduction from the ECM to the cell. At these cell-ECM interfaces a focal adhesion complex exists where the integrin is coupled to the internal actin cytoskeleton and cytoplasmic proteins such as paxillin. These cytoplasmic proteins regulate different kinase families such as focal adhesion kinase. These kinase families mediate downstream signaling processing events to regulate cell functions such as migration, proliferation, differentiation, and protein synthesis.

This complex signaling cascade may be activated by a tissue level mechanical stimulus. Specific Aim 1 clearly identified a complex relationship between the ECM fiber network and the cell. This mechanical relationship extends from the size scale of the tissue and cell level down to subcellular mechanisms. Cell integrins act as cellular mechanosensors whereby a local mechanical force may cause a confirmation change in the integrin. This conformation change can activate a focal adhesion kinase. The focal adhesion kinase initiates downstream signaling pathways that affect cellular physiology (214, 215). Thus, this cell integrin – ECM ligand interaction is critical to a healthy cell's function. For example, if an integrin that is associated

with binding to collagen is blocked the cell alignment will actually be lost (151). Cardiomyocytes whose integrin were blocked actually lost proper myofibrillar patterning and alignment (216). This mechanical relationship between the cell and the ECM fiber network, otherwise known as mechanobiology, serves to emphasize the importance of understanding how damage to the ECM scaffold composition and structure as seen in in Specific Aim 2 affects the cell-ECM interaction.

Thus, the findings of Specific Aim 2 and Specific Aim 3 coupled with information on cell integrin – ligand ECM interaction indicate that the composition and structure of an ECM scaffold are critical to cellular function and are closely associated with detergent treatment. The detergent comparisons herein provide a comprehensive database of each detergent to make an educated decision on the balance between decellularization and the retention of the composition, structure, and cytocompatibility of the ECM scaffold. Retention of these variables may prove critical to cellular physiology, and in turn tissue homeostasis and remodeling.

5.0 DISSERTATION SYNOPSIS

5.1 MAJOR FINDINGS

The present work compared the effect of different detergent treatments for tissue and whole organ decellularization on an ECM scaffold's composition, structure, mechanics, and cytocompatibility. This is the first time the three classes of detergents have been comprehensively compared under similar treatment conditions. The major findings for this work are as follows:

Specific Aim 1: To acquire a quantitative understanding of ECM micromechanics.

- An interrelationship exists between ECM composition, ECM structure, cellular gene expression, and cellular deformation as a function of mechanical loading that is highly specific to the anatomic location.
    - At the tissue level, the AV was thicker and had a stiffer mechanical response than the PV under biaxial load possibly due to its inherently higher transvalvular pressure.
    - At the cell level, the PV valvular interstitial cells underwent substantially larger deformations than the AV valvular interstitial cells. These cellular deformations correlated with collagen fiber kinematics and were layer dependent.
    - At the gene level, the AV had a higher level of expression of ECM constituents than the PV.

- Layer dependent cellular-collagen micromechanical coupling exists.
    - At the tissue level, the MV has two opposing fiber networks.
    - At the cell level, valvular interstitial cell deformation was greatest in the layer with the highest density of collagen fibers.

Specific Aim 2: To determine if the structure and mechanics of ECM scaffolds are altered as a function of different detergent treatments.

- Treatment with the zwitterionic detergent CHAPS and the ionic detergent SDS damaged the composition (loss of GAG and elastin) and structure (collagen fiber denaturation) of the source tissue, whereas treatment with the non-ionic detergent Triton™ X-100 and ionic detergent sodium deoxycholate were able to retain this complex composition and structure. However, increasing the pH of Triton™ X-100 from 7.4 to 11 resulted in partial damage to the composition and structure. For the heart, failure strength was unaffected by detergent treatment.
- Treatment with sodium deoxycholate and SDS were effective at removing dsDNA through both tissue mechanical agitation and whole organ perfusion, while treatment with Triton™ X-100 was only able to effectively decellularize thin tissues through mechanical agitation. Increasing the pH of Triton™ X-100 resulted in an increased removal of dsDNA but was still not sufficient to decellularize an entire organ.
- A multiple step protocol with Triton™ X-100 and sodium deoxycholate was able to effectively decellularize an entire organ while retaining its composition and structure.

Specific Aim 3: To determine if cell-ECM interaction is dependent upon the detergent treatment.

- Treatment with Triton™ X-100 resulted in a high level of HMEC-1 in-vitro cytocompatibility followed by sodium deoxycholate, whereas treatment with CHAPS and SDS resulted in a poor level of cytocompatibility. Increasing the pH of Triton™ X-100 from 8 to 11 resulted in decreased HMEC-1 cytocompatibility. C2C12 in-vitro cytocompatibility was insensitive to detergent treatment.
- Treatment with a multiple step protocol combining Triton™ X-100 and sodium deoxycholate also resulted in a high level of HMEC-1 in-vitro cytocompatibility.
- These detergent dependent cytocompatibility findings correlated with the compositional and structural findings from Specific Aim 2 indicating that a complex relationship exists between the cell and the ECM.

5.2 OVERALL CONCLUSIONS

This body of work found that the composition, structure, and cytocompatibility of an ECM scaffold are dependent on the type of detergent selected to achieve decellularization. While this work focused on two source tissues for cardiac repair, the information herein may be extrapolated to different decellularization applications. From these findings, a profile of each detergent was created to assist in the formulation of an optimized decellularization protocol depending on the source tissue of interest.

Table 9: Detergent profile for decellularization. Green, yellow, and red indicate positive, neutral, and negative, respectively.

	Cost	Decellularize	Composition	Structure	Mechanics	Cytocompatibility
Triton™ X-100 pH 8						
Triton™ X-100 pH 11.4						
CHAPS						
Sodium Deoxycholate						
SDS						
Multiple Step Detergent						

For example, based on the findings represented in Table 9 a thin cornea could be decellularized with a non-harsh detergent such as Triton™ X-100 to remove cellular material. However, a dense and thick tissue such as dermis may require a multiple step protocol. From this Table it may be postulated that the tissue should first be treated with a non-harsh detergent such as Triton™ X-100 to remove the majority of cellular material, followed by sodium deoxycholate to remove the remainder. Indeed, in this work a multiple step protocol that serially applies Triton™ X-100 and then sodium deoxycholate (190) was applied to the heart and successfully decellularized the tissue while retaining its composition, structure, and cytocompatibility. If the tissue is still not sufficiently decellularized it may require the application of SDS; however, with the information in Table 9 an investigator should recognize the importance of minimizing the application of such a harsh detergent.

At present, this is not the case. Many investigators utilize SDS for prolonged periods of time ranging from 12 to 120 hours (Table 4, and Table 5). Surprisingly, multiple step protocols

that do not contain SDS are reported to decellularize whole organs in as little as 10 hours with the application of an ionic detergent, sodium deoxycholate, for only three of the hours of treatment (71, 190). Thus, application of many of the protocols reported in Table 4 and Table 5 may have been formulated with the objective only to achieve decellularization due to the prolonged period of treatment with powerful detergents. The work of this dissertation elucidates the need to balance between achieving decellularization and retaining composition, structure, and cytocompatibility. This information will assist both academic laboratories and industry in further optimization of decellularization protocols to create ECM scaffolds with the highest levels of compositional and structural integrity along with excellent cytocompatibility.

5.3 FUTURE WORK

The work presented herein contributes to the foundation of knowledge that may optimize the manufacturing of ECM scaffolds. While other components of the manufacturing process such as source tissue (62, 63), remnant cellular material (104, 105), cross-linking (104), and method of terminal sterilization (43) have been found to impact the host remodeling response it is not clear whether different detergent treatments may have a similar effect. Clearly, from Specific Aim 1 there is an anatomically complex micromechanical relationship between cells and the collagen fiber network of ECM. Damage to this collagen fiber network as seen with harsh detergents in Specific Aim 2 may affect the mechanobiology of the implanted ECM scaffold, subsequently altering the host outcome. Thus, the finding of this body of work that detergents may alter composition, structure, and cytocompatibility of the ECM scaffold indicates that there is a strong possibility that there will be an inherently different host responses as a function of different

detergent treatments. Further in-vivo studies are warranted to identify the level of correlation of host tissue response to detergent treatment. If clear differences exist, an in-vitro mechanistic study should investigate how detergent treatment impacts site-specific tissue repair with primary cell harvests and site-appropriate mechanical loading from protocols developed in Specific Aim 1. This knowledge will lead to the optimization of site-specific ECM scaffold design for the reconstruction of complex tissues and organs.

BIBLIOGRAPHY

1. Go AS, Mozaffarian D, Roger VL, Benjamin EJ, Berry JD, Borden WB, et al. Heart disease and stroke statistics—2013 Update: A report from the American Heart Association. Circulation. 2013;127(1):e6-e245.

2. Miller LW. Left ventricular assist devices are underutilized. Circulation. 2011;123(14):1552-8.

3. Liu SS, Monti J, Kargbo HM, Athar MW, Parakh K. Frontiers of therapy for patients with heart failure. Am J Med. 2013;126(1):6-12.

4. Rose EA, Gelijns AC, Moskowitz AJ, Heitjan DF, Stevenson LW, Dembitsky W, et al. Long-term use of a left ventricular assist device for end-stage heart failure. N Engl J Med. 2001;345(20):1435-43.

5. Kurien S, Hughes KA. Anticoagulation and bleeding in patients with ventricular assist devices: walking the tightrope. AACN Adv Crit Care. 2012;23(1):91-8.

6. Backes D, van den Bergh WM, van Duijn AL, Lahpor JR, van Dijk D, Slooter AJ. Cerebrovascular complications of left ventricular assist devices. Eur J Cardiothorac Surg. 2012;42(4):612-20.

7. Langer R, Vacanti JP. Tissue engineering. Science. 1993;260(5110):920-6.

8. Khademhosseini A, Vacanti JP, Langer R. Progress in tissue engineering. Sci Am. 2009;300(5):64-71.

9. Guan J, Sacks MS, Beckman EJ, Wagner WR. Biodegradable poly(ether ester urethane)urea elastomers based on poly(ether ester) triblock copolymers and putrescine: synthesis, characterization and cytocompatibility. Biomaterials. 2004;25(1):85-96.

10. Anderson JM, Rodriguez A, Chang DT. Foreign body reaction to biomaterials. Semin Immunol. 2008;20(2):86-100.

11. Pascual G, Rodriguez M, Sotomayor S, Perez-Kohler B, Bellon JM. Inflammatory reaction and neotissue maturation in the early host tissue incorporation of polypropylene prostheses. Hernia. 2012;16(6):697-707.

12. Bellon JM, Rodriguez M, Garcia-Honduvilla N, Pascual G, Bujan J. Partially absorbable meshes for hernia repair offer advantages over nonabsorbable meshes. Am J Surg. 2007;194(1):68-74.

13. Schug-Pass C, Tamme C, Sommerer F, Tannapfel A, Lippert H, Kockerling F. A lightweight, partially absorbable mesh (Ultrapro) for endoscopic hernia repair: experimental biocompatibility results obtained with a porcine model. Surg Endosc. 2008;22(4):1100-6.

14. Leber GE, Garb JL, Alexander AI, Reed WP. Long-term complications associated with prosthetic repair of incisional hernias. Arch Surg. 1998;133(4):378-82.

15. Klinge U, Klosterhalfen B, Muller M, Schumpelick V. Foreign body reaction to meshes used for the repair of abdominal wall hernias. Eur J Surg. 1999;165(7):665-73.

16. Badylak SF. Xenogeneic extracellular matrix as a scaffold for tissue reconstruction. Transpl Immunol. 2004;12(3-4):367-77.

17. Chen F, Yoo JJ, Atala A. Acellular collagen matrix as a possible "off the shelf" biomaterial for urethral repair. Urology. 1999;54(3):407-10.

18. Kolker AR, Brown DJ, Redstone JS, Scarpinato VM, Wallack MK. Multilayer reconstruction of abdominal wall defects with acellular dermal allograft (AlloDerm) and component separation. Ann Plast Surg. 2005;55(1):36-41.

19. Lee MS. GraftJacket augmentation of chronic Achilles tendon ruptures. Orthopedics. 2004;27(1 Suppl):s151-3.

20. Metcalf MH, Savoie Iii FH, Kellum B. Surgical technique for xenograft (SIS) augmentation of rotator-cuff repairs. Operative Techniques in Orthopaedics. 2002;12(3):204-8.

21. Wainwright DJ. Use of an acellular allograft dermal matrix (AlloDerm) in the management of full-thickness burns. Burns. 1995;21(4):243-8.

22. Brigido SA. The use of an acellular dermal regenerative tissue matrix in the treatment of lower extremity wounds: a prospective 16-week pilot study. Int Wound J. 2006;3(3):181-7.

23. Barber FA, Herbert MA, Coons DA. Tendon augmentation grafts: biomechanical failure loads and failure patterns. Arthroscopy. 2006;22(5):534-8.

24. Atala A, Bauer SB, Soker S, Yoo JJ, Retik AB. Tissue-engineered autologous bladders for patients needing cystoplasty. Lancet. 2006;367(9518):1241-6.

25. Catena F, Ansaloni L, Leone A, De Cataldis A, Gagliardi S, Gazzotti F, et al. Lichtenstein repair of inguinal hernia with Surgisis inguinal hernia matrix soft-tissue graft in immunodepressed patients. Hernia. 2005;9(1):29-31.

26. Ueno T, Pickett LC, de la Fuente SG, Lawson DC, Pappas TN. Clinical application of porcine small intestinal submucosa in the management of infected or potentially contaminated abdominal defects. J Gastrointest Surg. 2004;8(1):109-12.

27. Butler CE, Prieto VG. Reduction of adhesions with composite AlloDerm/polypropylene mesh implants for abdominal wall reconstruction. Plast Reconstr Surg. 2004;114(2):464-73.

28. Sclafani AP, Romo T, 3rd, Jacono AA, McCormick S, Cocker R, Parker A. Evaluation of acellular dermal graft in sheet (AlloDerm) and injectable (micronized AlloDerm) forms for soft tissue augmentation. Clinical observations and histological analysis. Arch Facial Plast Surg. 2000;2(2):130-6.

29. Bissell MJ, Aggeler J. Dynamic reciprocity: how do extracellular matrix and hormones direct gene expression? Prog Clin Biol Res. 1987;249:251-62.

30. Kleinman HK, Philp D, Hoffman MP. Role of the extracellular matrix in morphogenesis. Curr Opin Biotechnol. 2003;14(5):526-32.

31. Cooper DK, Good AH, Koren E, Oriol R, Malcolm AJ, Ippolito RM, et al. Identification of alpha-galactosyl and other carbohydrate epitopes that are bound by human anti-pig antibodies: relevance to discordant xenografting in man. Transpl Immunol. 1993;1(3):198-205.

32. Bernard MP, Myers JC, Chu ML, Ramirez F, Eikenberry EF, Prockop DJ. Structure of a cDNA for the pro alpha 2 chain of human type I procollagen. Comparison with chick cDNA for pro alpha 2(I) identifies structurally conserved features of the protein and the gene. Biochemistry. 1983;22(5):1139-45.

33. Bernard MP, Chu ML, Myers JC, Ramirez F, Eikenberry EF, Prockop DJ. Nucleotide sequences of complementary deoxyribonucleic acids for the pro alpha 1 chain of human type I procollagen. Statistical evaluation of structures that are conserved during evolution. Biochemistry. 1983;22(22):5213-23.

34. Exposito JY, D'Alessio M, Solursh M, Ramirez F. Sea urchin collagen evolutionarily homologous to vertebrate pro-alpha 2(I) collagen. J Biol Chem. 1992;267(22):15559-62.

35. Allman AJ, McPherson TB, Badylak SF, Merrill LC, Kallakury B, Sheehan C, et al. Xenogeneic extracellular matrix grafts elicit a TH2-restricted immune response. Transplantation. 2001;71(11):1631-40.

36. Vorotnikova E, McIntosh D, Dewilde A, Zhang J, Reing JE, Zhang L, et al. Extracellular matrix-derived products modulate endothelial and progenitor cell migration and proliferation in vitro and stimulate regenerative healing in vivo. Matrix Biol. 2010;29(8):690-700.

37. Barkan D, Green JE, Chambers AF. Extracellular matrix: a gatekeeper in the transition from dormancy to metastatic growth. Eur J Cancer. 2010;46(7):1181-8.

38. Nelson CM, Bissell MJ. Of extracellular matrix, scaffolds, and signaling: tissue architecture regulates development, homeostasis, and cancer. Annu Rev Cell Dev Biol. 2006;22:287-309.

39. Taylor KR, Gallo RL. Glycosaminoglycans and their proteoglycans: host-associated molecular patterns for initiation and modulation of inflammation. Faseb J. 2006;20(1):9-22.

40. Nagase H, Visse R, Murphy G. Structure and function of matrix metalloproteinases and TIMPs. Cardiovasc Res. 2006;69(3):562-73.

41. Werner S, Grose R. Regulation of wound healing by growth factors and cytokines. Physiol Rev. 2003;83(3):835-70.

42. Bornstein P, Sage EH. Matricellular proteins: extracellular modulators of cell function. Curr Opin Cell Biol. 2002;14(5):608-16.

43. Valentin JE, Badylak JS, McCabe GP, Badylak SF. Extracellular matrix bioscaffolds for orthopaedic applications. A comparative histologic study. J Bone Joint Surg Am. 2006;88(12):2673-86.

44. Badylak SF, Valentin JE, Ravindra AK, McCabe GP, Stewart-Akers AM. Macrophage phenotype as a determinant of biologic scaffold remodeling. Tissue Eng Part A. 2008;14(11):1835-42.

45. Gilbert TW, Stewart-Akers AM, Sydeski J, Nguyen TD, Badylak SF, Woo SL. Gene expression by fibroblasts seeded on small intestinal submucosa and subjected to cyclic stretching. Tissue Eng. 2007;13(6):1313-23.

46. Androjna C, Spragg RK, Derwin KA. Mechanical conditioning of cell-seeded small intestine submucosa: a potential tissue-engineering strategy for tendon repair. Tissue Eng. 2007;13(2):233-43.

47. Record RD, Hillegonds D, Simmons C, Tullius R, Rickey FA, Elmore D, et al. In vivo degradation of 14C-labeled small intestinal submucosa (SIS) when used for urinary bladder repair. Biomaterials. 2001;22(19):2653-9.

48. Gilbert TW, Stewart-Akers AM, Simmons-Byrd A, Badylak SF. Degradation and remodeling of small intestinal submucosa in canine Achilles tendon repair. J Bone Joint Surg Am. 2007;89(3):621-30.

49. Agrawal V, Kelly J, Tottey S, Daly KA, Johnson SA, Siu BF, et al. An isolated cryptic peptide influences osteogenesis and bone remodeling in an adult mammalian model of digit amputation. Tissue Eng Part A. 2011;17(23-24):3033-44.

50. Badylak SF, Park K, Peppas N, McCabe G, Yoder M. Marrow-derived cells populate scaffolds composed of xenogeneic extracellular matrix. Exp Hematol. 2001;29(11):1310-8.

51. Agrawal V, Tottey S, Johnson SA, Freund JM, Siu BF, Badylak SF. Recruitment of progenitor cells by an extracellular matrix cryptic peptide in a mouse model of digit amputation. Tissue Eng Part A. 2011;17(19-20):2435-43.

52. Badylak SF, Lantz GC, Coffey A, Geddes LA. Small intestinal submucosa as a large diameter vascular graft in the dog. J Surg Res. 1989;47(1):74-80.

53. Badylak SF, Tullius R, Kokini K, Shelbourne KD, Klootwyk T, Voytik SL, et al. The use of xenogeneic small intestinal submucosa as a biomaterial for Achilles tendon repair in a dog model. J Biomed Mater Res. 1995;29(8):977-85.

54. Chen RN, Ho HO, Tsai YT, Sheu MT. Process development of an acellular dermal matrix (ADM) for biomedical applications. Biomaterials. 2004;25(13):2679-86.

55. Grauss RW, Hazekamp MG, Oppenhuizen F, van Munsteren CJ, Gittenberger-de Groot AC, DeRuiter MC. Histological evaluation of decellularised porcine aortic valves: matrix changes due to different decellularisation methods. Eur J Cardiothorac Surg. 2005;27(4):566-71.

56. Rieder E, Kasimir MT, Silberhumer G, Seebacher G, Wolner E, Simon P, et al. Decellularization protocols of porcine heart valves differ importantly in efficiency of cell removal and susceptibility of the matrix to recellularization with human vascular cells. J Thorac Cardiovasc Surg. 2004;127(2):399-405.

57. Medberry CJ, Crapo PM, Siu BF, Carruthers CA, Wolf MT, Nagarkar SP, et al. Hydrogels derived from central nervous system extracellular matrix. Biomaterials. 2013;34(4):1033-40.

58. Soto-Gutierrez A, Zhang L, Medberry C, Fukumitsu K, Faulk D, Jiang H, et al. A whole-organ regenerative medicine approach for liver replacement. Tissue Eng Part C Methods. 2011;17(6):677-86.

59. Wainwright JM, Hashizume R, Fujimoto KL, Remlinger NT, Pesyna C, Wagner WR, et al. Right ventricular outflow tract repair with a cardiac biologic scaffold. Cells Tissues Organs. 2012;195(1-2):159-70.

60. Singelyn JM, DeQuach JA, Seif-Naraghi SB, Littlefield RB, Schup-Magoffin PJ, Christman KL. Naturally derived myocardial matrix as an injectable scaffold for cardiac tissue engineering. Biomaterials. 2009;30(29):5409-16.

61. Badylak SF, Taylor D, Uygun K. Whole-organ tissue engineering: Decellularization and recellularization of three-dimensional matrix scaffolds. Annual Review of Biomedical Engineering. 2011;13(1):27-53.

62. Lin P, Chan WCW, Badylak SF, Bhatia SN. Assessing porcine liver-derived biomatrix for hepatic tissue engineering. Tissue Eng. 2004;10(7-8):1046-53.

63. Sellaro TL, Ravindra AK, Stolz DB, Badylak SF. Maintenance of hepatic sinusoidal endothelial cell phenotype in vitro using organ-specific extracellular matrix scaffolds. Tissue Eng. 2007;13(9):2301-10.

64. Uygun BE, Soto-Gutierrez A, Yagi H, Izamis ML, Guzzardi MA, Shulman C, et al. Organ reengineering through development of a transplantable recellularized liver graft using decellularized liver matrix. Nat Med. 2010;16(7):814-20.

65. Ott HC, Matthiesen TS, Goh S-K, Black LD, Kren SM, Netoff TI, et al. Perfusion-decellularized matrix: using nature's platform to engineer a bioartificial heart. Nat Med. 2008;14(2):213-21.

66. Singelyn J, Christman K. Injectable materials for the treatment of myocardial infarction and heart failure: The promise of decellularized matrices. Journal of Cardiovascular Translational Research. 2010;3(5):478-86.

67. Petersen TH, Calle EA, Zhao L, Lee EJ, Gui L, Raredon MB, et al. Tissue-engineered lungs for in vivo implantation. Science. 2010;329(5991):538-41.

68. Remlinger NT, Czajka CA, Juhas ME, Vorp DA, Stolz DB, Badylak SF, et al. Hydrated xenogeneic decellularized tracheal matrix as a scaffold for tracheal reconstruction. Biomaterials. 2010;31(13):3520-6.

69. Karabekmez FE, Duymaz A, Moran SL. Early clinical outcomes with the use of decellularized nerve allograft for repair of sensory defects within the hand. Hand. 2009;4(3):245-9.

70. Yu C, Bianco J, Brown C, Fuetterer L, Watkins JF, Samani A, et al. Porous decellularized adipose tissue foams for soft tissue regeneration. Biomaterials. 2013;34(13):3290-302.

71. Wainwright JM, Czajka CA, Patel UB, Freytes DO, Tobita K, Gilbert TW, et al. Preparation of cardiac extracellular matrix from an intact porcine heart. Tissue Eng Part C Methods. 2010;16(3):525-32.

72. Weymann A, Loganathan S, Takahashi H, Schies C, Claus B, Hirschberg K, et al. Development and evaluation of a perfusion decellularization porcine heart model - generation of 3-dimensional myocardial neoscaffolds. Circulation Journal. 2011;75(4):852-60.

73. Cortiella J, Niles J, Cantu A, Brettler A, Pham A, Vargas G, et al. Influence of acellular natural lung matrix on murine embryonic stem cell differentiation and tissue formation. Tissue Eng Part A. 2010;16(8):2565-80.

74. Song JJ, Guyette JP, Gilpin SE, Gonzalez G, Vacanti JP, Ott HC. Regeneration and experimental orthotopic transplantation of a bioengineered kidney. Nat Med. 2013;19(5):646-51.

75. Weisman HF, Healy B. Myocardial infarct expansion, infarct extension, and reinfarction: pathophysiologic concepts. Prog Cardiovasc Dis. 1987;30(2):73-110.

76. Jackson BM, Gorman JH, Moainie SL, Guy TS, Narula N, Narula J, et al. Extension of borderzone myocardium in postinfarction dilated cardiomyopathy. J Am Coll Cardiol. 2002;40(6):1160-7.

77. Mann DL, Bristow MR. Mechanisms and models in heart failure: the biomechanical model and beyond. Circulation. 2005;111(21):2837-49.

78. Holmes JW, Borg TK, Covell JW. Structure and mechanics of healing myocardial infarcts. Annual Review of Biomedical Engineering. 2005;7:223-53.

79. White HD, Norris RM, Brown MA, Brandt PW, Whitlock RM, Wild CJ. Left ventricular end-systolic volume as the major determinant of survival after recovery from myocardial infarction. Circulation. 1987;76(1):44-51.

80. Sabbah HN, Shimoyama H, Kono T, Gupta RC, Sharov VG, Scicli G, et al. Effects of long-term monotherapy with enalapril, metoprolol, and digoxin on the progression of left ventricular dysfunction and dilation in dogs with reduced ejection fraction. Circulation. 1994;89(6):2852-9.

81. Dor V, Montiglio F, Sabatier M, Coste P, Barletta G, Di Donato M, et al. Left ventricular shape changes induced by aneurysmectomy with endoventricular circular patch plasty reconstruction. Eur Heart J. 1994;15(8):1063-9.

82. Dor V, Sabatier M, Di Donato M, Montiglio F, Toso A, Maioli M. Efficacy of endoventricular patch plasty in large postinfarction akinetic scar and severe left ventricular dysfunction: comparison with a series of large dyskinetic scars. J Thorac Cardiovasc Surg. 1998;116(1):50-9.

83. Magovern JA. Experimental and clinical studies with the Paracor cardiac restraint device. Semin Thorac Cardiovasc Surg. 2005;17(4):364-8.

84. Mann DL, Kubo SH, Sabbah HN, Starling RC, Jessup M, Oh JK, et al. Beneficial effects of the CorCap cardiac support device: five-year results from the Acorn Trial. J Thorac Cardiovasc Surg. 2012;143(5):1036-42.

85. Fujimoto KL, Tobita K, Merryman WD, Guan J, Momoi N, Stolz DB, et al. An elastic, biodegradable cardiac patch induces contractile smooth muscle and improves cardiac remodeling and function in subacute myocardial infarction. J Am Coll Cardiol. 2007;49(23):2292-300.

86. Fujimoto KL, Tobita K, Guan J, Hashizume R, Takanari K, Alfieri CM, et al. Placement of an elastic biodegradable cardiac patch on a subacute infarcted heart leads to cellularization with early developmental cardiomyocyte characteristics. J Card Fail. 2012;18(7):585-95.

87. Wainwright JM. Right ventricular outflow tract repair with a cardiac biologic scaffold. Cells Tissues Organs. 2011;15219:1-12.

88. Robinson KA, Li J, Mathison M, Redkar A, Cui J, Chronos NA, et al. Extracellular matrix scaffold for cardiac repair. Circulation. 2005;112(9 Suppl):I135-43.

89. Badylak SF, Kochupura PV, Cohen IS, Doronin SV, Saltman AE, Gilbert TW, et al. The use of extracellular matrix as an inductive scaffold for the partial replacement of functional myocardium. Cell Transplant. 2006;15(1):S29-40.

90. Remlinger NT, Gilbert TW, Yoshida M, Guest BN, Hashizume R, Weaver ML, et al. Urinary bladder matrix promotes site appropriate tissue formation following right ventricle outflow tract repair. Organogenesis. 2013;9:3.

91. Freytes DO, Martin J, Velankar SS, Lee AS, Badylak SF. Preparation and rheological characterization of a gel form of the porcine urinary bladder matrix. Biomaterials. 2008;29(11):1630-7.

92. Cowin SC, Doty SB. Tissue mechanics: Springer; 2007.

93. Lodish H. Molecular cell biology. New York: W. H. Freeman; 2008.

94. Helm P, Beg MF, Miller MI, Winslow RL. Measuring and mapping cardiac fiber and laminar architecture using diffusion tensor MR imaging. Ann N Y Acad Sci. 2005:296-307.

95. Sacks MS, Sun W. Multiaxial mechanical behavior of biological materials. Annual Review of Biomedical Engineering. 2003;5:251-84.

96. Baicu CF, Stroud JD, Livesay VA, Hapke E, Holder J, Spinale FG, et al. Changes in extracellular collagen matrix alter myocardial systolic performance. Am J Physiol Heart Circ Physiol. 2003;284(1):H122-32.

97. Ezzell RM, Goldmann WH, Wang N, Parashurama N, Ingber DE. Vinculin promotes cell spreading by mechanically coupling integrins to the cytoskeleton. Exp Cell Res. 1997;231(1):14-26.

98. Brancaccio M, Fratta L, Notte A, Hirsch E, Poulet R, Guazzone S, et al. Melusin, a muscle-specific integrin beta1-interacting protein, is required to prevent cardiac failure in response to chronic pressure overload. Nat Med. 2003;9(1):68-75.

99. Parker KK, Ingber DE. Extracellular matrix, mechanotransduction and structural hierarchies in heart tissue engineering. Philos Trans R Soc Lond B Biol Sci. 2007;362(1484):1267-79.

100. Crapo PM, Gilbert TW, Badylak SF. An overview of tissue and whole organ decellularization processes. Biomaterials. 2011;32(12):3233-43.

101. Cox B, Emili A. Tissue subcellular fractionation and protein extraction for use in mass-spectrometry-based proteomics. Nat Protoc. 2006;1(4):1872-8.

102. Freytes DO, Badylak SF, Webster TJ, Geddes LA, Rundell AE. Biaxial strength of multilaminated extracellular matrix scaffolds. Biomaterials. 2004;25(12):2353-61.

103. Sarig U, Au-Yeung GC, Wang Y, Bronshtein T, Dahan N, Boey FY, et al. Thick acellular heart extracellular matrix with inherent vasculature: a potential platform for myocardial tissue regeneration. Tissue Eng Part A. 2012;18(19-20):2125-37.

104. Brown BN, Valentin JE, Stewart-Akers AM, McCabe GP, Badylak SF. Macrophage phenotype and remodeling outcomes in response to biologic scaffolds with and without a cellular component. Biomaterials. 2009;30(8):1482-91.

105. Keane TJ, Londono R, Turner NJ, Badylak SF. Consequences of ineffective decellularization of biologic scaffolds on the host response. Biomaterials. 2012;33(6):1771-81.

106. Reing JE, Brown BN, Daly KA, Freund JM, Gilbert TW, Hsiong SX, et al. The effects of processing methods upon mechanical and biologic properties of porcine dermal extracellular matrix scaffolds. Biomaterials. 2010;31(33):8626-33.

107. Shafiq MA, Gemeinhart RA, Yue BY, Djalilian AR. Decellularized human cornea for reconstructing the corneal epithelium and anterior stroma. Tissue Eng Part C Methods. 2012;18(5):340-8.

108. Du L, Wu X, Pang K, Yang Y. Histological evaluation and biomechanical characterisation of an acellular porcine cornea scaffold. Br J Ophthalmol. 2011;95(3):410-4.

109. Wallis JM, Borg ZD, Daly AB, Deng B, Ballif BA, Allen GB, et al. Comparative assessment of detergent-based protocols for mouse lung de-cellularization and re-cellularization. Tissue Eng Part C Methods. 2012;18(6):420-32.

110. Meyer SR, Chiu B, Churchill TA, Zhu L, Lakey JR, Ross DB. Comparison of aortic valve allograft decellularization techniques in the rat. J Biomed Mater Res A. 2006;79(2):254-62.

111. Pagoulatou E, Triantaphyllidou IE, Vynios DH, Papachristou DJ, Koletsis E, Deligianni D, et al. Biomechanical and structural changes following the decellularization of bovine pericardial tissues for use as a tissue engineering scaffold. J Mater Sci Mater Med. 2012;23(6):1387-96.

112. Mendoza-Novelo B, Avila EE, Cauich-Rodriguez JV, Jorge-Herrero E, Rojo FJ, Guinea GV, et al. Decellularization of pericardial tissue and its impact on tensile viscoelasticity and glycosaminoglycan content. Acta Biomater. 2011;7(3):1241-8.

113. Akhyari P, Aubin H, Gwanmesia P, Barth M, Hoffmann S, Huelsmann J, et al. The quest for an optimized protocol for whole-heart decellularization: A comparison of three popular and a novel decellularization technique and their diverse effects on crucial extracellular matrix qualities. Tissue Engineering Part C: Methods. 2011;17(9):915-26.

114. Arnold T, Linke D. The use of detergents to purify membrane proteins. Curr Protoc Protein Sci. 2008;4(4):1-4.

115. Seddon AM, Curnow P, Booth PJ. Membrane proteins, lipids and detergents: not just a soap opera. Biochim Biophys Acta. 2004;3:1-2.

116. Prive GG. Detergents for the stabilization and crystallization of membrane proteins. Methods. 2007;41(4):388-97.

117. Hodde JP, Badylak SF, D. SK. The effect of range of motion on remodeling of small intestinal submucosa (SIS) When used as an achilles tendon repair material in the rabbit. Tissue Engineering. 1997;3(1):27-37.

118. Boruch AV, Nieponice A, Qureshi IR, Gilbert TW, Badylak SF. Constructive remodeling of biologic scaffolds is dependent on early exposure to physiologic bladder filling in a canine partial cystectomy model. J Surg Res. 2010;161(2):217-25.

119. Nguyen TD, Liang R, Woo SL, Burton SD, Wu C, Almarza A, et al. Effects of cell seeding and cyclic stretch on the fiber remodeling in an extracellular matrix-derived bioscaffold. Tissue Eng Part A. 2009;15(4):957-63.

120. Sacks MS, David Merryman W, Schmidt DE. On the biomechanics of heart valve function. J Biomech. 2009;42(12):1804-24.

121. Aikawa E, Whittaker P, Farber M, Mendelson K, Padera RF, Aikawa M, et al. Human semilunar cardiac valve remodeling by activated cells from fetus to adult: implications for postnatal adaptation, pathology, and tissue engineering. Circulation. 2006;113(10):1344-52.

122. Joyce EM, Liao J, Schoen FJ, Mayer JE, Jr., Sacks MS. Functional collagen fiber architecture of the pulmonary heart valve cusp. Ann Thorac Surg. 2009;87(4):1240-9.

123. Christie GW, Barratt-Boyes BG. Mechanical properties of porcine pulmonary valve leaflets: how do they differ from aortic leaflets? Ann Thorac Surg. 1995;60(2 Suppl):S195-9.

124. Hoffman BD, Crocker JC. Cell mechanics: dissecting the physical responses of cells to force. Annual Review of Biomedical Engineering. 2009;11:259-88.

125. Mirnajafi A, Raymer JM, McClure LR, Sacks MS. The flexural rigidity of the aortic valve leaflet in the commissural region. J Biomech. 2006;39(16):2966-73.

126. Stella JA, Sacks MS. On the biaxial mechanical properties of the layers of the aortic valve leaflet. J Biomech Eng. 2007;129(5):757-66.

127. Kadner A, Raisky O, Degandt A, Tamisier D, Bonnet D, Sidi D, et al. The ross procedure in infants and young children. Ann Thorac Surg. 2008;85(3):803-8.

128. Rabkin-Aikawa E, Aikawa M, Farber M, Kratz JR, Garcia-Cardena G, Kouchoukos NT, et al. Clinical pulmonary autograft valves: pathologic evidence of adaptive remodeling in the aortic site. J Thorac Cardiovasc Surg. 2004;128(4):552-61.

129. Taylor PM, Batten P, Brand NJ, Thomas PS, Yacoub MH. The cardiac valve interstitial cell. International Journal of Biochemistry and Cell Biology. 2003;35(2):113-8.

130. Rabkin-Aikawa E, Farber M, Aikawa M, Schoen FJ. Dynamic and reversible changes of interstitial cell phenotype during remodeling of cardiac valves. J Heart Valve Dis. 2004;13(5):841-7.

131. Ikhumetse J, Konduri S, Warnok J, Xing Y, Yoganathan A. Cyclic aortic pressure affects the biological properties of porcine pulmonary valve leaflets. Journal of Heart Valve Disease. 2006;15:295-302.

132. Merryman WD, Lukoff HD, Long RA, Engelmayr GC, Jr., Hopkins RA, Sacks MS. Synergistic effects of cyclic tension and transforming growth factor-beta1 on the aortic valve myofibroblast. Cardiovasc Pathol. 2007;16(5):268-76.

133. Huang HY, Liao J, Sacks MS. In-situ deformation of the aortic valve interstitial cell nucleus under diastolic loading. J Biomech Eng. 2007;129(6):880-89.

134. Hinton RB, Jr, Lincoln J, Deutsch GH, Osinska H, Manning PB, Benson DW, et al. Extracellular matrix remodeling and organization in developing and diseased aortic valves. Circ Res. 2006;98(11):1431-8.

135. Lincoln J, Alfieri CM, Yutzey KE. Development of heart valve leaflets and supporting apparatus in chicken and mouse embryos. Developmental Dynamics. 2004;230(2):239-50.

136. Chakraborty S, Cheek J, Sakthivel B, Aronow BJ, Yutzey KE. Shared gene expression profiles in developing heart valves and osteoblast progenitor cells. Physiol Genomics. 2008;35(1):75-85.

137. Woo SLY, Orlando CA, Camp JF, Akeson WH. Effects of postmortem storage by freezing on ligament tensile behavior. Journal of Biomechanics. 1994;19:399-404.

138. Billiar KL, Sacks MS. Biaxial mechanical properties of the natural and glutaraldehyde treated aortic valve cusp--Part I: Experimental results. J Biomech Eng. 2000;122(1):23-30.

139. Christie GW. Anatomy of aortic heart valve leaflets: the influence of glutaraldehyde fixation on function. European Journal of Cardio-Thoracic Surgery. 1992;6:S25-S33.

140. Watkins S. Immunohistochemistry. Current Protocols in Cytometry: John Wiley & Sons, Inc.; 2001.

141. Stella JA, Liao J, Hong Y, David Merryman W, Wagner WR, Sacks MS. Tissue-to-cellular level deformation coupling in cell micro-integrated elastomeric scaffolds. Biomaterials. 2008;29(22):3228-36.

142. Stephens E, Grande-Allen K. Age-related changes in collagen synthesis and turnover in porcine heart valves. J Heart Valve Dis. 2007;16(6):672-82.

143. Latif N, Sarathchandra P, Taylor PM, Antoniw J, Yacoub MH. Localization and pattern of expression of extracellular matrix components in human heart valves. J Heart Valve Dis. 2005;14(2):218-27.

144. Bouchard-Martel J, Roussel E, Drolet M, Arsenault M, Couet J. Interstitial cells from left-sided heart valves display more calcification potential than from right-sided valves: an in-vitro study of porcine valves. J Heart Valve Dis. 2009;18(4):421-8.

145. Snider P, Hinton RB, Moreno-Rodriguez RA, Wang J, Rogers R, Lindsley A, et al. Periostin Is required for maturation and extracellular matrix stabilization of noncardiomyocyte lineages of the heart. Circ Res. 2008;102(7):752-60.

146. Merryman WD, Youn I, Lukoff HD, Krueger PM, Guilak F, Hopkins RA, et al. Correlation between heart valve interstitial cell stiffness and transvalvular pressure: implications for collagen biosynthesis. Am J Physiol Heart Circ Physiol. 2006;290(1):H224-31.

147. Aldous IG, Veres SP, Jahangir A, Lee JM. Differences in collagen cross-linking between the four valves of the bovine heart: a possible role in adaptation to mechanical fatigue. Am J Physiol Heart Circ Physiol. 2009;296(6):H1898-906.

148. Aldous I, Lee J, Wells S. Differential changes in the molecular stability of collagen from the pulmonary and aortic valves during the fetal-to-neonatal transition. Annals of Biomedical Engineering. 2010;38(9):3000-9.

149. Screen HR, Lee DA, Bader DL, Shelton JC. Development of a technique to determine strains in tendons using the cell nuclei. Biorheology. 2003;40(1-3):361-8.

150. Mirnajafi A, Raymer J, Scott MJ, Sacks MS. The effects of collagen fiber orientation on the flexural properties of pericardial heterograft biomaterials. Biomaterials. 2005;26(7):795-804.

151. Stephens E, Durst C, Swanson J, Grande-Allen K, Ingels N, Miller D. Functional coupling of valvular interstitial cells and collagen via α2β1 integrins in the mitral leaflet Cellular and Molecular Bioengineering. 2010:1-10.

152. Stephens EH, de Jonge N, McNeill MP, Durst CA, Grande-Allen KJ. Age-related changes in material behavior of porcine mitral and aortic valves and correlation to matrix composition. Tissue Engineering Part A. 2010;16(3):867-78.

153. Rabkin E, Aikawa M, Stone JR, Fukumoto Y, Libby P, Schoen FJ. Activated interstitial myofibroblasts express catabolic enzymes and mediate matrix remodeling in myxomatous heart valves. Circulation. 2001;104(21):2525-32.

154. Grande-Allen K, Liao J. The heterogeneous biomechanics and mechanobiology of the mitral valve: Implications for tissue engineering. Current Cardiology Reports. 2011;13(2):113-20.

155. Flanagan TC, Black A, O'Brien M, Smith TJ, Pandit AS. Reference models for mitral valve tissue engineering based on valve cell phenotype and extracellular matrix analysis. Cells Tissues Organs. 2006;183(1):12-23.

156. May-Newman K, Yin FC. Biaxial mechanical behavior of excised porcine mitral valve leaflets. Am J Physiol. 1995;269(4 Pt 2):H1319-27.

157. Grashow JS, Yoganathan AP, Sacks MS. Biaixal stress-stretch behavior of the mitral valve anterior leaflet at physiologic strain rates. Ann Biomed Eng. 2006;34(2):315-25.

158. Sacks MS, Enomoto Y, Graybill JR, Merryman WD, Zeeshan A, Yoganathan AP, et al. In-vivo dynamic deformation of the mitral valve anterior leaflet. Ann Thorac Surg. 2006;82(4):1369-77.

159. Fung YC. What are the residual stresses doing in our blood vessels? Ann Biomed Eng. 1991;19(3):237-49.

160. Stephens EH, Nguyen TC, Itoh A, Ingels NB, Miller DC, Grande-Allen KJ. The effects of mitral regurgitation alone are sufficient for leaflet remodeling. Circulation. 2008;118(14 suppl 1):S243-S9.

161. Stephens EH, Timek TA, Daughters GT, Kuo JJ, Patton AM, Baggett LS, et al. Significant changes in mitral valve leaflet matrix composition and turnover with tachycardia-induced cardiomyopathy. Circulation. 2009;120(11 Suppl):S112-9.

162. Quick DW, Kunzelman KS, Kneebone JM, Cochran RP. Collagen synthesis is upregulated in mitral valves subjected to altered stress. Asaio J. 1997;43(3):181-6.

163. Kunzelman KS, Quick DW, Cochran RP. Altered collagen concentration in mitral valve leaflets: biochemical and finite element analysis. Ann Thorac Surg. 1998;66(6 Suppl):S198-205.

164. Xing Y, Warnock JN, He Z, Hilbert SL, Yoganathan AP. Cyclic pressure affects the biological properties of porcine aortic valve leaflets in a magnitude and frequency dependent manner. Ann Biomed Eng. 2004;32(11):1461-70.

165. Filip DA, Radu A, Simionescu M. Interstitial cells of the heart valves possess characteristics similar to smooth muscle cells. Circ Res. 1986;59(3):310-20.

166. Messier RH, Jr., Bass BL, Aly HM, Jones JL, Domkowski PW, Wallace RB, et al. Dual structural and functional phenotypes of the porcine aortic valve interstitial population: characteristics of the leaflet myofibroblast. Journal of Surgical Research. 1994;57(1):1-21.

167. Mulholland DL, Gotlieb AI. Cell biology of valvular interstitial cells. Canadian Journal of Cardiology. 1996;12(3):231-6.

168. Stephens EH, Durst CA, West JL, Grande-Allen KJ. Mitral valvular interstitial cell responses to substrate stiffness depend on age and anatomic region. Acta Biomaterialia. 2011;7(1):75-82.

169. Sacks MS, He Z, Baijens L, Wanant S, Shah P, Sugimoto H, et al. Surface strains in the anterior leaflet of the functioning mitral valve. Annals of Biomedical Engineering. 2002;30(10):1281-90.

170. Schenke-Layland K. Non-invasive multiphoton imaging of extracellular matrix structures. J Biophotonics. 2008;1(6):451-62.

171. Lilledahl M, Pierce D, Ricken T, Holzapfel G, Davies C. Structural analysis of articular cartilage using multiphoton microscopy: Input for biomechanical modeling. IEEE Trans Med Imaging. 2011;30(9):1635-48.

172. Cao L, Guilak F, Setton L. Pericellular matrix mechanics in the anulus fibrosus predicted by a three-dimensional finite element model and in situ morphology. Cellular and Molecular Bioengineering. 2009;2(3):306-19.

173. Courtney T, Sacks MS, Stankus J, Guan J, Wagner WR. Design and analysis of tissue engineering scaffolds that mimic soft tissue mechanical anisotropy. Biomaterials. 2006;27(19):3631-8.

174. Chaudhuri BB, Kundu P, Sarkar N. Detection and gradation of oriented texture. Pattern Recogn Lett. 1993;14(2):147-53.

175. Karlon WJ, Covell JW, McCulloch AD, Hunter JJ, Omens JH. Automated measurement of myofiber disarray in transgenic mice with ventricular expression of ras. Anat Rec. 1998;252(4):612-25.

176. Agoram B, Barocas VH. Coupled macroscopic and microscopic scale modeling of fibrillar tissues and tissue equivalents. J Biomech Eng. 2001;123(4):362-9.

177. Sacks MS, Chuong CJ. Characterization of Collagen Fiber Architecture in the Canine Central Tendon. Journal of Biomechanical Engineering. 1992;114:183-90.

178. Sacks MS, Smith DB, Hiester ED. A small angle light scattering device for planar connective tissue microstructural analysis. Ann Biomed Eng. 1997;25(4):678-89.

179. Scott M, Vesely I. Aortic valve cusp microstructure: The role of elastin. Annals of Thoracic Surgery. 1995;60:S391-S4.

180. Vesely I. The role of elastin in aortic valve mechanics. Journal of Biomechanics. 1998;31(2):115-23.

181. Butcher JT, Nerem RM. Valvular endothelial cells and the mechanoregulation of valvular pathology. Philos Trans R Soc Lond B Biol Sci. 2007;362(1484):1445-57.

182. Butcher JT, Nerem RM. Valvular endothelial cells regulate the phenotype of interstitial cells in co-culture: effects of steady shear stress. Tissue Eng. 2006;12(4):905-15.

183. Carruthers CA, Alfieri CM, Joyce EM, Watkins SC, Yutzey KE, Sacks MS. Gene expression and collagen fiber micromechanical interactions of the semilunar heart valve interstitial cell. Cell Mol Bioeng. 2012;5(3):254-65.

184. Gilbert TW, Freund JM, Badylak SF. Quantification of DNA in biologic scaffold materials. Journal of Surgical Research. 2009;152(1):135-9.

185. Valentin JE, Stewart-Akers AM, Gilbert TW, Badylak SF. Macrophage participation in the degradation and remodeling of extracellular matrix scaffolds. Tissue Eng Part A. 2009;15(7):1687-94.

186. Freytes DO, Stoner RM, Badylak SF. Uniaxial and biaxial properties of terminally sterilized porcine urinary bladder matrix scaffolds. J Biomed Mater Res B Appl Biomater. 2008;84(2):408-14.

187. Hudson TW, Liu SY, Schmidt CE. Engineering an improved acellular nerve graft via optimized chemical processing. Tissue Eng. 2004;10(9-10):1346-58.

188. Courtman DW, Pereira CA, Kashef V, McComb D, Lee JM, Wilson GJ. Development of a pericardial acellular matrix biomaterial: biochemical and mechanical effects of cell extraction. J Biomed Mater Res. 1994;28(6):655-66.

189. Kasimir MT, Rieder E, Seebacher G, Silberhumer G, Wolner E, Weigel G, et al. Comparison of different decellularization procedures of porcine heart valves. Int J Artif Organs. 2003;26(5):421-7.

190. Remlinger NT, Wearden PD, Gilbert TW. Procedure for decellularization of porcine heart by retrograde coronary perfusion. J Vis Exp. 2012;6(70):50059.

191. Ott HC, Matthiesen TS, Goh SK, Black LD, Kren SM, Netoff TI, et al. Perfusion-decellularized matrix: using nature's platform to engineer a bioartificial heart. Nat Med. 2008;14(2):213-21.

192. Ross EA, Williams MJ, Hamazaki T, Terada N, Clapp WL, Adin C, et al. Embryonic stem cells proliferate and differentiate when seeded into kidney scaffolds. J Am Soc Nephrol. 2009;20(11):2338-47.

193. Yoeruek E, Bayyoud T, Maurus C, Hofmann J, Spitzer MS, Bartz-Schmidt KU, et al. Decellularization of porcine corneas and repopulation with human corneal cells for tissue-engineered xenografts. Acta Ophthalmol. 2012;90(2):1755-3768.

194. Brown BN, Barnes CA, Kasick RT, Michel R, Gilbert TW, Beer-Stolz D, et al. Surface characterization of extracellular matrix scaffolds. Biomaterials. 2010;31(3):428-37.

195. Wu TC, Wan YJ, Chung AE, Damjanov I. Immunohistochemical localization of entactin and laminin in mouse embryos and fetuses. Dev Biol. 1983;100(2):496-505.

196. Parekh A, Mantle B, Banks J, Swarts JD, Badylak SF, Dohar JE, et al. Repair of the tympanic membrane with urinary bladder matrix. Laryngoscope. 2009;119(6):1206-13.

197. Lecheminant J, Field C. Porcine urinary bladder matrix: a retrospective study and establishment of protocol. J Wound Care. 2012;21(10):476-82.

198. Zhang L, Zhang F, Weng Z, Brown BN, Yan H, Ma X, et al. Effect of an Inductive Hydrogel composed of Urinary Bladder Matrix upon Functional Recovery Following Traumatic Brain Injury. Tissue Eng Part A. 2013;19(17-18):1909-18.

199. Liu L, Deng L, Wang Y, Ge L, Chen Y, Liang Z. Porcine urinary bladder matrix-polypropylene mesh: a novel scaffold material reduces immunorejection in rat pelvic surgery. Int Urogynecol J. 2012;23(9):1271-8.

200. Brown B, Lindberg K, Reing J, Stolz DB, Badylak SF. The basement membrane component of biologic scaffolds derived from extracellular matrix. Tissue Eng. 2006;12(3):519-26.

201. Nieponice A, Gilbert TW, Badylak SF. Reinforcement of esophageal anastomoses with an extracellular matrix scaffold in a canine model. Ann Thorac Surg. 2006;82(6):2050-8.

202. Eberli D, Susaeta R, Yoo JJ, Atala A. Tunica repair with acellular bladder matrix maintains corporal tissue function. Int J Impot Res. 2007;19(6):602-9.

203. Kelly DJ, Rosen AB, Schuldt AJ, Kochupura PV, Doronin SV, Potapova IA, et al. Increased myocyte content and mechanical function within a tissue-engineered myocardial patch following implantation. Tissue Eng Part A. 2009;15(8):2189-201.

204. Rosario DJ, Reilly GC, Ali Salah E, Glover M, Bullock AJ, Macneil S. Decellularization and sterilization of porcine urinary bladder matrix for tissue engineering in the lower urinary tract. Regen Med. 2008;3(2):145-56.

205. Shah U, Bien H, Entcheva E. Microtopographical effects of natural scaffolding on cardiomyocyte function and arrhythmogenesis. Acta Biomater. 2010;6(8):3029-34.

206. Eweida A, Saad M, Gabr E, Marei M, Khalil MR. Cultured keratinocytes on urinary bladder matrix scaffolds increase angiogenesis and help in rapid healing of wounds. Adv Skin Wound Care. 2011;24(6):268-73.

207. D'Amore A, Stella JA, Wagner WR, Sacks MS. Characterization of the complete fiber network topology of planar fibrous tissues and scaffolds. Biomaterials. 2010;31(20):5345-54.

208. Theodossiou TA, Thrasivoulou C, Ekwobi C, Becker DL. Second harmonic generation confocal microscopy of collagen type I from rat tendon cryosections. Biophys J. 2006;91(12):4665-77.

209. Crapo PM, Gilbert TW, Badylak SF. An overview of tissue and whole organ decellularization processes. Biomaterials. 2011;32(12):3233-43.

210. Wolf MT, Daly KA, Brennan-Pierce EP, Johnson SA, Carruthers CA, D'Amore A, et al. A hydrogel derived from decellularized dermal extracellular matrix. Biomaterials. 2012;33(29):7028-38.

211. Carlson TR, Hu H, Braren R, Kim YH, Wang RA. Cell-autonomous requirement for beta1 integrin in endothelial cell adhesion, migration and survival during angiogenesis in mice. Development. 2008;135(12):2193-202.

212. Barczyk M, Carracedo S, Gullberg D. Integrins. Cell Tissue Res. 2010;339(1):269-80.

213. Petit V, Thiery JP. Focal adhesions: structure and dynamics. Biol Cell. 2000;92(7):477-94.

214. Wang JH, Thampatty BP. An introductory review of cell mechanobiology. Biomech Model Mechanobiol. 2006;5(1):1-16.

215. Eyckmans J, Boudou T, Yu X, Chen CS. A hitchhiker's guide to mechanobiology. Dev Cell. 2011;21(1):35-47.

216. Simpson DG, Terracio L, Terracio M, Price RL, Turner DC, Borg TK. Modulation of cardiac myocyte phenotype in vitro by the composition and orientation of the extracellular matrix. J Cell Physiol. 1994;161(1):89-105.